Study of electron transport in semiconductor nanodevices by Scanning Gate Microscopy

Peng Liu

UNIVERSITÉ DE GRENOBLE

THÈSE

Pour obtenir le grade de

DOCTEUR DE L'UNIVERSITÉ DE GRENOBLE

Spécialité : **Nanophysique**

Arrêté ministériel :

Présentée par

Peng LIU

Thèse dirigée par **Vincent BAYOT** et
codirigée par **Hermann SELLIER**

préparée au sein du **Institut Néel, CNRS**
dans **l'École Doctorale de Physique**

Etude du transport électronique dans les nanodispositifs semiconducteurs par microscopie à grille locale

Thèse soutenue publiquement le **30 septembre 2011**,
devant le jury composé de :

M. Christophe CHAUBET		
Professeur d'Université	Montpellier	Rapporteur
M. Zhao-Zhong WANG		
Directeur de Recherche	Paris	Rapporteur
M. Hervé COURTOIS		
Professeur d'Université	Grenoble	Président
M. Xavier WALLART		
Directeur de Recherche	Lille	Examinateur
M. Vincent BAYOT		
Professeur d'Université	Grenoble	Examinateur
M. Hermann SELLIER		
Maître de Conférence	Grenoble	Examinateur

Acknowledgements

I must acknowledge first, my advisors Vincent Bayot and Hermann Sellier, without whom, this thesis would never have been possible. I have learnt a lot about the methodology of research from them.

I am indebted to Ludovic Desplanque and Xavier Wallart, who supplies us a lot of state-of-the-art high mobility 2 dimensional electron gas samples. I cannot thank Benoit Hackens and Frederico Martins enough who spent countless hours in cleanroom to fabricate numerous devices for me. Most of the research work would not have been possible without their experience and patience.

I want to express my gratitude to Serge Huant for his fruitful discussion of our results and kind help in preparing my thesis defense presentation.

I thank Marco Pala for his theoretical work, which helps to design the device structure and to interpret the experimental results. I thank Benjamin Sacépé for his suggestions in the experiments and data analysis. I thank Jean-François Motte for his ever present enthusiasm, dedicated maintenance of the instruments inside the lab as well as his help with the manipulation of cryogenic facilities.

Many thanks are due to Alexis Mosset and Justine Laurent. We work in the same laboratory together for a quite long period. They helped me a lot in my first days after arriving in Grenoble to get used to the life here. I also thank the other members in the Champ Proche group in Néel institute. They helped a lot in various aspects in the three years.

I acknowledge the financial support from Nanosciences Foundation during my thesis.

I appreciate the kind understanding from my parents and wife. Without their help, I would have never completed this thesis.

Résumé

La microscopie de grille à balayage (SGM pour Scanning Gate Microscopy), développée à la fin des années 1990, est devenue un outil puissant pour étudier les propriétés électroniques locales dans les nano-dispositifs semi-conducteurs. La SGM est basée sur la technique AFM, mais la pointe métallique est utilisée comme une grille mobile couplée capacitivement au dispositif, et les propriétés de transport électronique sont étudiées sous l'influence de cette grille, fournissant des informations spatiales à haute résolution. Cette thèse décrit d'abord le remplacement de la détection optique de notre système AFM par une détection piézo-électrique utilisant un diapason à quartz, puis les résultats de mesures SGM sur divers nano-dispositifs, qui sont tous fabriqués à partir d'hétérostructures InGaAs / InAlAs contenant un gaz d'électrons bi-dimensionnel (2DEG) de grande mobilité situé à quelques dizaines de nanomètres sous la surface. Sur une simple constriction, nous étudions l'interaction pointe-échantillon avec deux approches: la force électrostatique et l'effet capacitif. Sur une boite quantique, nous étudions les phénomènes de blocage de Coulomb lorsque la pointe est utilisée comme une grille pour moduler la charge à l'intérieur de la boite. Dans un travail sur le paradoxe de Braess, avec l'aide de simulations numériques, nous découvrons un effet paradoxal en modulant la largeur du canal central dans un dispositif mésoscopique en forme de double anneau, en analogie avec le paradoxe qui se produit dans un réseau classique. Par une étude détaillée de l'évolution de la conductance, nous découvrons enfin plusieurs pièges de charge dans les images SGM, et proposons un modèle pour interpréter le changement de conductance en présence de pièges de charge. Nous développons alors une méthode pour imager directement les pièges de charge par des mesures de transconductance avec une modulation de la tension sur la pointe.

Mots-clés:

microscopie à force atomique, cryogénie, microscopie à balayage de grille, système d'électrons bi-dimensionnel, transport électronique, diapason à quartz, force capacitive, boite quantique, blocage de Coulomb, paradoxe de Braess, pièges de charge

Abstract

Scanning gate microscopy (SGM), developed in the late 1990's, has become a powerful tool to investigate the local electronic properties in semiconductor nano devices. SGM is based on the AFM technique but the metallic tip is used as a movable gate capacitively coupled to the device, and the electron transport property is studied on influence of this gate, providing spatial information with high resolution. This thesis presents the update of the force detection mode of our AFM system from optical method to force sensing by a quartz tuning fork, and the SGM measurement results on various nano devices, all of which are fabricated from InGaAs/InAlAs heterostructures containing a high mobility 2DEG located a few tens of nanometers below the surface. On a 2DEG constriction, we investigate the tip-sample interaction with two approaches: the capacitive force and the gate effect. On a quantum dot, we study the Coulomb blockade phenomena where the tip is used as a gate to modulate the charging/discharging inside the dot. In a work on Braess paradox, with the help of numerical simulations, we discover a Braess paradox effect by modulating a channel width in a 'double-ring' shaped mesoscopic device in analogy with the one that occurs in a classical network. By a detailed study of the conductance changes, we discover several charge traps from the SGM map, and propose a model to interpret the conductance change with the presence of charge traps. We develop a method to directly image the charge traps by transconductance measurements with a voltage modulation on the tip.

Keywords:

Atomic force microscopy, cryogenics, scanning gate microscopy, two-dimensional electron system, electron transport, quartz tuning fork resonator, capacitive force, quantum dot, Coulomb blockade, Braess paradox, charge traps

Contents

Chapter 1

Introduction

1.1 Electronic devices

In 1947, John Bardeen, Walter Brattain and William Shockley from Bell Labs developed the first transistor on the basis of germanium. After the first silicon transistor produced by Texas Instruments in 1954, the silicon technologies started. In parallel to the technological progresses, the fundamental research on semiconductor also developed rapidly. From then on, science and technologies benefitted from each other. Thanks to the invention of the field effect transistor, fundamental research on two dimensional electron systems (2DES) became available from the 1960s, initially based on elemental semiconductor silicon [1], later on III-V compound semiconductor like gallium arsenide (GaAs) [2], and II-VI compound semiconductor like cadmium telluride (CdTe) [3], graphene [4] and oxide materials [5]. Besides the boost to the microelectronic industry, two-dimensional systems opened a new research area, where integral and fractional quantum Hall effects were observed and led to two Nobel prizes in 1985 [6]and 1998 [7].

Nowadays, the electronic properties of 2DES are still an important field of fundamental research, in which much of the work is based on the measurements of electron transport using macroscopic leads. Transport measurements is a powerful tool that have provided deep insights into the electronics properties of 2DES. However, they are not suitable for studying the local properties of these systems, because they do not provide spatial information. In order to study the local electronic properties of 2DES in more details, people introduced specific scanning probe techniques.

1.2 Scanning probe techniques

Since the invention of scanning tunneling microscopy (STM) in 1981 [8, 9], the family of scanning probe microscopy has included atomic force microscopy (AFM) [10] (contact, no-contact, tapping modes), electrostatic force microscopy (EFM), magnetic force microscopy (MFM), scanning near-field optical microscopy (SNOM) [11], scanning capacitance microscopy (SCM) [12], etc.

Different from traditional optical microscopy, scanning probe microscopy (SPM) techniques use a physical probe to study the probe-sample interaction and obtain a spatial map of the sample properties. So, the spatial resolution is not limited by the diffraction of light, and can reach sub-Å resolution.

Shortly after the invention of SPM, people realized that, with such powerful tools, not only the specimens' properties could be obtained from the measurements, e.g., extracting electron density of states from tunneling current in STM, magnetization from MFM, but also the modification of specimens became available, e.g., moving atoms by STM [13], nano-lithography by AFM [14], etc.

1.3 Scanning Gate Microscopy (SGM)

Scanning gate microscopy (SGM) was developed in the late 1990's to overcome the limitation of STM that does not work on semiconductor devices based on 2DES buried in heterostructures [15]. SGM is based on the AFM technique but the metallic tip is used as a movable gate capacitively coupled to the device, and the electron transport property is studied on influence of this gate at the nanometer scale.

In SGM, the in-plane electrical conductance of the device is measured simultaneously as scanning the tip above the device. The tip acts therefore as an element which controls the behavior of the device. On this point of view, SGM is different from most types of SPMs where the tip solely plays the role of a sensor, e.g., in STM, EFM, SCM, etc. In general, SGM is a combination of a nano-device exhibiting gate effect under certain circumstance and a scanning probe microscope where the tip is used as a flying nano-gate.

The devices that have been studied by SGM can be made of semiconductor 2D electron system [16, 17], nanowires [18], nanotubes [19], graphene [20, 21, 22], superconductors [23]. The 2DES devices can be patterned into quantum dot

(QD) [18, 19], quantum point contact (QPC) [16, 24], quantum rings [25, 26], mesoscopic Hall bars [27, 28], etc.

The SPMs used in SGM studies are essentially AFMs with conductive tips while the force sensors have been varied. Quite important, the microscope should be adapted to low-temperature (below 4.2 K) because quantum phenomena are the principle motivations of these studies and to magnetic field environment if magneto-related effects are to be explored, e.g., Aharonov-Bohm effect [25], quantum Hall effect [27, 28], superconducting transition [23] and magnetic focusing phenomena [24].

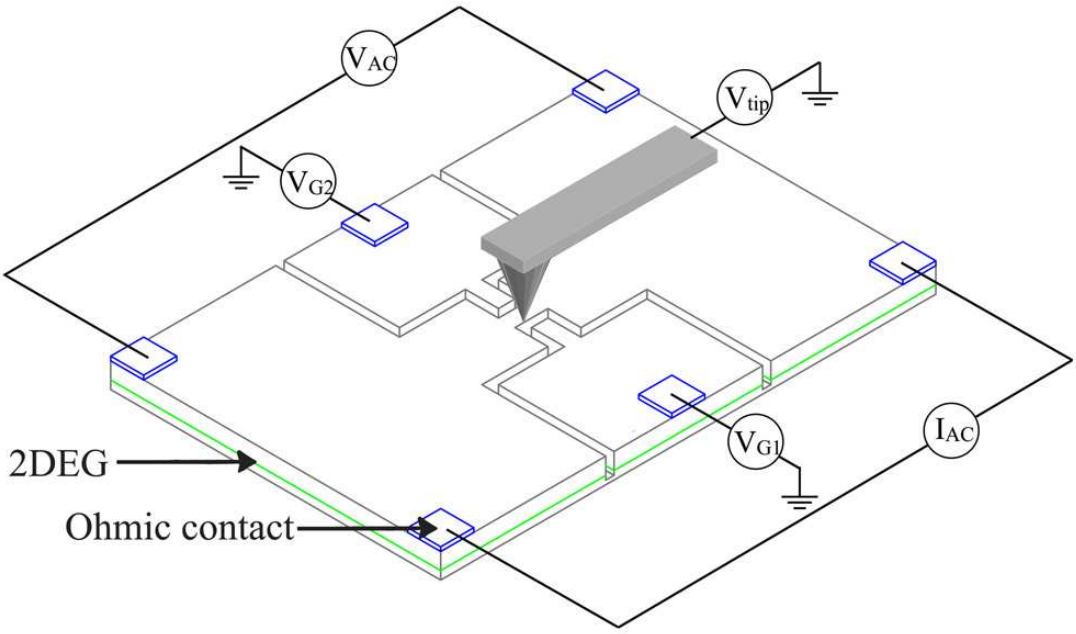

Figure 1.1: Schematic of the working principle of scanning gate microscopy. In a standard 4-probe conductance measurement configuration, the device is biased with an AC current I_{AC}, and the voltage difference across the device V_{AC} is detected by lock-in method. The conductance of the device can be modulated by changing the lateral gate voltages V_{G1} and V_{G2}, or the tip gate voltage V_{tip}. When the biased tip is scanned in a plane above the device, a map of conductance change is built as a function of the tip position.

The working principle of SGM is schematically depicted in Figure A.1. The biased tip at voltage V_{tip} is scanned in the plane with a fixed distance from the device surface, and the conductance G of the device is recorded simultaneously

to build a map of conductance change (or local gate effect) as a function of the tip position (i.e. a SGM image). This map can be recorded for different tip voltages, or alternatively conductance change spectroscopies versus tip voltage can be recorded for specific tip positions.

1.4 Description of the content

In this thesis, I discuss the building blocks of SGM, including devices, instrumentations, experimental operations, several problems encountered, solutions, and some results obtained on different devices.

In Chapter 2, I describe the physical properties of two-dimensional electron gas (2DEG) formed at the hetero-interface of III-V semiconductors, and focus on a few mesoscopic electron transport phenomena (conductance quantization in QPC, Coulomb blockade in QD, and Aharonov-Bohm effect) and on their previous investigations by SGM experiments.

In Chapter 3, I discuss the microscope used in this work, including a detailed description of the quartz tuning fork (TF) sensor (mechanical and electrical models, preparation of TF sensor with AFM tip, force detection with TF), a presentation of the microscope assembly, the microscope control system (software) and the operation in AFM mode for topography at room-temperature and low-temperature.

In Chapter 4, I discuss the sample preparations (in both cleanrooms of Louvain-la-Neuve and Grenoble), the electron transport measurement system, the operation of the microscope in SGM mode, a simple SGM experiment on a constriction to illustrate the capacitive coupling between tip and device and extract the tip induced potential experienced by the electrons, and finally a tentative SGM experiment on a mesoscopic elliptic cavity.

In Chapter 5, I present the results of three representative SGM experiments performed in my PhD period: (i) Coulomb blockade on a quantum dot controlled by lateral gates; (ii) Braess paradox phenomena in a double ring nanostructure and (iii) imaging of single charge traps coupled to the 2DEG of III-V semiconductor heterostructure.

In Chapter 6, I make conclusions and perspectives to continue and extend this work in the future.

Chapter 2

Background

Contents

2.1 Properties of the two dimensional electron gas

The 2DEG is a very interesting system to study quantum phenomena at low temperature. In this work, we studied several materials, all based on 2DEGs.

2.1.1 The InGaAs/InAlAs heterostructures

The InGaAs/InAlAs lattice matched to InP system is of great interest for both electronic and optical devices. The properties of small effective mass, high mobility, large conduction band discontinuity (0.5 eV), high Γ-L separation (0.55 eV) [29] offers the potential for the application in high-speed electronic devices. On the SGM point of view, the shorter lateral depletion length (10∼30 nm) is another advantage over AlGaAs/GaAs system (∼100 nm) [30].

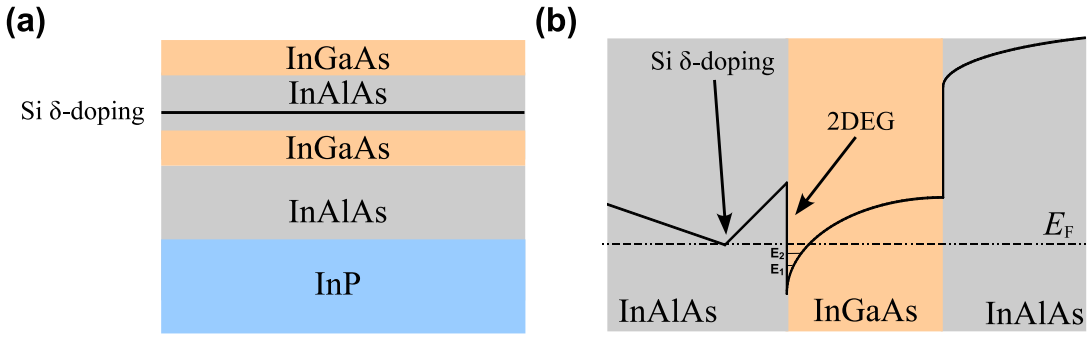

Figure 2.1: Formation of 2DEG on InGaAs/InAlAs interface. (a) Epitaxial layers sequence of InGaAs/InAlAs structures on InP substrate. (b) Conduction band diagram of InGaAs/InAlAs heterostructures. The 2DEG forms at the interface of the two different materials.

Figure 2.1 shows an example of InGaAs/InAlAs heterostructure used in our experiments as described in Chapter 4 and 5.

In absence of dopant, the heterostructure presents a series of conduction band offsets at each interface, and the smaller gap of InGaAs lies fully inside the band gap of InAlAs. In presence of a plane of Si dopants in top InAlAs layer, the bands of the different materials are shifted in order to align their Fermi level, the band right at the InGaAs/InAlAs interface starts to bend (Figure 2.1 right). The bending produces a quantum well (called channel) that confines in the lateral

direction the electrons transferred from the dopants. The confinement leads to discrete subbands, which can be occupied by charge carriers, if the Fermi level lies above the energy level of these subbands. When electrons start to fill these bands, they form a 2DEG.

Since the electrons are provided by a nearby donor layer of silicon atoms (called δ-doped layer), the electron density in the 2DEG is strongly dependent on the distance and doping density of this layer. The position of the δ-doping is often above the 2DEG itself to avoid disturbance during the molecular beam epitaxy (MBE) growth of the channel. The separation of the donor layer from the 2DEG (by the so-called spacer layer) enables the electrons to move with a minimum of scattering inside the 2DEG.

2.1.2 Subbands in the quantum well

Consider the 2DEG depicted in Figure 2.1. The electrons are free to move in the x-y plane, but confined in z-growth direction by some potential U_z. The electron wavefunctions in this structure (no external fields) can be written in the form:

$$\Psi_{\mathbf{r}} = \phi_j(z) \exp\{ik_x x\} \exp\{ik_y y\} \tag{2.1}$$

with the dispersion relation:

$$E = E_c + \epsilon_j + \frac{\hbar^2}{2m^*}(k_x^2 + k_y^2) \tag{2.2}$$

where E_c is the conduction band edge. The index j numbers the different subbands, each having a different wavefunction ϕ_z in the z-direction and a cut-off energy ϵ_j. Usually at low temperature with low carrier densities, only the lowest subband (j=1) is occupied.

2.1.3 Hall and Shubnikov-de Haas Effects

2.1.3.1 Hall Effect

Electron transport in two-dimensional electron gases is routinely characterized and described in terms of the Drude-Boltzmann theory [31]. In magneto-transport experiments, a current I is applied on the 2DEG, which is patterned as a Hall-bar structure, and next, the longitude and transverse voltages, respectively $\mathrm{U_L}$ and $\mathrm{U_H}$ are measured, as shown in Figure 2.2.

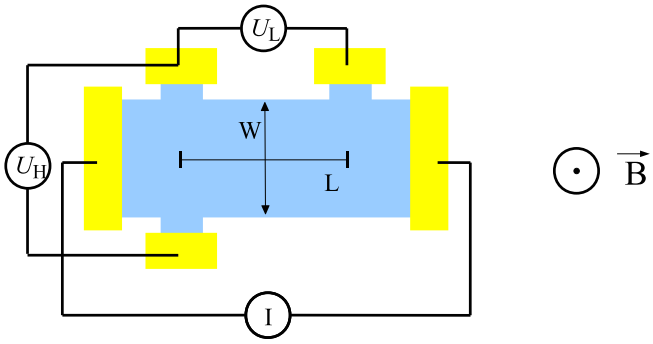

Figure 2.2: Schematic of magneto-resistance measurement. The magnetic field direction is perpendicular to the paper plane. Blue: 2DEG, Yellow: metal contacts.

Considering the Hall-bar width W, and the separation of longitudinal voltage probes L, the components of the two-dimensional resistivity tensor

$$\varrho = \begin{pmatrix} \varrho_{xx} & \varrho_{xy} \\ -\varrho_{xy} & \varrho_{yy} \end{pmatrix} \tag{2.3}$$

can be expressed as

$$\varrho_{xx} = \frac{W}{L}\frac{U_L}{I} = R_\square \text{ and } \varrho_{xy} = \frac{U_H}{I} \tag{2.4}$$

where $R_\square = \varrho_{xx}$ is the square resistance

The electron density (Hall density) n_H can then be determined from the low magnetic field Hall resistivity, which is linear versus magnetic field B:

$$n_H = \frac{B}{e\varrho_{xy}} \tag{2.5}$$

and the Hall mobility $\mu_H = e\tau/m^*$ of the electron with effective mass m^* can then be obtained from

$$\mu_H = \frac{1}{en_H R_\square} \tag{2.6}$$

2.1.3.2 Landau levels and Shubnikov-de Haas oscillations

In quantum mechanics, when a magnetic field is applied perpendicular to the plane of the 2DEG, the cyclotron orbits of electrons are quantized, with the cyclotron frequency of $\omega_c = eB/m^*$. The electron can only occupy orbits with discrete energy levels:

$$E_n = E_c + \epsilon_j + \hbar\omega_c(n + \frac{1}{2}) \tag{2.7}$$

This is called Landau levels (LL) [32], where ϵ_j corresponds to different subband energies due to the confinement in z-direction that is discussed in Section 2.1.2.

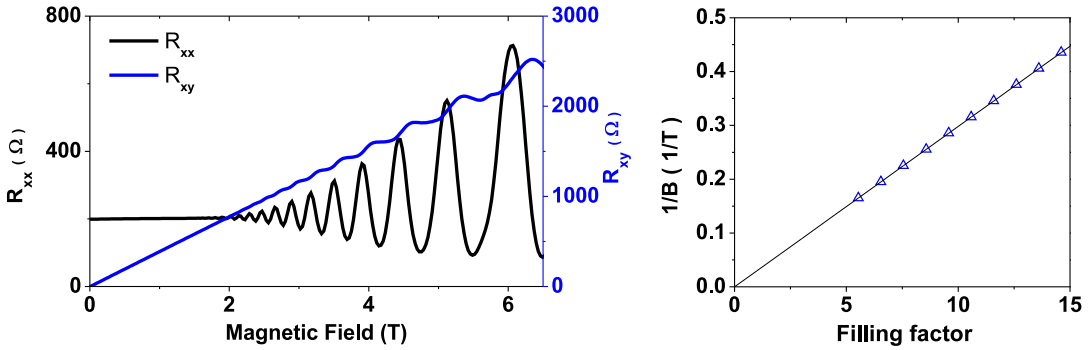

Figure 2.3: Left, Hall effect and Shubnikov-de Haas oscillation. Right, relation between magnetic field and the filling factor. Measurement parameters: temperature 4.2K, current $1\mu A$@17Hz, magnetic field sweeping rate 0.2T/min. Hall bar L/W=4. See Chapter 4.1 for more details.

In a 2D system at zero field, the density of states (DOS) per unit area can be expressed as: $N(E) = m^*/\pi\hbar^2\vartheta(E - E_s)$, where $\vartheta(x)$ is the step function and $E_s = E_c + \epsilon_j$. In magnetic field, $N(E)$ breaks into a sequence of peaks spaced by $\hbar\omega_c$. For each LL, the number of states per unit area $N(E_n) = 2eB/h$. As the magnetic field is increased, (i) the increase of $N(E_n)$ means more electrons can be put in each LL, and (ii) the separation of LL increases. For a fixed Fermi level, the number of filled LL (referred as filling factor ν) decreases. Due to (i) and (ii), as the magnetic field is changed, the position of E_F varies relative to the LL peaks. Each time E_F lies at the center of one LL (respective between two LL), the longitudinal resistance reaches a maximum (respective minimum). This phenomena is the origin of Shubnikov-de Haas oscillation [31]. The electron density n_s is related to the magnetic field values of two successive peaks (ν half-integer) via:

$$\frac{n_s}{2eB_1/h} - \frac{n_s}{2eB_2/h} = 1 \;\Rightarrow\; n_s = \frac{2e}{h}\frac{1}{\Delta(1/B)} \tag{2.8}$$

if the spin-degenerate Landau levels are assumed.

To anticipate complications in sample used in Section 5.2, it has to be noted, that the electron density deduced from the SdH data can be smaller than that deduced from the low field Hall data. This is because the Hall voltage gives the total electron density including other electron layers in parallel to the 2DEG.

However, these parallel conduction paths are most of time associated with low mobilities, and do not contribute to SdH effect.

For 2DEG made of III-V materials, typical values for electron densities range from 10^{11} cm^{-2} to 10^{12} cm^{-2}, and mobilities are typically between 10^4 cm^2/Vs and 10^7 cm^2/Vs [33] at liquid helium temperature.

2.1.4 Characteristic energy, time and length

At thermal equilibrium at temperature T, the occupied states at energy E are described with the Fermi distribution function:

$$f_0(E) = \frac{1}{1 + \exp^{(E-E_F)/k_B T}} \tag{2.9}$$

where E_F is the Fermi energy. To relate the electron density n_s to the Fermi energy, we make use of the relation

$$n_s = \int N_s(E) f_0(E) dE \tag{2.10}$$

where $N_s \equiv m^*/\pi\hbar^2$ is the 2D density of states per unit area per unit energy[1]. In the degenerate limit at low T, we obtain

$$n_s = N_s \times (E_F - E_s) \tag{2.11}$$

At low temperature, the conductance is determined entirely by the electrons with energy close to the Fermi energy. The wave vector of such electrons is referred as the Fermi wave vector (k_F):

$$E_F - E_s = \frac{\hbar^2 k_F^2}{2m^*} \Rightarrow \hbar k_F = \sqrt{2m^*(E_F - E_s)} \tag{2.12}$$

Using Equation 2.11 we can express the Fermi wave vector in terms of the electron density:

$$k_F = \sqrt{2\pi n_s} \tag{2.13}$$

The corresponding Fermi velocity and wavelength are:

$$v_F = \hbar k_F / m^* \tag{2.14}$$

$$\lambda_F = 2\pi/k_F = \sqrt{2\pi/n_s} \tag{2.15}$$

[1]The effective mass of electrons in $In_xGa_{1-x}As$ can be calculated by [34]: $m^* = 0.079 - 0.038x$.

The elastic mean free path, l_e is the typical distance that an electron travels before the initial direction of its momentum is changed, which is often related to diffusion on static scatters, that conserves energy. Combining information about the electron density and mobility, l_e can be determined from:

$$l_e = \upsilon_{\mathrm{F}} \tau_m \tag{2.16}$$

where $\tau_m = \mu_{\mathrm{H}} m^*/e$ is the momentum relaxation time. And the diffusion constant is given by

$$D = \frac{1}{2} \upsilon_{\mathrm{F}}^2 \tau_m = \frac{1}{2} \upsilon_{\mathrm{F}} l_e \tag{2.17}$$

The phase-relaxation length l_ϕ is the average distance that an electron travels before it experiences inelastic scattering which destroys its initial coherent state. In the case of high-mobility 2DEG, phase relaxation often occurs on a timescale τ_ϕ which is of the same order or shorter than the momentum relaxation time τ_m. Then $l_\phi = \upsilon_{\mathrm{F}} \tau_\phi$ holds with the Fermi velocity υ_{F}. In low mobility materials, τ_m can be considerably shorter than τ_ϕ, and diffusive motion may occur over a phase-coherent region; then $l_\phi^2 = D\tau_\phi$.

2.2 Mesoscopic electron transport in 2DEG nano structures

In general, structures in which the phase relaxation length l_ϕ is comparable to the characteristic system size L but much larger than the Fermi wavelength λ_{F} are called mesoscopic systems. Depending on the relation between the elastic mean free path of electrons l_e and the system size L, the system is called ballistic ($l_e \gg L$) or diffusive ($l_e \ll L$) systems. Below, I discuss three representative phenomena of electron transport in mesoscopic systems: (i) conductance quantization, (ii) Coulomb blockade and (iii) Aharonov-Bohm effect, and present the SGM studies on these effects reported in the literature.

2.2.1 Conductance quantization in Quantum Point Contacts

In 2DEGs formed in semiconductor heterostructures, the Fermi wavelength λ_{F} is in the order of tens of nanometers. This makes it possible to study a constriction with an opening whose size is comparable with λ_{F} and smaller than the elastic

mean free path. Such type of constriction is referred as quantum point contact (QPC).

In 1988, Delft-Philips [35] and Cambridge [36] groups independently discovered that the conductance across a QPC is quantized. They controlled the width W of the QPC by applying negative voltages on split-gates. With the increase of gate voltages, the conductance does not increase continuously, but with steps of height $2e^2/h \approx 77.48\mu S = (12.9k\Omega)^{-1}$. An example of this effect is shown in Figure 2.4.

2.2.1.1 The origin of conductance quantization

An elementary explanation of the quantization compares the constriction as a quasi 1D electron wave guide, through which a small integer number $\mathrm{N} \approx 2\mathrm{W}/\lambda_\mathrm{F}$ of transverse modes can propagate at the Fermi level. The wide regions connecting the constriction on both sides are reservoirs of electrons in local equilibrium. A voltage difference V between the reservoirs induces a current I through the constriction, equally distributed among the N modes. This equipartition rule is not immediately obvious, because electrons at the Fermi level in each mode have different group velocities $\upsilon_\mathrm{n} = \mathrm{d}\omega/\mathrm{dk} = \frac{1}{\hbar} \cdot \mathrm{dE}/\mathrm{dk}$, where k is the longitudinal wave vector. However, the difference in group velocity is compensated by the difference in 1D density of states $\rho_\mathrm{n} = \mathrm{g(k)dk/dE} = \frac{1}{2\pi} \cdot \mathrm{dk/dE}$. As a result, each mode carries the same current $\mathrm{I_n} = \rho_\mathrm{n}(\mathrm{eV})\mathrm{e}\upsilon_\mathrm{n} = \mathrm{Ve}^2\rho_\mathrm{n}\upsilon_\mathrm{n} = \mathrm{Ve}^2/\mathrm{h}$. Summing over all modes in the waveguide, one obtains the conductance $\mathrm{G} = \mathrm{I/V} = \mathrm{Ne}^2/\mathrm{h}$. The experimental step size is twice e^2/h because spin-up and spin-down modes are degenerate at zero magnetic field.

The quantized conductance of a point contact provides firm experimental support for the Landauer formula,

$$G = \frac{2e^2}{h} \sum_n t_n \tag{2.18}$$

where t_n (between 0 and 1) are transmission coefficients for the conductance of a disordered mesoscopic region connected to two electron reservoirs. For an 'ideal' 1D conductor, the N first coefficients are equal to 1 and all others are equal to 0. Deviations from exact quantization in a realistic geometry originates from the series resistance from the wide regions, whose magnitude can not be determined precisely, or from excess resistance due to backscattering at the entrance and exit of the constriction, due to the abrupt widening of the geometry. This can be

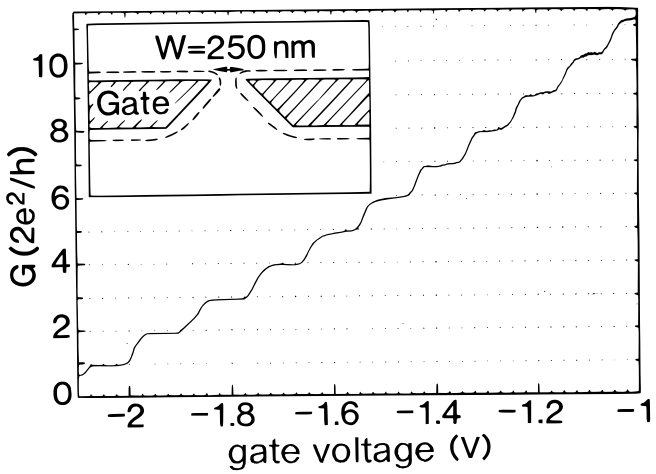

Figure 2.4: Conductance quantization QPC conductance as a function of gate voltage, measured at 600 mK, demonstrating the conductance quantization in units of $2e^2/h$. The data are obtained from the two-terminal resistance after subtraction of a background resistance. Inset: schematic of a QPC. Taken from ref [35]

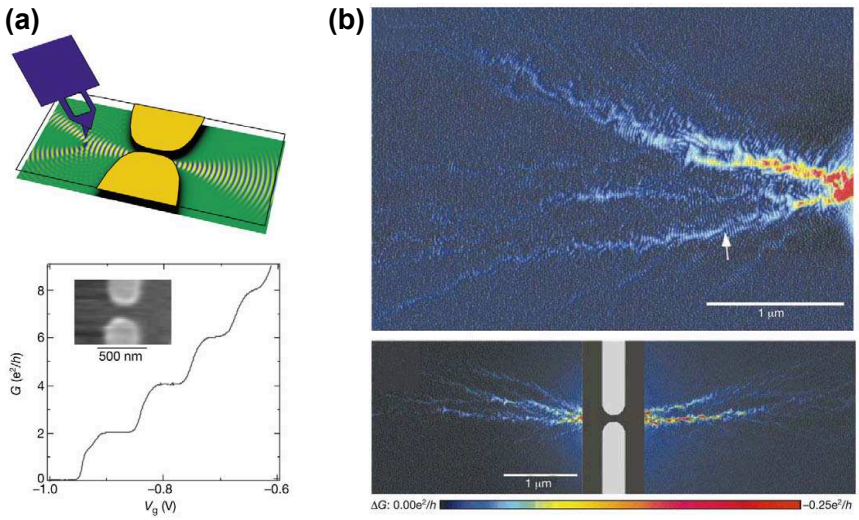

Figure 2.5: (a) Top, schematic of the SGM experimental setup; and bottom, the QPC conductance as a function of the surface gate voltages. Inset: topography image of the QPC. (b) Top, Electron flow from one side of the QPC; and bottom, electron flow from both sides of the QPC. These two images were obtained from two different QPCs, while both of the two were biased on the $G_0 = 2e^2/h$ conductance step. Taken from [16]

contrasted with the quantization of the Hall resistance in strong magnetic fields, where an accuracy better than 1 part in 10^7 is obtained routinely [37].

2.2.1.2 SGM experiments on conductance quantization

In reference [16], the authors reported the observation of electron flow emitted by a QPC, which was made on the 2DEG sample of AlGaAs/GaAs heterostructure by placing two metal gates on the surface. They scanned a charged tip above the nearby regions of the QPC on both two sides. The capacitive coupling between the tip and 2DEG reduced the carriers density of the 2DEG plane in a small spot directly beneath the tip, creating a depletion region that backscatters the electron waves. When the tip was over areas of high electron flow, the conductance through the QPC decreased; when the tip was over areas of relatively low electron flow, the conductance through the QPC was unmodified. They changed the voltage applied on the surface gates to tune the QPC conductance on the first, second and third quantum conductance plateaus. From the conductance maps, they found each time new mode was opened, new angular lobes of electron flow appeared and the electron flow patterns widened, and the number of lobes in the patterns equaled to the number of the QPC modes. Another interesting feature is the movement of tip alternates the constructive and destructive interference of electrons backscattered from the tip, that produced the appearance of fringes spaced by half of the Fermi wavelength in the conductance maps, indicating the presence of quantum mechanical phase coherence in the electron flow. In ref [24], the authors studied the electrons flow between two QPCs in an open system with the presence of magnetic field, i.e., imaging the phenomenon of magnetic focusing. The theoretical study of SGM experiment on QPCs can be found in reference [38]. Figure 2.5 (b) shows the coherent electron flows obtained by SGM as reported in ref [16].

Although QPCs are interesting research topics themselves (see e.g., $0.7G_0$ anomaly [39]), they are also the elements for more complex nanostructures, such as quantum dot (see below.)

2.2.2 Coulomb blockade in Quantum Dots

If a small conducting island of charges is coupled to two large electron reservoirs (source and drain contacts) by tunnel barriers, and a gate electrode is placed next to the island, the conductance as a function of gate voltage exhibits a series of peaks with extremely small conductance in between due to Coulomb blockade.

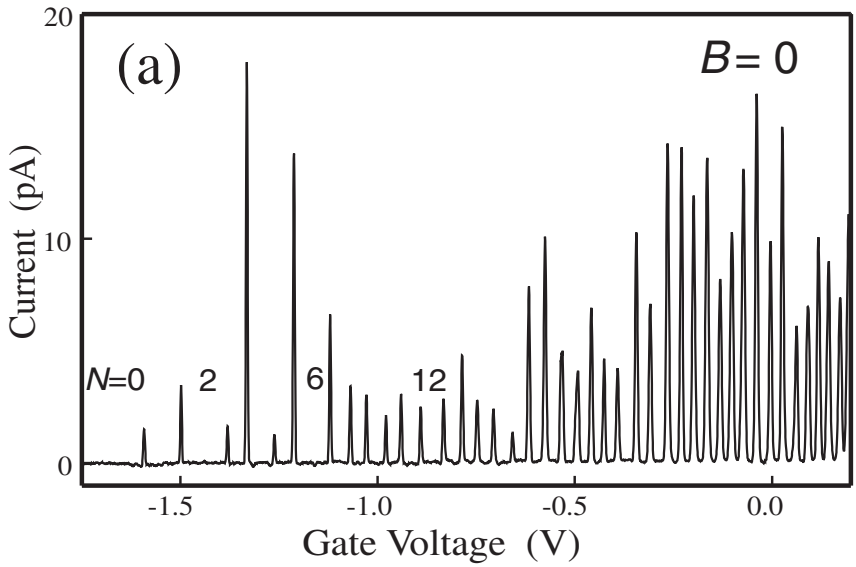

Figure 2.6: Coulomb blockage measured in double barrier heterostructure. Taken from S. Tarucha et al., [40]

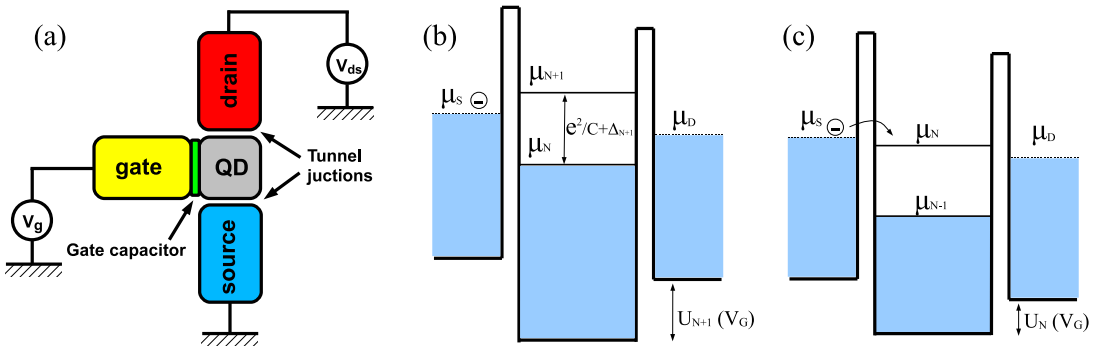

Figure 2.7: Schematics of quantum dot system. (a) Quantum dot system. (b) Electron transport is blocked and the dot contains a fixed number of N electrons. (c) The gate voltage is tuned in order to align the chemical potential in the dot with that of source and drain, transport is allowed.

One example of such results is shown in Figure 2.6. The configuration of such a quantum dot (QD) device is schematically depicted in Figure 2.7 (a).

2.2.2.1 Constant interaction from the capacitance model

In the constant interaction model, it is assumed that the total energy $E(N)$ of the island is given by the sum of its single-particle energies E_n plus the electrostatic energy $E_{\text{elstat}}(N)$:

$$E(N) = \sum_{n=1}^{N} E_n + E_{\text{elstat}}(N) = \sum_{n=1}^{N} E_n + \frac{1}{2}N^2 E_c + eN\left(\frac{Q_0^{(0)}}{C_\Sigma} - \sum_{j=1}^{N_G}\alpha_j\phi_j\right) \quad (2.19)$$

In Equation 2.19, there are a few assumptions: (i) the quantum levels can be calculated independently of the number of electrons inside the dot, (ii) the Coulomb interactions among the electron in the dot and between electrons in the dot and those somewhere else in the environment (in the metallic gates or in the 2DEG leads) are parameterized by a capacitance C, and (iii) C is independent of the number of electrons inside the dot, which is a reasonable assumption as long as the dot is much larger than the screening length (no electric fields exist in the interior of the dot) [41].

Electrochemical potential μ_N is defined as the energy required to add the N^{th} electron to the QD. We can write μ_N for a QD as

$$\mu_N = E(N) - E(N-1) = E_N + E_c\left(N - \frac{1}{2}\right) + e\left(\frac{Q_0^{(0)}}{C_\Sigma} - \sum_{j=1}^{N_G}\alpha_j\phi_j\right) \quad (2.20)$$

where N is the number of electrons, $E_c = e^2/C_\Sigma$ is the charging energy, C_Σ is the total capacitance of QD, $Q_0^{(0)}$ is the charge on QD when all the potentials are set as zero, α_j is the lever arm of gate j on QD, defined as $\alpha_\mathrm{j} \triangleq \mathrm{C_{0j}}/\mathrm{C}_\Sigma$, where $\mathrm{C_{0j}}$ is the capacitance between QD and the j^{th} gate, and ϕ_j is the potential on the j^{th} gate. The value of α_j is always positive. For metallic gates, the lever arm is well defined; however in quantum dots where regions of a 2DEG are used as in-plane gates the lever arm might change slowly as a function of the voltage applied to the gate making the relation between the chemical potential on the dot and gate voltage non-linear.

In the situation of very small bias and low temperatures ($\mathrm{eV_{bias}}$, $\mathrm{k_BT} \ll \mathrm{e^2/C_\Sigma}$), the behavior is the following. In Figure 2.7(b) transport through the QD is blocked due to the Coulomb blockade effect, with N electrons inside the

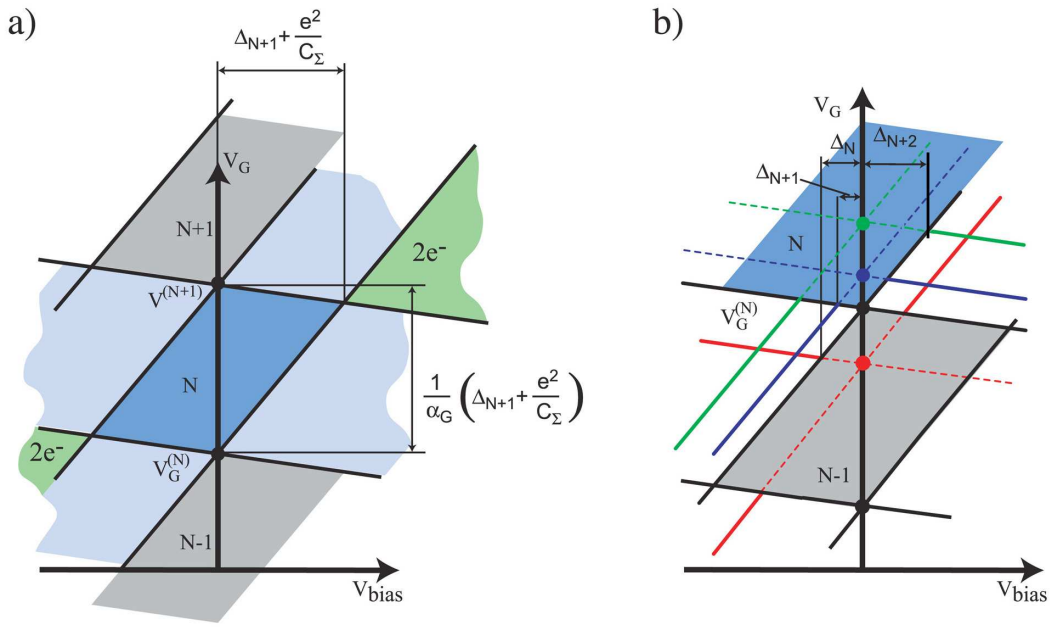

Figure 2.8: Charge stability diagrams of QD in (a) ground state, and (b) excited state. These diagrams are explained in the text.

dot. By decreasing the gate voltage, the chemical potential μ_N inside the QD is raised until it aligns with that of the drain contact ($\mu_D = \mu_N$) and an electron can leave the QD. If at the same time $\mu_s > \mu_D$ a current can flow and the number of electrons inside the QD will fluctuate between N and $N-1$. When the gate voltage further decreases and $\mu_s < \mu_N$ the dot is left with one electron less *(N-1)* and the current is again blocked.

With small bias, the conductance peak will appear when $\mu_s \approx \mu_N \approx \mu_D$. Using this to solve equation 2.20, we find the peak position is given by:

$$\phi_G^{(N)} = \frac{1}{e\alpha_G}\left[E_N + \frac{e^2}{C_\Sigma}\left(N - \frac{1}{2}\right) - e\sum_{j=1,j\neq G}^{N_G}\alpha_j\phi_j + \frac{eQ_0^{(0)}}{C_\Sigma} - \mu_s\right] \tag{2.21}$$

and the separation between two peaks is given by:

$$\Delta\phi_G^{(N+1)} = \phi_G^{(N+1)} - \phi_G^{(N)} = \frac{1}{e\alpha_G}[E_{N+1} - E_N + E_C] = \frac{1}{e\alpha_G}[\Delta_{N+1} + E_C] \tag{2.22}$$

where Δ_{N+1} is the single-particle level spacing [42].

2.2.2.2 Charge stability diagrams and Coulomb diamonds

In order to analyze a spectrum in a quantitative way it is necessary to know the value of the lever arm of the gate, which is tuned. The easiest way to determine the lever arm is by measuring the Coulomb blockade diamonds, namely current-voltage characteristics through the dot as a function of the gate voltage.

We assume that the bias is applied symmetrically to the source and drain contacts, which means $\mu_\mathrm{s} = \mu_0 + \mathrm{eV_{bias}}/2$ and $\mu_\mathrm{D} = \mu_0 - \mathrm{eV_{bias}}/2$ where μ_0 is the electrochemical potential in both contacts without an additional bias voltage. This now leads to a set of requirements for the situation where a configuration with N electrons on the dot is stable (for $V_\mathrm{bias} > 0$):

$$\mu_N < \mu_0 - eV_{bias}/2 \tag{2.23}$$

$$\mu_{N+1} > \mu_0 + eV_{bias}/2 \tag{2.24}$$

These inequalities can be translated into what we will call *borderline-equations* describing the 2 lines where the Coulomb blockade is lifted at the edge of the diamond shaped region:

$$\begin{aligned} V_G &= \frac{1}{e\alpha_G}[E_N + E_c(N - \frac{1}{2}) - \mu_0 + \frac{eV_\mathrm{bias}}{2}(1 - \alpha_\mathrm{s} + \alpha_D) \\ &\quad -e\sum_{j=1,j\neq G,S,D}^{N_G} \alpha_j\phi_j + \frac{eQ_0^{(0)}}{C_\Sigma}] \\ V_G &= \frac{1}{e\alpha_G}[E_{N+1} + E_c(N + \frac{1}{2}) - \mu_0 - \frac{eV_\mathrm{bias}}{2}(1 + \alpha_\mathrm{s} - \alpha_D) \\ &\quad -e\sum_{j=1,j\neq G,S,D}^{N_G} \alpha_j\phi_j + \frac{eQ_0^{(0)}}{C_\Sigma}] \end{aligned} \tag{2.25}$$

Here, α_s, α_D are the lever arms of the source and drain contacts. If the dot is symmetric, e.g., the tunnel barriers have the same geometry, then $\alpha_\mathrm{s} = \alpha_\mathrm{D}$ and the borderlines have exactly the opposite slope $\pm 1/2\alpha_\mathrm{G}$. The two lines cross at $\mathrm{eV_{bias}} = \Delta_{\mathrm{N+1}} + \mathrm{e}^2/\mathrm{C}_\Sigma$. The situation is shown in detail in Figure 2.8 (a). In the central diamond (dark blue region) the probability of finding N electrons on the quantum dot is unity and the dot is in a stable N-electron configuration. The light blue diamonds extending from the Coulomb peaks (black dots) denote the regions where the probability for finding N electrons on the dot is between 0 and 1 and the electron number can fluctuate by one. Further away from the gate axis (green areas), the large bias $\mathrm{eV_{bias}} > \mathrm{e}^2/\mathrm{C}_\Sigma$ allows for two electrons to tunnel at the same time. In a measurement of the differential conductance $\partial\mathrm{I}/\partial\mathrm{V}$ as

a function of DC-bias V_{bias} or gate voltage V_G the border lines will show up as peaks since this is where the current through the dot changes and a transport channel opens/closes.

Excited States

If $eV_{bias} > \Delta_{N+1}$, additional single-particle levels become accessible within the bounds given by the bias voltage and lead to an increase of the current through the dot and to additional boundary lines in the differential conductance. This is shown in Figure 2.8 (b) where for each Coulomb peak additional lines occur outside the blockade diamonds. For all the elastic processes (energy conserving regarding the dot energy) the border lines for each Coulomb blockade peak are simply shifted by the single-particle level spacings Δ/α_G along the gate voltage axis.

2.2.2.3 SGM experiments on QD

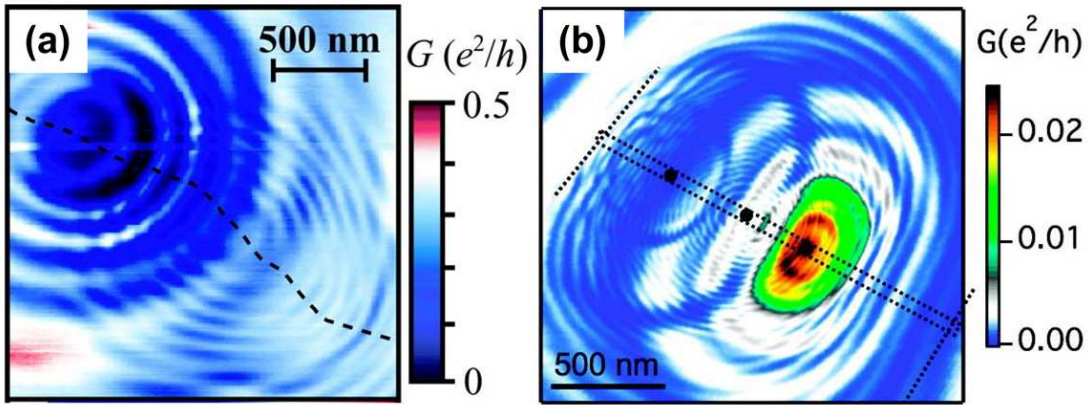

Figure 2.9: SGM images of QDs formd in CNT (a) and InAs nanowire (b). The image displays the conductance of the nanotube(wire) obtained by scanning a charged tip along the plane above the samples. Concentric rings of high conductance, corresponding to Coulomb blockade peaks, are centered on quantum dots. Taken from [18, 19].

Using the metallic AFM tip as a movable gate electrode, QDs formed in numerous different systems have been studied. In ref [18], the authors studied the QD formed in InAs nanowires. From the conductance images of the nanowire,

multiple QDs were identified along the nanowire, that each dot was surrounded by a series of concentric rings corresponding to Coulomb blockade peaks. In ref [19], the authors studied single-electron motion in carbon nanotube QDs. The number of electrons occupying the quantum dot could be changed by tuning the voltage applied to the tip, that caused Coulomb oscillations in the nanotube conductance. The positions of individual QDs were determined from the spatial maps of the oscillations. Besides, the electrostatic forces associated with single electrons hopping on and off the QD were also measured. These forces changed the amplitude, frequency, and quality factor of the cantilever oscillation, demonstrating the interaction between single-electron motion and mechanical oscillator. Figure 2.9 shows the concentric rings of Coulomb blockade peaks centered on QD formed in CNT [19] and InAs wires [18]. In ref [43], a single-electron QD was fabricated by lithography method on the AlGaAs/GaAs heterostructures containing a 2DEG. In the Coulomb blockade regime, the charged SPM tip shifted the lowest energy level in the dot and created a ring in the image corresponding to a peak in the Coulomb-blockade conductance. The energy of the electron state in the QD was determined from the fits to the line shape of the ring. In ref [44], the author fabricated a QD on AlGaAs/GaAs heterostructures by the means of local anodic oxidation. Using the QD in a given quantum state as a sensitive electrometer, the lever arm of the tip was measured. In ref [23], a superconducting single-electron transistor (SET) was measured by SGM. The shape of tip-induced potential was found to consist of a gate voltage-dependent part and a part that is independent of gate voltage. In their SGM measurements, they also revealed a dependence of the charging energy and the superconducting gap on the tip position and the voltage applied to it.

2.2.3 Aharonov-Bohm Effect in Quantum Rings

The Aharonov-Bohm (AB) effect is a quantum mechanical phenomenon in which an electrically charged particle is affected by an electromagnetic field ($\vec{E}$, $\vec{B}$), despite being confined to a region in which both the magnetic field $\vec{B}$ and electric field $\vec{E}$ are zero [45]. The underlying mechanism is the coupling of the electromagnetic potentials (V, $\vec{A}$) with the complex phase φ of the charged particle's wavefunction, and the AB effect is accordingly illustrated by interference experiments.

2.2.3.1 Magnetic AB effect

The electromagnetic theory implies that a particle with electric charge q traveling along path P in a region with zero magnetic field $\vec{B}$, but non-zero magnetic vector potential $\vec{A}$ ($\vec{B} = \nabla \times \vec{A} = 0$), acquires a phase shift φ given by:

$$\varphi = \frac{e}{\hbar} \int_P \vec{A} \cdot d\vec{l} \tag{2.26}$$

Therefore one single particle, traveling in space along two different paths with the same start and end points, will acquire a phase difference $\Delta\varphi$ determined by the magnetic flux Φ_B through the area between the paths by:

$$\Delta\varphi = \frac{q\Phi_B}{\hbar} \tag{2.27}$$

In experiment, the wavefunction of a charged particle passing around a long solenoid experiences a phase shift as a result of the enclosed magnetic field, despite the magnetic field being negligible in the region through which the particle passes and the particle's wavefunction being negligible inside the solenoid. This phase shift has been observed experimentally [46].

2.2.3.2 Electrostatic AB effect

Besides the magnetic vector potential, the phase of the wavefunction also depends upon the scalar electric potential. By constructing a situation in which the electrostatic potential varies for two paths of a particle, through regions of zero electric field, an observable AB interference phenomenon resulting from the phase shift has been predicted.

From the Schrödinger equation, the phase of an eigenfunction with energy E is $\varphi = -Et/\hbar$. The energy depends upon the electrostatic potential V for a particle with charge q. In particular, for a region with constant potential V (zero field), the electric potential energy qV is simply added to E, resulting in a phase shift:

$$\Delta\varphi = -\frac{q\mathbf{V}t}{\hbar} \tag{2.28}$$

where t is the time spent in the potential. This effect was reported in ref [47].

2.2.3.3 SGM experiment on AB effect

In ref [25], the previous PhD student in our group (F. Martins) reported the study of electron propagation inside an open quantum ring exhibiting this archetype

of electron-wave interference phenomena by the method of SGM, as shown in Figure 2.10.

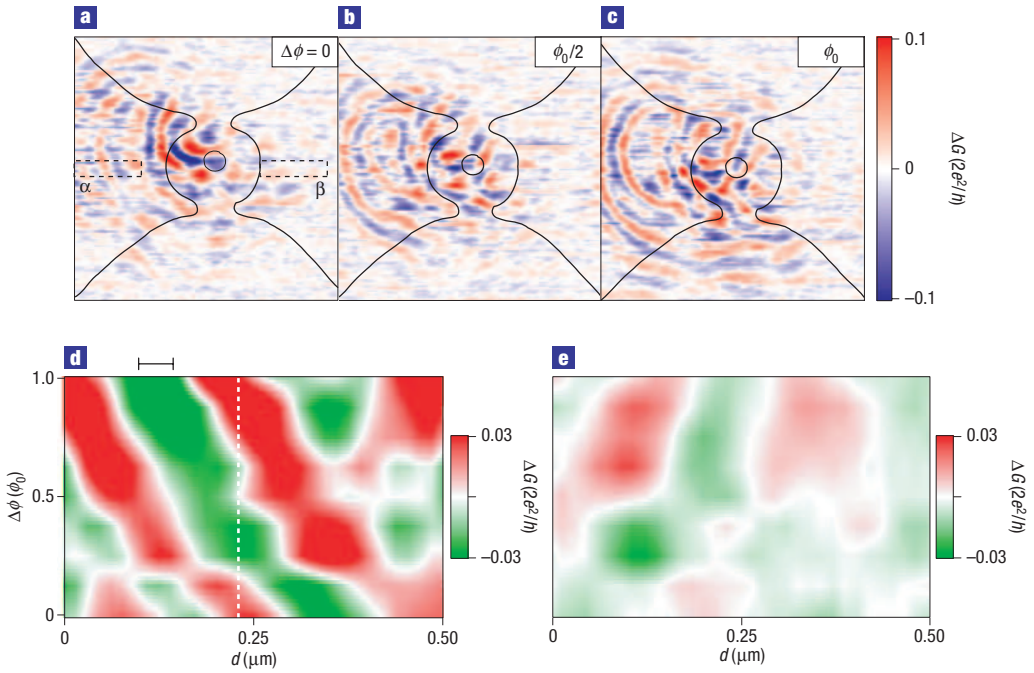

Figure 2.10: Evolution of conductance maps revealing that concentric fringes originate from the electrostatic AB effect. (a)-(c), Conductance maps recorded at increasing magnetic fields over one AB cycle, showing a continuous evolution of fringe patterns. (d)-(e), Vertical averages of horizontal conductance profiles in regions α(d) and β(e) on both sides of the QR, defined by the dashed rectangles on (a), plotted as a function of the magnetic flux, in units of the AB period Φ_0. Taken from [25].

The interpretation of the fringe patterns evolution with magnetic field is a scanning gate induced electrostatic AB effect. As the tip approaches the ring, the electrical potential mainly increases on the corresponding side of the ring. This induces a phase difference between electron wavefunctions traveling through the two arms of the ring, which causes the observed oscillations. It has to be noted that, in experiment, electric and magnetic fields ($\vec{E}$, $\vec{B}$) are non-zero inside the ring and therefore are applied to the electrons in addition to the scalar and vector potentials (V, $\vec{A}$) that appear in the theoretical analysis.

Chapter 3

Scanning probe microscope

Contents

The Atomic Force Microscope (AFM) was invented in 1986. Now, AFM is one of the most powerful tools for imaging, measuring, and manipulating materials at the nanoscale. In AFM, a silicon or silicon nitride cantilever with a sharp tip at its end is used to scan the sample surface. When the distance between tip and sample surface is small, forces between the tip and the sample lead to a deflection of the cantilever. The deflection is typically measured using a laser spot reflected from the backside of the cantilever into a position sensitive detector, e.g., quadrant photodiode.

For some special sample materials, the optical detection method is not suitable, such as for samples that are sensitive to light (photo-sensitive materials), or sensitive to the local heating caused by the light (very soft polymers). On the experimental side, the optical detection brings complexities in the construction of instruments working in cryogenic condition, because of the degraded performance of semiconductor optical sensors at low temperature.

Our experiments focus on the study of electron transport phenomena at low temperature in III-V semiconductor materials. To avoid the drawbacks of the optical detection mentioned above, we used a piezoelectric quartz tuning fork (TF) as the force sensor in our low temperature AFM.

3.1 Quartz tuning fork as force sensor

3.1.1 Commercial uses of the TF

The tuning fork was invented in 1711 by British musician John Shore. A tuning fork is an acoustic resonator in the form of a two-pronged fork with the prongs formed from a U-shaped bar of elastic metal (usually steel). It resonates at a specific constant pitch when set vibrating by striking it against a surface or with an object, and emits a pure musical tone after waiting a moment to allow some high overtones to die out.

Quartz has the advantage that its elastic constant and its size change in such a way that the frequency dependence on temperature can be very low. This made quartz oscillator widely used as high-stability frequency references. One major reason for the wide use of quartz crystal oscillators is their high quality factors (Q). A typical Q factor for a quartz oscillator ranges from 10^4 to 10^6 in vacuum. For low frequency application, crystals are typically cut in the shape of a tuning fork, such as those used in digital watches. The forks are fabricated from wafers

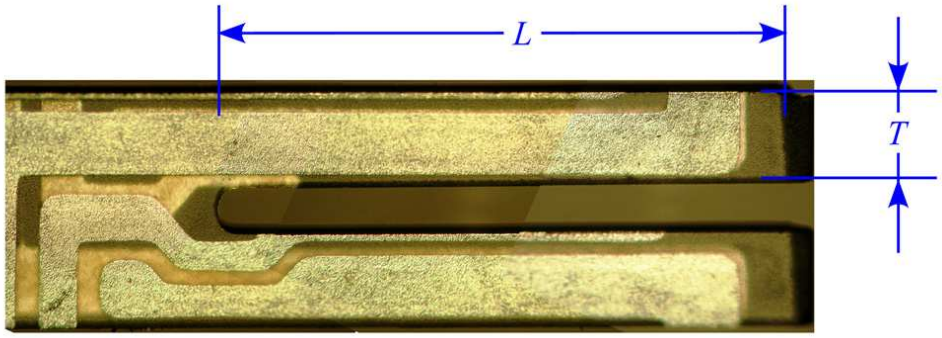

Figure 3.1: Image of the tuning fork force sensor used in our AFM setup.

of α-quartz with the optical axis (c-axis) approximately normal to the wafer plane. Because of the possibility of non-optical detection of the oscillation in the dynamic mode, and low power loss on resonance (less than 0.1μW), quartz TF is an ideal sensor for low temperature scanning force microscope.

3.1.2 Mechanical model of the TF

Some of the mechanical properties are related to the geometric sizes of TF and crystalline constants of quartz. The Young's modulus of quartz is E = 7.87 $\times$ 10^{10} N/m^2, and density of quartz crystal is $\rho = 2659$ kg/m^3. The spring constant k and resonance frequency f_0 of TF can be calculated with equations:

$$k = 0.25 \times E \cdot W \cdot \left(\frac{T}{L}\right)^3 \tag{3.1}$$

$$f_0 = \frac{3.516}{2\pi} \cdot \sqrt{\frac{E}{12\rho}} \cdot \frac{T}{L^2} \tag{3.2}$$

where W, T, L are the width, thickness and length of TF prong, as depicted in Figure 3.1. In the TF we used, L=3.80 mm, T=0.54 mm and W=0.35 mm, and we get k=2.0 $\times$ 10^4 N/m and $f_0 = 32.8$ kHz.

For small amplitude vibrations, and for simplicity, the prong of TF can be treated as a spring with constant k. The motion equation of the prong under driven signal U_0 can be written as:

$$m_0\ddot{x} + \gamma\dot{x} + kx = \alpha_{\mathrm{p}}U_0 + F_{\mathrm{ts}} \tag{3.3}$$

where α_{p} is the piezoelectric coupling constant, m_0 is the effective mass, γ is the damping constant and F_{ts} is the force exerted by the sample on the tip,

which is placed at the end of the prong as will be described in Section 3.3. Then Equation 3.3 can be re-written as:

$$\ddot{x} + \frac{\gamma}{m_0}\dot{x} + \omega_0^2 x = \frac{\alpha_\mathrm{p}}{m_0}U_0 + \frac{1}{m_0}F_\mathrm{ts}(x) \tag{3.4}$$

where $\omega_0 = \sqrt{k/m_0}$ is defined as the 'undamped angular frequency of the oscillator'. The quality factor Q relates to the damping constant via $Q = m_0\omega_0/\gamma$. Finally we get:

$$\ddot{x} + \frac{\omega_0}{Q}\dot{x} + \omega_0^2 x = \frac{\alpha_\mathrm{p}}{m_0}U_0 + \frac{1}{m_0}F_\mathrm{ts}(x) \tag{3.5}$$

For a TF without tip-sample interaction ($F_\mathrm{ts} = 0$), the solution of Equation 3.5 is:

$$x(\omega) = \frac{\alpha_\mathrm{p}U_0}{m_0(\omega_0^2 - \omega^2 + i\omega\omega_0/Q)} \tag{3.6}$$

Determination of the parameters of the mechanical model

From the discussions above, we can determine the parameters of the mechanical model as following:

$$m_0 = k/4\pi^2 f_0^2 \tag{3.7}$$

$$\gamma = 2\pi m_0 f_0/Q \tag{3.8}$$

The calculated effective mass is $\mathrm{m_0} \sim$0.48 mg ($k = 2.0 \times 10^4$ N/m, f_0=32474 Hz), and real mass of one prong is $\rho \cdot \mathrm{W} \cdot \mathrm{T} \cdot \mathrm{L} \sim 1.9$ mg.

3.1.3 Electrical detection of the TF resonance

The mechanical oscillation of TF sensor is measured via the piezoelectric effect of the quartz crystal. The induced piezoelectric charge is given by $Q_\mathrm{p} = 2\bar{\alpha_\mathrm{p}}x$, and the piezoelectric current is $I_\mathrm{p} = \dot{q_\mathrm{p}} = 2\bar{\alpha_\mathrm{p}}\dot{x}$ (The dimension of $\bar{\alpha_\mathrm{p}}$ [C/m] equals to that of α_p [N/V]). Besides, a current of amplitude $I_c = C_0\dot{U_0}$ flows through the capacitance C_0 between the tuning fork contacts. The total current as a function of angular frequency is therefore given by:

$$I(\omega) = i\omega C_0 U_0 + 2i\bar{\alpha_\mathrm{p}}\omega x \tag{3.9}$$

If we neglect the tip-sample interaction, combined with Equation 3.6, $I(\omega)$ is found to be:

$$I(\omega) = i\omega U_0 \left(C_0 + \frac{2\bar{\alpha_\mathrm{p}}\alpha_\mathrm{p}/m_0}{\omega_0^2 - \omega^2 + i\omega\omega_0/Q} \right) \tag{3.10}$$

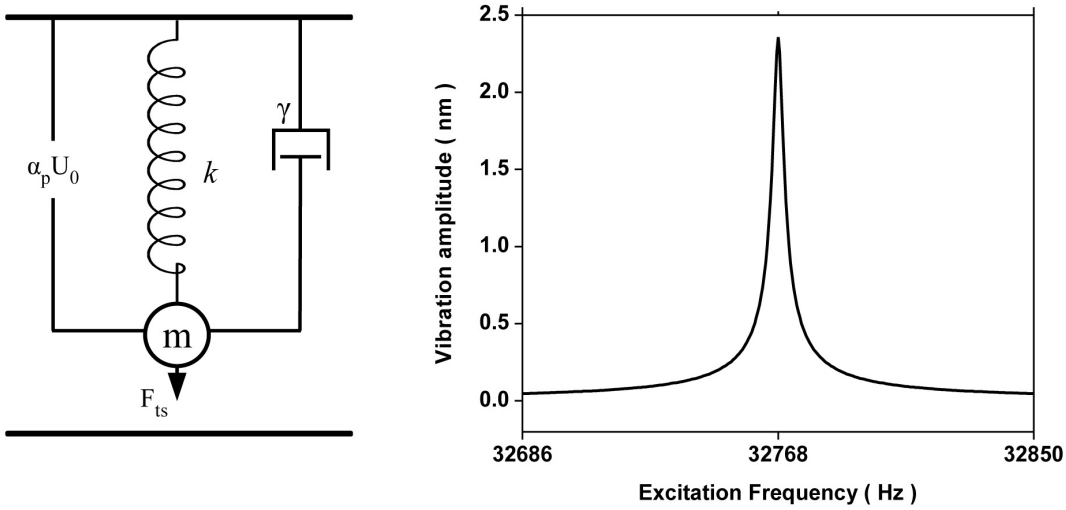

Figure 3.2: Left, the mechanical model of the TF sensor. Right, the vibration amplitude as a function of the excitation frequency simulated from Equation 3.6. The input parameters are: $\alpha_p = 5\mu N/V$, $U_0 = 1$ mV, $m_0 = 0.5$ mg, $f_0 = \omega_0/2\pi =$ 32768 Hz and Q=10,000.

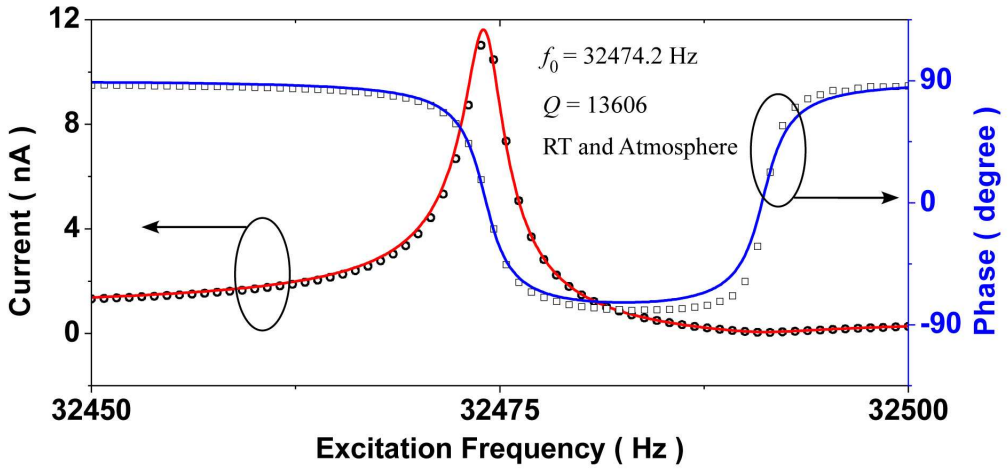

Figure 3.3: Open circles, the measured resonance curve of the TF sensor. The excitation signal (1mV_{rms}) is applied directly on the TF. Solid curves, the fitted results from Equation 3.10. The phase is defined as $\varphi = \tan^{-1}\left(\frac{\text{Im(I)}}{\text{Re(I)}}\right)$.

The recorded resonance curve shown in Figure 3.3 can be fitted with this equation. The fitted parameters are: C_0 = 3.97pF, Q=13606, f_0=32474Hz. Using m_0=0.48 mg, we get $\bar{\alpha_p}\alpha_p = 4.16 \times 10^{13}$ C^2/m^2. Since $\bar{\alpha_p} = \alpha_p$, we get $\alpha_p = 6.45$ μC/m. The displacement of TF at resonance can be estimated from Equation 3.9: with $U_0 = 1$ mV$_{rms}$ excitation applied directly on the TF, at resonance f_0=32474 Hz, the generated piezoelectric current is $I_p = 11$ nA, and the corresponding displacement is $x_{rms} \sim 4.3$ nm. By measuring the current $I(\omega_0)$ at resonance and the vibration amplitude $x(\omega_0)$ simultaneously by optical method (another TF with a tip glued at the end of one prong), we found $x = 4.2$ nm for $I = 22$ nA at $U_0 = 10$ mV.

The electrical response of the TF differs from a damped harmonic oscillator by adding a capacitance C_0 parallel to the serially connected RLC (see Section 3.1.4). The addition of C_0 results in an anti-resonance at a frequency above the resonance frequency as can be seen in Figure 3.3. The anti-resonance frequency can be calculated by: $f_a = 1/(2\pi\sqrt{LCC_0/(C+C_0)})$, ref [48].

Near resonance frequency ($\omega \approx \omega_0$), the current is dominated by the piezoelectric current, and can be expanded as:

$$I(\omega) = \frac{2\alpha_p^2 Q U_0}{m_0\omega_0}\left[1 - i\frac{2Q}{\omega_0}(\omega-\omega_0)\right] + \mathcal{O}[(\omega-\omega_0)^2] \tag{3.11}$$

The phase defined as $\varphi = \tan^{-1}[\mathrm{Im(I)/Re(I)}] = \tan^{-1}[2\mathrm{Q}(1-\omega/\omega_0)]$ is shown in Figure 3.3. The phase is used in the phase locked loop (PLL) feedback, and will be discussed in Section 3.2.

3.1.4 Electrical analogy of TF

The piezoelectric resonator could be modeled by an equivalent circuit (Butterworth-Van Dyke circuit) as shown in Figure 3.4. The LRC resonator models the mechanical resonance:

- the inductance (L) models the kinetic energy storage (effective mass);
- the capacitance (C) models the potential energy storage (spring constant);
- the resistance (R) models the damping process;
- the parallel capacitance (C_0) models the geometrical arrangement of contacts on the crystal, the dielectric properties of quartz and the cables capacitance.

The parameters of the electrical model are related to that of the mechanical model by:

$$Q_{\mathrm{p}}^2/2C = 2 \times kx^2/2 \tag{3.12}$$
$$LI_{\mathrm{p}}^2/2 = 2 \times m_0\dot{x}^2/2 \tag{3.13}$$
$$I_{\mathrm{p}}^2 R = 2 \times \gamma\dot{x}^2 \tag{3.14}$$

where the piezoelectric charge $Q_{\mathrm{p}} = 2\alpha_{\mathrm{p}}x$, and the piezoelectric current $I_{\mathrm{p}} = 2\alpha_{\mathrm{p}}\dot{x}$. Equations 3.12-3.14 indicate the potential energy, kinetic energy, and power of energy loss due to damping respectively. The calculated parameters of the electrical model are ($\alpha_{\mathrm{p}} = 6.45\mu\mathrm{C/m}$):

$$C = 2\alpha_{\mathrm{p}}^2/k = 4.2\ fF \tag{3.15}$$
$$L = m_0/2\alpha_{\mathrm{p}}^2 = 5.8\ kH \tag{3.16}$$
$$R = \gamma/2\alpha_{\mathrm{p}}^2 = 86\ k\Omega \tag{3.17}$$

In analogy to Equation 3.3, the equation describing such a circuit under an excitation U_0 can be written as:

$$L\ddot{q} + R\dot{q} + q/C = U_0 \tag{3.18}$$

The resonance frequency is $f_{\mathrm{res}} = 1/(2\pi\sqrt{LC})$, and the Q-factor is defined as: $Q = \sqrt{L/C}/R$.

The transfer function (or called as admittance) $Y(\omega) = I(\omega)/U_0(\omega) = \dot{Q}(\omega)/U_0(\omega)$ is:

$$Y(\omega) = \frac{1}{R + \frac{1}{i\omega C} + i\omega L} + i\omega C_0 \tag{3.19}$$

In Figure 3.4, (a) shows the measured current, and (b) shows the simulation obtained with the parameters listed in Equations 3.15-3.17 and $\mathrm{C}_0 = 3.97$ pF.

3.1.5 The dependence of Q-factor on temperature and pressure

The Q-factor of the TF resonator is closely related to the temperature T and pressure P. As suggested in ref [49], the Q-factor can be written in the form of $Q^{-1} = Q_i^{-1} + Q_{\mathrm{p}}^{-1}$, where Q_i is the intrinsic Q-factor and Q_{P} is the pressure-related Q-factor.

- The component of Q_{P}^{-1} decreases as the pressure decreases, i.e., at low pressure, $Q_{\mathrm{P}}^{-1} \propto P$; at high pressure, $Q_{\mathrm{P}}^{-1} \propto P^{1/2}$. This characteristic can be used to interpret the increase of Q observed in vacuum.

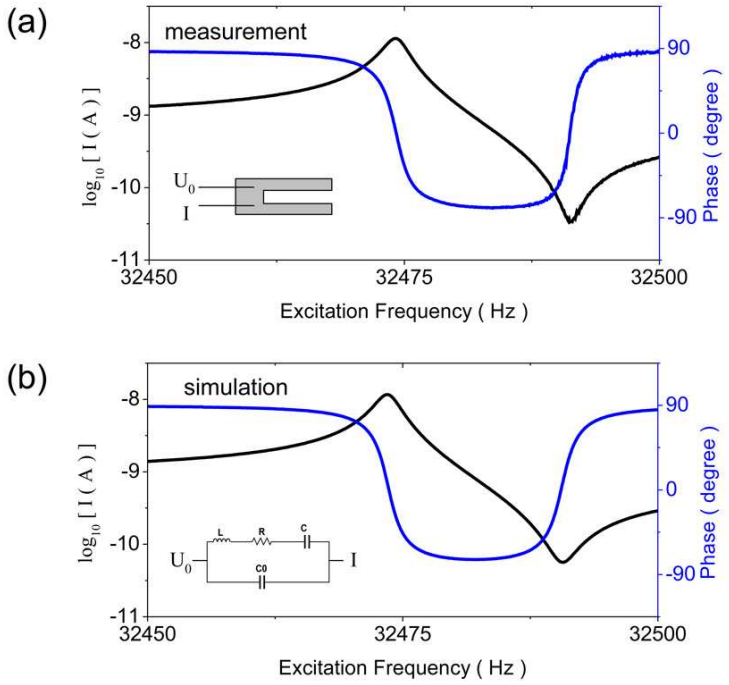

Figure 3.4: Electrical model of the TF. Left, the measurement result of resonance curve (the same data as that shown in Figure 3.3, plotted in $\log_{10}$ scale). Right, the simulation results obtained with the electrical model described in Equation 3.19, with the excitation signal of $U_0 = 1\text{mV}$.

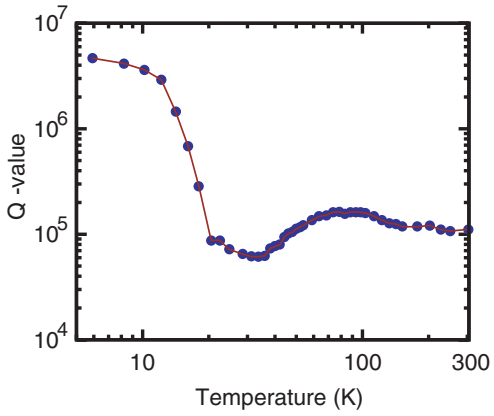

Figure 3.5: Temperature dependence of the Q-factor of a quartz TF resonator. The Q-factor changes from 10^5 to 5×10^6, when lowering the temperature from 300 to 6 K. The pressure inside the test chamber is less than 1 Pa. Taken from ref [50].

- The temperature dependence of the Q-factor results from the component Q_i. Figure 3.5 shows the temperature dependence of Q from RT to 4 K. The limitation of Q at room temperature is mainly due to the intrinsic acoustic losses. By cooling down the TF to liquid helium temperature, the contribution of acoustic losses vanishes, thus enabling an increase of the Q-factor, by almost one order of magnitude. In our case, the typical Q-factor of the TF with a tip glued on a prong is 10,000 at RT and 100,000 at LT. Theoretical studies indicate that, Q^{-1} is almost a linear function of T^4, which obeys the Landau-Rumer theory of acoustic wave absorption caused by phonon-phonon interaction in the crystal. The abnormal behavior seen in the range of 20 K to 50 K, i.e., the Q-factor becomes smaller than that obtained at RT, is due to the effect of the impurity in quartz: the ionic Na^+ impurity are responsible for a decrease of the Q-factor through interactions of the sound wave with thermal phonons [50, 51].

3.2 Frequency detection

When the tip interacts with the sample surface, the shift of the resonance frequency is much smaller than that of traditional cantilevers, because of its high spring constant. This requires frequency demodulation with high resolution. As shown in Figure 3.3, the phase signal changes by almost 180° within a range of less than 1 Hz centered at the resonance frequency. The phase change in this narrow regime is linearly dependent on the frequency (see below). This brings the possibility of detecting resonance frequency shift with high sensitivity. If one wants to use this feature as the frequency shift detection, the excitation frequency has to be adjusted by phase-lock loop (PLL) to maintain the TF working at the resonance frequency, as shown in Figure 3.6.

3.2.1 Phase Lock Loop

The region in the red rectangle shows the setup to measure the admittance of the TF. The TF is driven by the output voltage of a function generator (FG), in the range of 20 μV to 1 mV, depending on the TF Q-factor and the selected oscillating amplitude. The TF current is converted to a voltage signal by the current amplifier with a I-V gain 10^6 V/A. The output of the current amplifier is demodulated by the lock-in amplifier, which determines the in-phase (X) and 90° (Y) current components corresponding to the real and imaginary parts in Equation 3.10.

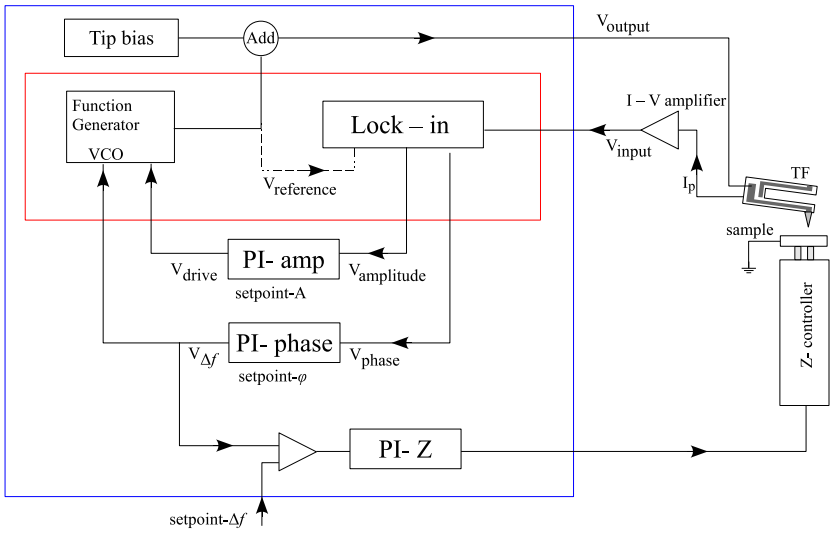

Figure 3.6: Schematic of the phase-lock loop. All the segments in blue rectangle are integrated in Nanonis Assembly. The working principle of the PLL is described in details in the text.

In practice, the outputs are amplitude A and phase φ. Near the resonance ($f - f_{\text{res}} \ll f_{\text{res}}/Q$), the phase is given by:

$$\varphi \approx -\frac{2Q(f - f_{\text{res}})}{f_{\text{res}}} \tag{3.20}$$

The phase signal is a linear indicator of the deviation of the driving frequency f from the resonance frequency f_{res}, which can be used in a feedback to maintain the TF at the resonance frequency. From Equation 3.20, we get:

$$Q = -\frac{\varphi f_{\text{res}}}{2(f - f_{\text{res}})} \tag{3.21}$$

This formula is used to determine quickly the Q-factor in the Nanonis controller software after a frequency sweep.

The PLL increases the dynamic range of the frequency detection. The phase signal of the lock-in depends linearly on the frequency shift only in a limited range of frequencies around resonance. With high-Q sensors this range can become so narrow (100 mHz under vacuum at LT) that during the tip approach or when scanning on rough surfaces the frequency shift runs out of this range. The PLL avoids this problem by tracking the resonance.

The PLL is made by feeding the phase signal into a proportional integral (PI) controller. The output of the PI $V_{\Delta f}$ is fed to the input of 'voltage-controlled oscillator' (VCO) of FG, which will adjust the output frequency of FG to the resonance frequency of TF in order to keep the phase at 0°. The output $V_{\Delta f}$ is also fed into z-feedback controller, which will first determine the difference between $\Delta f = f_{res} - f_{res}^0$ [1], and the set-point value $\Delta f_{set-point}$, and then feeds the error signal into the PI of the z-controller. Output of the PI z-controller will control the vertical motion of the scanner such as keeping constant the tip-sample interaction.

Another feature of the PLL is the control of the TF oscillation amplitude. The amplitude output A of the lock-in is fed to the amplitude modulation input of the FG via a PI controller. This feedback keeps the amplitude of the TF oscillation at a constant value by adjusting the excitation voltage amplitude on the TF. Both the drive frequency and the drive amplitude could be used in the microscope z-feedback control, but the drive frequency is usually preferred because of the high Q-factor.

3.3 Fabrication of TF sensors with a metallic tip

In SGM experiment, a metallic tip is required to capacitively couple this scanning gate to the buried 2DEG. In our experiments, we choose to glue the commercial EFM cantilever[2] directly at the very end of one TF prong (see Figure 3.7).

The commercial quartz TF is first prepared by removing the lid with pliers. Then the bare TF is glued on a small piece of PCB with insulating glue[3], and next this assembly is glued on the tip holder. If the tip will be used in an experiment under magnetic field, it's better to replace the leads of the TF that are made of magnetic wire, with a thin aluminum or copper wire, because the strong magnetic fields would inevitably induce positions shift in both vertical and horizontal directions during the SGM microscopy.

The second step is to precisely glue the cantilever on the right position. This

[1] f_{res}^0 is referred as the resonance frequency of a free TF (also called 'center frequency'), and f_{res} is referred as the resonance frequency with the presence of tip-sample interaction.

[2] NANOSENSORS™, PPP-NCHPt-20. The tip is made of n^+ silicon, and coated with Pt/Ir on both tip and detector sides. The tip height is 10 - 15 μm.

[3] Two components rapid epoxy glue, product of Araldite®.

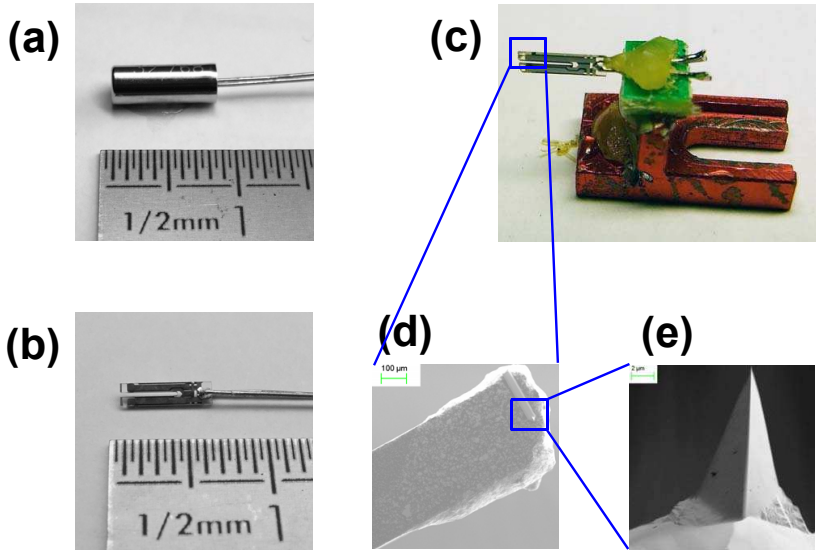

Figure 3.7: The preparation of TF sensor. (a)-(b), the TF sensor before and after the lid is removed. (c) Image of the TF sensor glued on the TF holder. (d)-(e) SEM images of the tip glued at the end of the top prong.

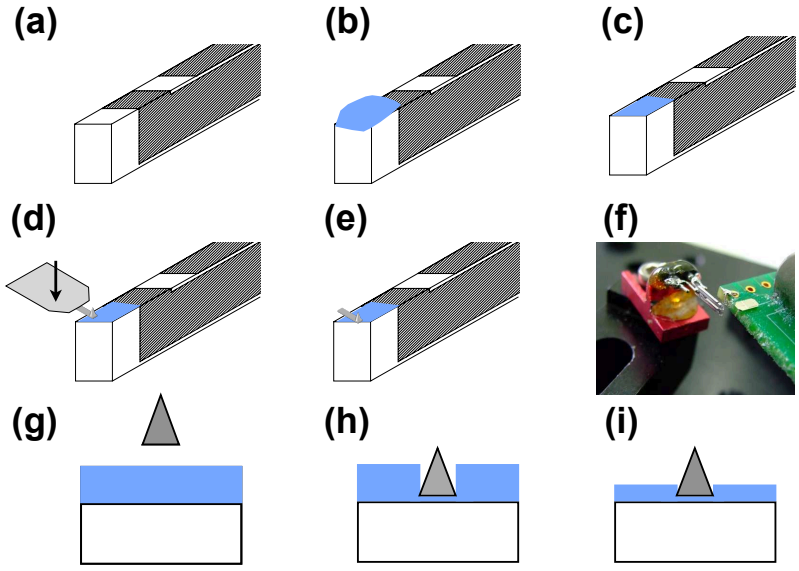

Figure 3.8: (a)-(e) Schematics of gluing commercial conductive AFM tip onto the TF sensor. (f) Image of the apparatus used for gluing the tip. (g)-(h) The relative positions between the tip and the silver epoxy, corresponding to the steps of (d-e) respectively. (i) Schematic of the reduced thickness of the silver epoxy after baking.

process was accomplished as shown in Figure 3.8, starting from the TF which was already glued on the holder:

1. Image (a) shows the metal electrode on the top TF prong;

2. Firstly we put a piece of silver epoxy on the end of the top prong. In this step, the mixture of two components of silver epoxy has to be adjusted from the suggested ratio of (1:10), to ensure that a tiny piece of such mixture could be picked up. The silver epoxy (blue parts) coated on the TF should cover a small area of the metal electrode on the surface of the TF (shadow areas), which is used as the connection between voltage source and tip, as shown in (b).

3. Then, the thickness of silver epoxy is reduced by removing most part with a thin wire, and only a thin layer is left as shown in (c), because the height of commercial tips is only about 15 μm. Steps of (b) and (c) are completed by hand.

4. Then the cantilever chip is placed on a plate with double-face tape in-between. The tip is of course facing upwards. After approaching the cantilever (with a 3-dimensional moving stage) to the end of TF, we press the cantilever downwards. The cantilever is broken off from the holder part, and stays on the state, as shown in (d) and (e). In this step, we minimize the distance from the end of TF to the tip; otherwise with a small tilted angle of TF with respect to the sample surface, the end of the TF would touch the sample before the tip.

5. (f) is the image taken before (d). All the steps (b)-(e) are done under a stereo microscope.

6. The last step is to bake the silver-epoxy (95℃ for about 2 hours in the oven). (i) shows the thickness change after baking. Since only a small piece of silver-epoxy is used, it's useful to put the residual part into the oven at the same time because it can be used to check if the silver-epoxy is baked enough and solidified already. Figure 3.7 (e) is a SEM image of a fresh tip.

3.4 Electrostatic force interaction

The two principle modes of operation of AFMs are static mode and dynamic mode. In static mode, the cantilever is moving in contact with the surface of the sample and the height profile of the surface is measured using the deflection

of the cantilever as a feedback input for the z-controller. In dynamic mode, the cantilever is externally excited at its resonance frequency. The oscillation amplitude and phase (resonance frequency and Q-factor) are modified by tip-sample interaction forces. These changes in oscillation properties provide information about the sample's characteristics.

The elastic interaction between tip and sample will shift the resonance frequency, via the presence of force gradient ($\partial F/\partial x$). Inelastic tip-sample interaction will alter the Q value. Using this assumption of force gradient [52], we can relate the frequency shift to the tip-sample interaction:

$$\Delta f = \eta \left(\frac{\partial F}{\partial x} \right) \tag{3.22}$$

where $\partial F/\partial x$ is the gradient of the tip-sample interaction force, and η is a constant function of the spring constant k of the TF. For small vibrating amplitudes, the force gradient can be regarded as constant over the whole range of vibration. Writing $F_{\mathrm{ts}} = (\partial F/\partial x) \cdot x$, Equation 3.5 becomes:

$$\ddot{x} + \frac{\gamma}{m_0}\dot{x} + \omega_1^2 x = \frac{\alpha_{\mathrm{p}}}{m_0} U_0 \tag{3.23}$$

where $\omega_1 = \sqrt{(k - \frac{\partial F}{\partial x})/m_0}$. We get the frequency shift (from the resonance):

$$\Delta f = f_1 - f_0 = f_0 \left(\sqrt{1 - \frac{1}{k}\frac{\partial F}{\partial x}} - 1 \right) \approx -\frac{1}{2k} f_0 \left(\frac{\partial F}{\partial x} \right) \tag{3.24}$$

In the case of a TF sensor, the coefficient 1/2 should be replaced by 1/4, which reflects the fact that only one prong of the TF senses the interaction, but both prongs are oscillating. We get therefore $\eta = -f_0/4k$.

For attractive force[1], $\partial F/\partial x > 0$, and for repulsive force, $\partial F/\partial x < 0$. So, attractive (repulsive) force will move the resonance frequency to a lower (higher) value. This is consistent with the frequency shift measurements that will be shown in Figure 3.19.

Electrostatic force

[1] Here we define the positive direction of force vector $\vec{F}$ and displacement vector $\vec{x}$ from the tip to the surface.

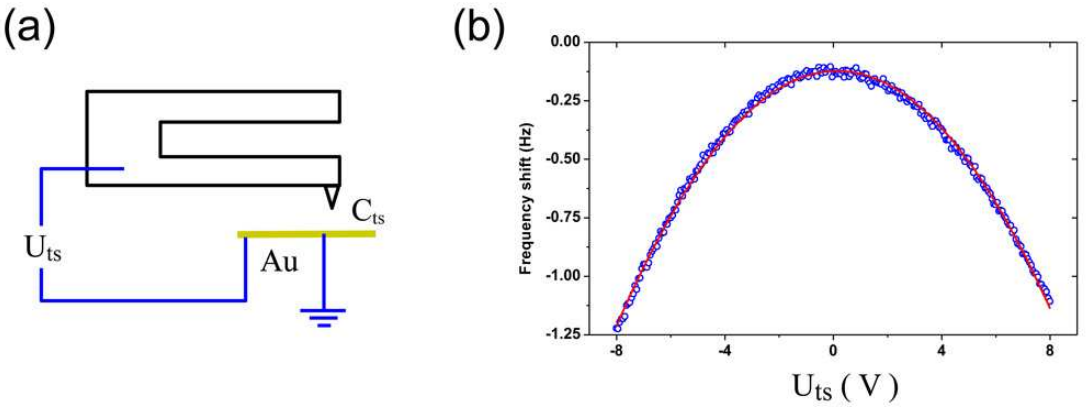

Figure 3.9: Left, schematic of the experimental configuration for the electrostatic force measurement on a gold surface. Right, measurement of the frequency shift of the TF as the tip voltage sweeps. The measurement is performed at RT and atmospheric pressure.

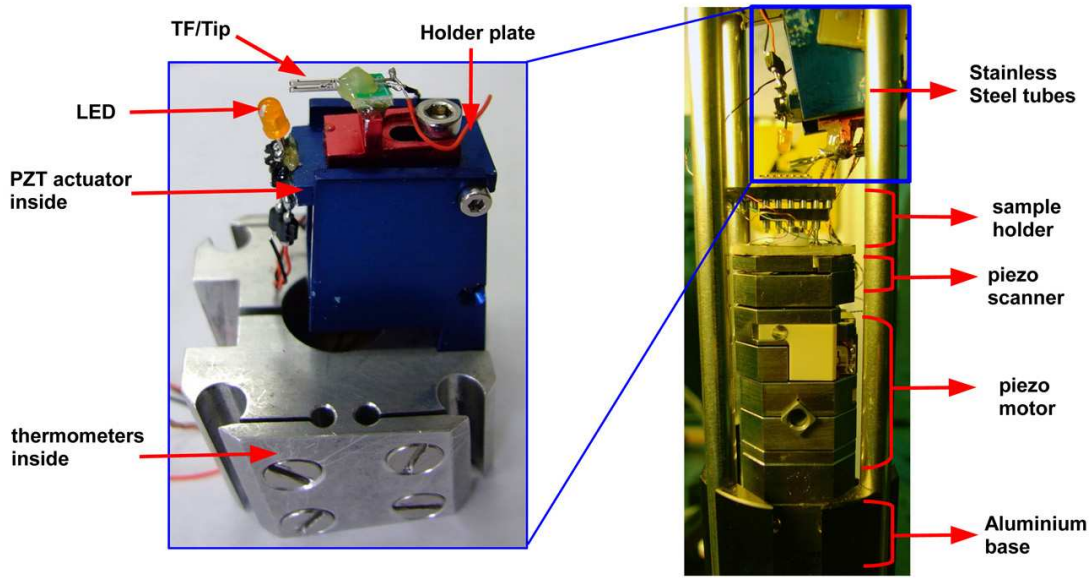

Figure 3.10: Left, image of the AFM head. Right, the piezo motor and scanner. This microscope is located at the bottom of the low temperature insert.

If a voltage U_{ts} is applied between the tip and the sample when the distance is small, an attractive electrostatic force would be built, that can be sensed by the frequency shift of the TF. The co-existence of metallic tip and conductive sample surface (or conducting 2DEG buried a few tens of nm below the surface) forms a capacitor. The capacitance value C_{ts} depends on the tip and sample geometry as well as the dielectric properties of the medium in-between. The electrostatic energy stored in the capacitor is $E = -C_{\mathrm{ts}}U_{\mathrm{ts}}^2/2$. The electrostatic force is:

$$F_{\mathrm{ts}}^{\mathrm{electrostatic}} = -\frac{\partial E}{\partial x} = \frac{1}{2}\frac{\partial C_{\mathrm{ts}}}{\partial x}U_{\mathrm{ts}}^2 \tag{3.25}$$

Because the tip and the sample surface are often made of different materials, we have to take into account the chemical potential difference $(\Delta\mu_{\mathrm{ts}}/e)$ of these materials, which is taken as equal to the difference of work functions. Then we obtain the frequency shift:

$$\Delta f = \frac{\eta}{2}\left(\frac{\partial^2 C_{\mathrm{ts}}}{\partial x^2}\right)(U_{\mathrm{ts}} + \Delta\mu_{\mathrm{ts}}/e)^2 \tag{3.26}$$

Figure 3.9 shows the measurement of frequency shift versus tip voltage for a metallic tip glued on a prong of the TF and placed above the grounded gold surface at a distance $\mathrm{d_{ts}} = 50$ nm. In the separation range [50 nm, 100 nm], the electrostatic force dominates the tip-sample interaction. The curve can be well fitted with Equation 3.26: $\Delta f = -0.016 \times (V - 0.14)^2 - 0.12$. Here we can extract the contact potential between the PtIr coated tip and the Au coated surface to be about 0.14 V. This is consistent with the low value expected for the metals[1]. The capacitance model between a metallic tip and a conducting surface/buried 2DEG will be discussed in more details in Section 4.4.

3.5 Low temperature AFM setup

3.5.1 Stainless steel tube rack

The microscope is designed for working under LT and strong magnetic field environments. Thus there are several requirements for the rack of the microscope:

- Non-magnetic materials to avoid distortion of the rack by magnetic force.
- Low thermal conductivity materials, because the bottom of the rack stays at 4.2 K and the top part is at RT, high thermal conductivity materials would bring heat to the microscope.

[1]The metal work functions: Au 5.1 $\sim$ 5.47eV, Pt 5.12 $\sim$ 5.93eV, Ir 5.0 $\sim$ 5.67eV.

- Rigidity and low vibration for AFM microscopy.

Finally non-magnetic stainless steel tubes are chosen to build the rack, connected by aluminium frames. In the design of the rack structure, tubes with different lengths are assembled to isolate the external vibration at different frequencies, and three tubes per stage are used instead of four. The total length of the microscope insert is designed such that the sample locates at the center of the superconducting magnet. In addition, the tubes are also protections for the wirings placed inside. The insert with the microscope is then fitted in a $\phi = 50$ mm stainless steel tube, sealed at the top flange and used to make vacuum or add exchange gas.

3.5.2 Piezo-motor

The coarse motion of the sample is done with three Attocube translation stages. The working principle of these translation stages is based on the slip-stick inertial motion that is the controllable use of the inertia of a sliding block. The sliding block slips along a guided rod to which it is otherwise clamped (sticking) in frictional engagement. To obtain a net step, the guiding rod is first accelerated very rapidly over a short period of time (typically microseconds) so that the inertia of the sliding block overcomes the friction. This way, the sliding block disengages from the accelerated rod and remains nearly non-displaced. Subsequently the guiding rod moves back to its initial position slowly enough so that the sliding block this time sticks to it and thus makes a net step. Periodic repetition of this sequence leads to a step-by-step motion of the sliding block in one direction. A piezo electric ceramics is used to push or pull the guiding rod and the exact sequence in the slip and stick motion is controlled by a high voltage source delivering fast voltage signals [53].

Resistive position sensors are used to monitor the movement of motors over 7 mm with a resolution of about 1 μm.

3.5.3 Piezo-scanner

Compared to our previous setup, the piezo tube scanner was replaced by a new type of scanner which uses three PZT stacks, as schematically shown in Figure 3.12 (a) and (b). With this scanner, the scanning range was increased to 26.6 μm(16 μm) in the x-y(Z) directions at room temperature and 40V, and to 30 μm(4 μm) at low temperature and 150V (40V).

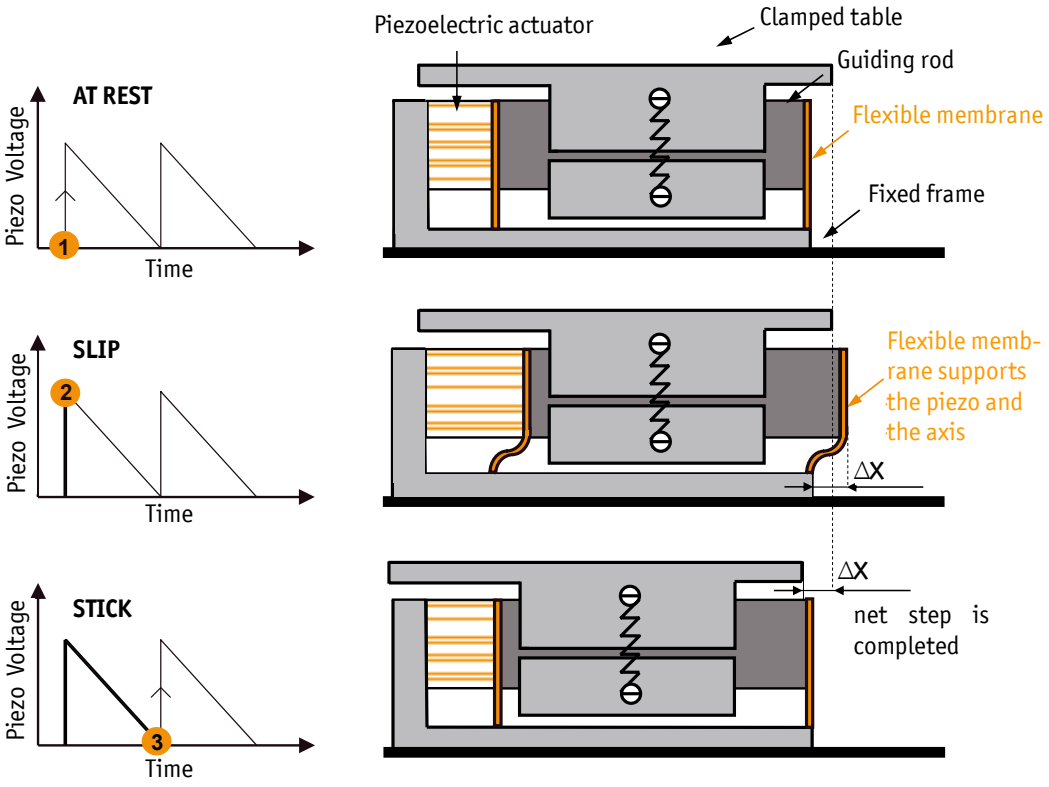

Figure 3.11: Schematics of the slip-stick driven mechanism of the piezo motor. Taken from the products catalogue of Attocube System AG.

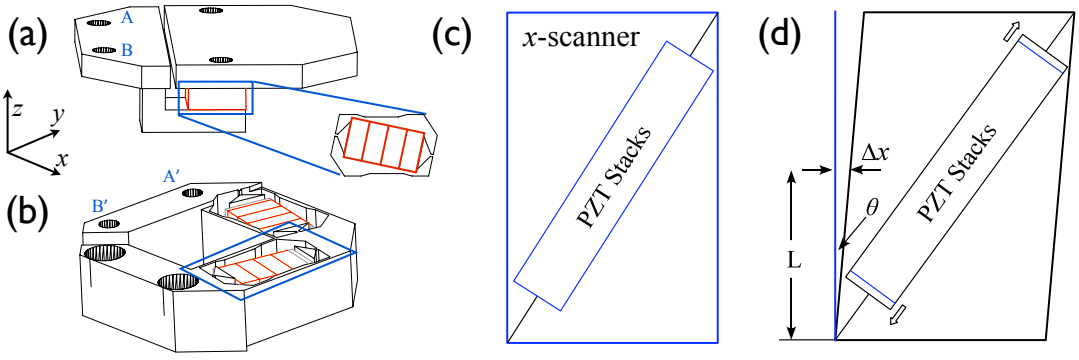

Figure 3.12: (a)-(b) Schematics of the xyz directions scanner. The z stage (a) is mounted at the end of the xy stage (b) (A-A′, B-B′). (c)-(d) Explanation of the working principle of the x-scanner.

The working principle of the scanner is schematically depicted in Figure 3.12 (c) and (d). For simplicity, the rectangle in (c) represents the wire-cut Ti metal block, marked with blue color in (b), and the PZT stacks are mounted on the diagonal of the rectangle. At zero voltage applied on the PZT stacks, the rectangle in (c) holds its original shape. If the applied voltage drives the extension of the PZT stacks, then the rectangle deforms into a parallelogram, as shown in (d).

The induced horizontal displacement $\Delta x = L \cdot \tan\theta$ where L=5 mm is the distance to the sample center. In SGM experiment, for a typical scanning range of 3μ m θ is about 0.034°. The displacement $\Delta y = L(1-\cos\theta)$ in the perpendicular direction (in y for a x-scanner) induced by the deformation of parallelogram is about 1 nm, which can be ignored.

3.5.4 Sample holder

The sample holder is a dual-in-line chip carrier mounted on a PCB plate with copper tracks obtained by etching. The layout of printing is shown in Figure 3.13. The two black circles (separated by 20 mm) correspond to the holes for mounting on the scanner plate by Ti-screws. Two rows of 7 dots (separated by 8 mm) correspond to the soldering positions of dual-in-line chip carrier. The other 8 dots correspond to the soldering positions of wirings. This sample holder is designed for the sample bounding shown in the red rectangle (there is no soldering point around the two holes, because otherwise the soldering is easily to be broken while fixing the screws).

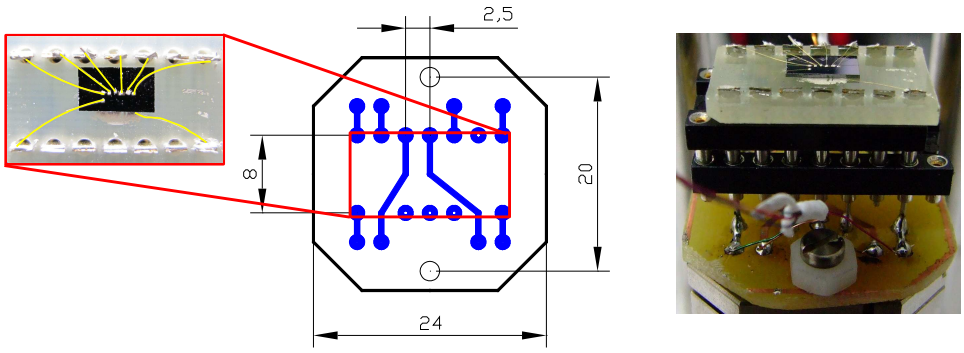

Figure 3.13: The contacts layout and image of the sample holder. Inset in red rectangle: top-view image of the sample boundings. Unit of the dimensions: mm.

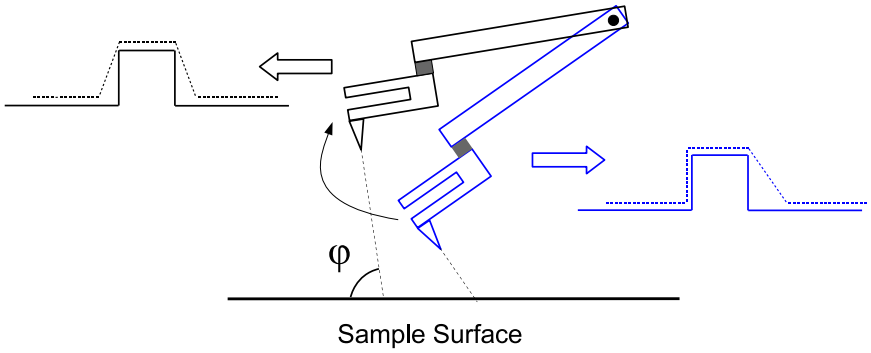

Figure 3.14: Schematics of the working principle of the TF holder plate, and consequence of the tilt on the topography profiles.

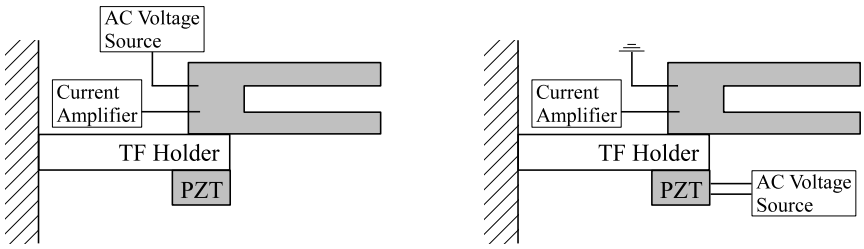

Figure 3.15: Schematics of two different methods of exciting the TF. Left, electrical excitation: the AC voltage signal is directly applied on one of the prongs of the TF. Right, mechanical excitation: the AC voltage signal is applied on the PZT stack, which is glued on the other side of the TF holder plate.

3.5.5 TF Holder Plate

The TF holder is screwed on a plate with adjustable angle φ between the tip and the sample surface (Figure 3.14). Since the tip height is only 10-15μ m, the TF cannot be placed horizontally, but should be tilted. For different tips after preparations, the tilt and position of the cantilever placed on the prong are slightly different. To minimize the topography distortion and the asymmetry of tip-induced electrostatic potential due to the tilt of tip, we tune the angle of the holder plate to adjust φ typically around 85^o.

3.5.6 Light emitting diode

The orange LED placed beside the TF is used to generate carriers in the 2DEG at low temperature. This effect will be discussed in more details in Section 4.4.

3.5.7 PZT actuator

The external excitation of the TF vibration can be an AC voltage V applied directly on the TF leads, or on a PZT actuator which transfers the AC voltage to a mechanical vibration at the same frequency (Figure 3.15). Compared with applying V on TF directly, working with PZT actuator induces distortion of the resonance curve due to a complex mechanical coupling in the assembly.

3.5.8 Thermometers

We use platinum and carbon glass resistance thermometers to control the cooling down of the microscope. The platinum thermometer is used for high T (35 K$\sim$300 K), and carbon glass thermometer is used for low T ($<$ 20 K). The relations between thermometers resistance and the temperature are shown in Figure 3.16.

3.6 Operation of the microscope in AFM mode

The operation of the microscope is conducted with the help of the Nanonis controller software shown in Figure 3.17 based on LabView program (main window ①):

1. After preparation of the tip on the TF, the resonance curve of TF should be tested to see if the contacts are working correctly. Occasionally, while

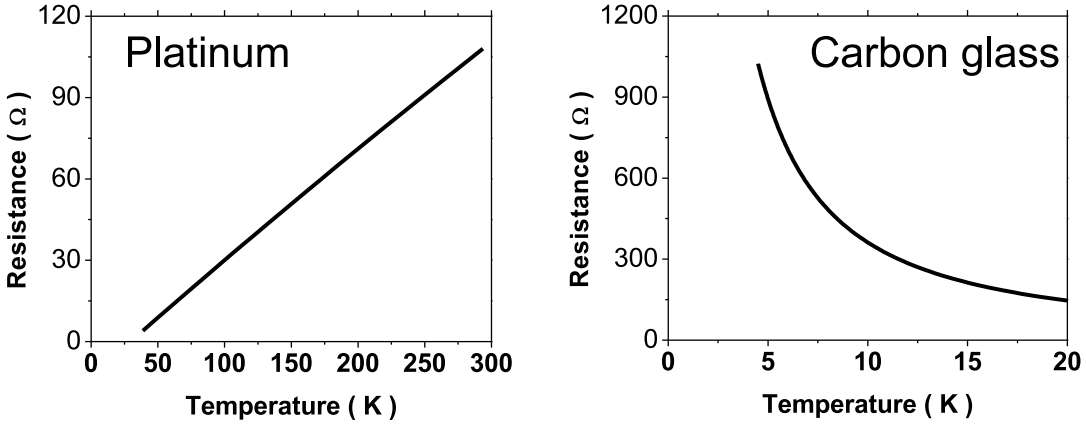

Figure 3.16: The resistance-temperature relations of the two types of thermometers used in the experiment. The working temperature range for the platinum thermometer is (35 K to 300 K), and for the carbon-glass thermometer is below 20 K.

coating silver epoxy, a tiny piece of epoxy would be left in the gap between two electrodes of the prong on the two longest edges on top surface. After baking silver epoxy this would short-circuit the two electrodes of the TF. If short-circuit occurred, the output of I-V amplifier would saturate, instead of the normal resonance curve.

2. Mount sample on the holder screw it on the scanner. Mount the TF on the holder plate and then on the rack. The TF holder plate has to be adjusted to have the tip perpendicular to the surface. The vertical distance between tip and sample is manually adjusted to be about 1mm.

3. Connect the wirings of motors (6 wires), position sensors (9), scanner (6), sample (8), TF (2), LED (2), thermometers (4) and PZT actuator (2). Check the capacitances of motors with Attocube controller[1]. At RT, the capacitance of a motor is approximately 500 nF. If one of these values is not correct (for most time, it's 0), this means some wirings are not well connected. Then, the motor wirings have to be unplugged and reassembled.

4. Approach the tip by moving the z-vertical motor upwards with Attocube controller manually. This approach is monitored by a stereo microscope[2]

[1]Model: ANC-150
[2]Leica MZ-95

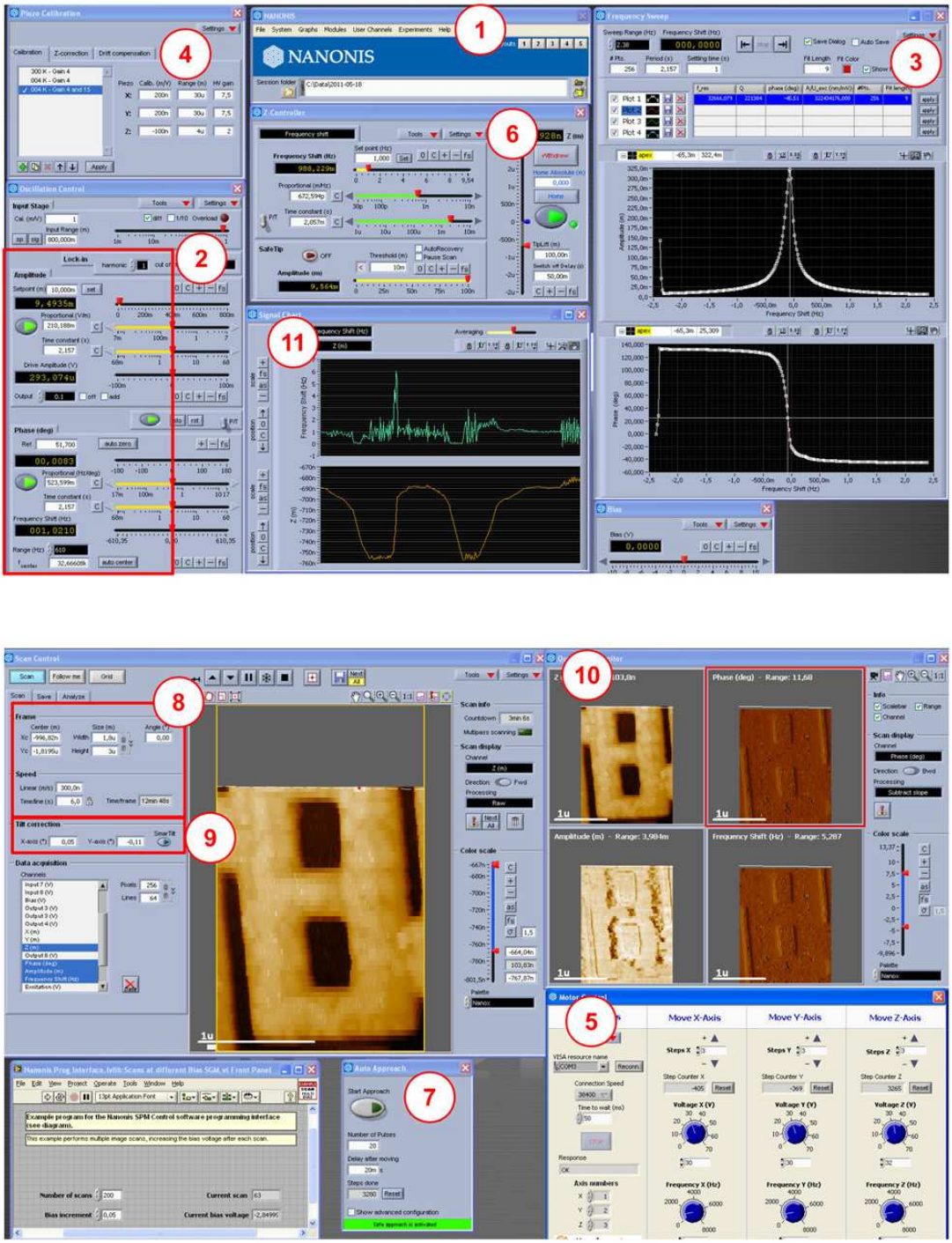

Figure 3.17: LabView program interface of Nanonis Controller software.

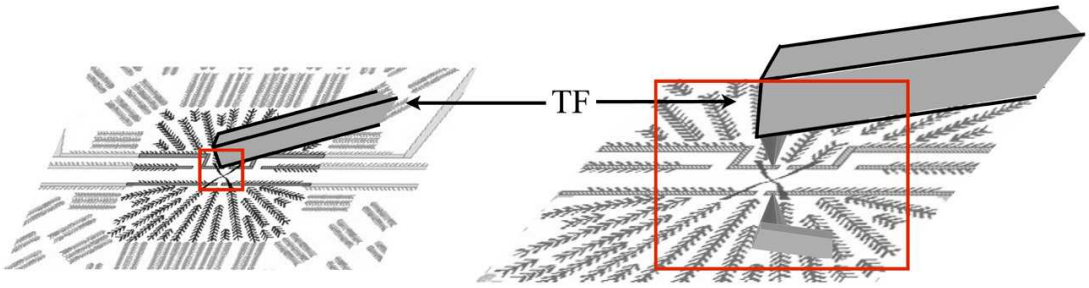

Figure 3.18: Schematic of the alignment of the tip to the central part of the sample under a stereo microscope.

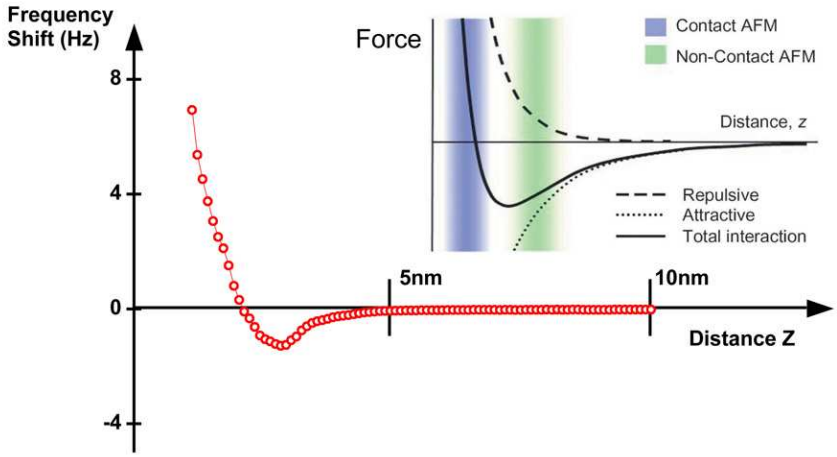

Figure 3.19: The relation between frequency shift of the TF and the tip-sample distance. As the tip-sample distance decrease, the net force experienced by the tip is first the attractive force, which might be the residual electrostatic force, and then the repulsive force, which results from the von der Waals interaction. The sign of the frequency shift can be known from Equation 3.24. The curve is recorded at 4.2 K, with electrical excitation on the TF. The excitation voltage amplitude is around 50 μV.

simultaneously. This process is schematically shown in Figure 3.18. Sometimes the tip cannot be seen in the microscope because the 'huge' (mm-size) TF prong blocks the sight. The approach is stopped when the tip is about $50\mu m \sim 100\mu m$ above the surface, which could be estimated from the distance from the apex of the tip to its mirror image seen in the sample surface..

5. Sweep the frequency and record the resonance curve. This procedure is done by sweeping the frequency of the excitation voltage applied on one of the TF prongs, and recording the amplified current (I-V gain of 10^6 V/A) generated from the other prong. The central value of the sweeping frequency (about 32 kHz for the TF) is set in the 'Oscillation Control' window ②. This step should be repeated a few times by reducing the frequency range of the sweep. One typical example of a resonance curve (amplitude and phase signals) is shown in 'Frequency Sweep' window ③ in Figure 3.17. Next, the PLL parameters are set in 'Oscillation Control' window automatically (the algorithm of determining these parameters is discussed in ref [54]). Then choose the set-point of the oscillation amplitude[1], and start on the PLL feedback of both amplitude and frequency in 'Oscillation Control' window ②. For an amplitude set-point of 10 mV, the excitation voltage applied directly on the TF is about 1mV at RT, and less than 50 μV at LT.

6. Set the high voltage (HV) gains of the scanner that amplify the 0-10 V xyz outputs. Adjust the knobs manually and set the correct HV gain in 'Piezo Calibration' window ④.

   - At RT, we use a HV gain of 4 in $x-y$ and 1 in z, the scanning range is 26μm $\times$ 26μm in $x-y$ and 4μ m in z.
   - At LT, with a HV gain of 15 in $x-y$ and 4 in z, the scanning range is 30μm $\times$ 30μm in $x-y$ and 4μ m in z.

7. Adjust the knobs of the Attocube controller to 'CCon' (computer control), and connect the serial port of the computer in 'Motor Control' window ⑤. Set the voltage and frequency of the piezo-motor steps and the number of steps for the manual approaching.

8. In 'Z Controller' window ⑥, set the parameters of the z-feedback, including a set-point of frequency shift (Δf), and the Proportional-Integral (PI) gains.

[1] Here, the amplitude is the voltage signal converted from piezoelectric current by the current amplifier.

9. Start the automatic approach of the sample towards the tip in 'Auto Approach' window ⑦. The parameters to be set here include the number of z-motor moving steps per approach sequence and the time delay between two sequences. Several sequences of z-scanner extensions and z-motor steps are repeated until the tip touches the surface (the frequency shift value reaches the set-point value).

   In Figure 3.19, we can see that the absolute value of the frequency shift increases as the tip-sample distance decrease when the tip is in contact with the surface. Thus in the feedback configuration, we set the slope of the z-feedback as 'negative', i.e., once the frequency shift increases, the distance should be decreased to maintain the set-point of the frequency shift. Note that a small region of attractive interaction can be obtained just before the repulsive contact.

10. Start the scanning. The scanning parameters include scanning area, center, speed, number of lines, number of points per line, scanning direction, angle. The recorded signals channels include frequency shift, excitation, phase, z-height, TF vibration amplitude, SGM signals, etc., see 'Scan Control' window ⑧.

11. When the topography image of a flat surface shows different heights in different positions, the tilt angle of the scanning plane has to be adjusted. This point is of extreme importance for the experiment of SGM because the z-feedback is off and the tip-induced potential is strongly dependent on the tip-sample distance. The angles in x and y directions are adjusted automatically with the help of the 'smart tilt' function ⑨. This task is completed as: the tip travels in a circular path (inscribed circle of scanning area, assuming the area is a square) several times and the tilt angle is calculated by the software to make the sample surface horizontal.

    During scanning, the built images corresponding to different signal channels are displayed in 'Quad Scan Monitor' ⑩, and the profiles of the signals can be viewed in 'Signal Chart' ⑪. An example of the signals is shown in Figure 3.20

For low temperature operation, follow the steps below:

12. Retract the sample downwards for about 150 μm.

13. Load the microscope into the stain-less steel tube (ϕ=50 mm).

14. Pump the tube until the vacuum is below 10^{-5} mbar (this step may take a few hours).

15. Inject exchange helium gas, with pressure value of 10 mbar.

16. Lower down the tube into the liquid helium bath of the cryostat progressively, such that the temperature of the microscope decreases slowly down to 4.2 K to avoid stress on the fragile piezo ceramics.

17. Repeat RT operation steps (starting at step 5). At LT, the typical driven voltage of motors is around 30 V (instead of 18 V at RT).

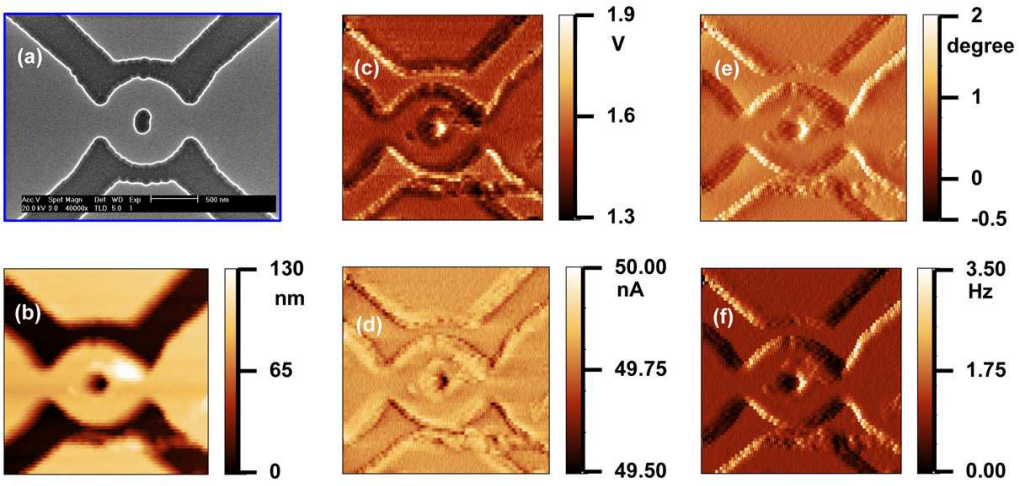

Figure 3.20: Different signals recorded simultaneously during the scanning in tapping mode. (a)-(b) SEM and topography images; (c)-(d) the excitation voltage (applied on the PZT stack) and the amplitude of generated piezoelectric current; (e)-(f) the phase and the frequency shift.

3.7 Tip shape and possible damages

To perform reliable and high spatial resolution SGM experiments, it's important to keep the tip-induced potential well localized. The shape of this potential strongly depends on the geometrical shape of the tip [55]. Thus even tiny distortions of tips would influence the final measurement results. In general, the

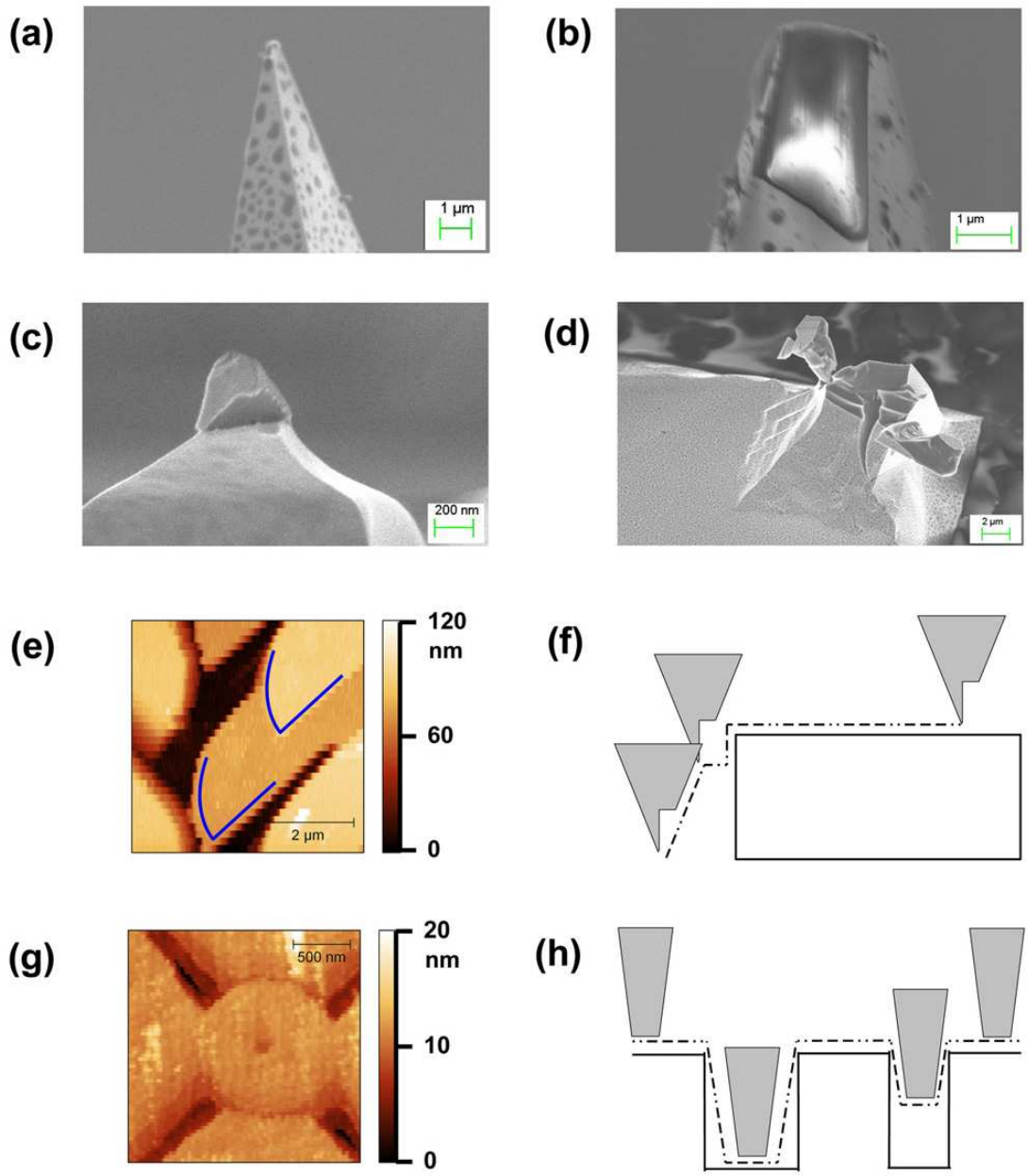

Figure 3.21: (a)-(d) Four different types of broken tips. (e)-(f) The formation of double-tip image. (g)-(h) The image and the schematic of scanning with a blunt tip.

distortions might originate from attachment of dust particles, or damages of the tips. The attachment of dust particles sometimes occurred during scanning, and could be removed by scanning with a high speed if the adhesion force was not very strong. The damages of tips could happen in a few cases:

- When the tip scanned on the surface for a long time and the apex is progressively destroyed, because Si became hard and fragile at low temperature. We can lower the risk by reducing the scanning speed and set a small vibration amplitude set-point value.

- When the parameters in the z-feedback were not set quite appropriate. With too fast gain, the z-scanner would crash the sample to the tip; but if the gain was too slow, the sample would not retract even if the tip presses strongly on the surface (For example, when the tip is scanning from the etched trench to the un-etched region).

- When electronic spikes induced sudden large upward displacement in z-direction. This might happen in both topography mode and SGM mode.

In Figure 3.21 (a)-(d), 4 typical kinds of damaged tips are shown. In (a), the tip was only damaged at the apex part and became blunted. This damage could be known if the measured depth of etched trenches were correct in large trench but smaller in thin trenches. In (b), the tip was crashed and a large piece of apex was gone. This damage could be known if the measure depths of large trenches were much smaller than the etching depth, and sometimes double-tip appeared. In (c), the apex part was broken but still dangling. This damage could be known if the topography scanning was quite unstable. In (d), the tip was thoroughly destroyed. This damage could be known if the z-feedback was very unstable.

Figure 3.21 (e) shows a typical double-tip image and a schematic of the explanation in (f). In (g), the measured depth (20 nm) of thin trenches became much smaller than the actual value (70 nm). For SGM measurement, damaging levels in (a) was acceptable, while (b)-(d) were not.

Chapter 4

Devices and SGM operation

Contents

4.1 Device Materials

In this thesis work, we used high mobility heterostructures grown by the IEMN group EPIPHY (Xavier Wallart and colleagues). Some of them are similar to those already used in the experiments on quantum rings [25, 26], and have been used in the experiments on the constriction and quantum dot. We also tried new types of heterostructures to change the electronic properties, including structures with a back gate, that enables us to modulate the carriers density and Fermi wavelength (λ_F) by tuning the voltage applied on the back gate (V_{bg}).

4.1.1 InGaAs/InAlAs heterostructures

In the work on the constriction (Section 4.5) and the QD (Section 5.1), the devices are made from 'standard' InGaAs/InAlAs heterostructures on insulating InP substrate. The epitaxially grown layer structure is shown in Figure 2.1. The electronic property of such heterostructure is characterized by magnetoresistance measurement, as shown in Figure 2.3. The extracted sheet carriers density and mobility are $n_H = 1.62 \times 10^{12}$ cm^{-2}, $n_{SdH} = 1.6 \times 10^{12}$ cm^{-2}, and $\mu_H = 77,700$ cm^2/Vs. Using the effective mass $m^* = 0.05m_e$ in $In_{0.75}Ga_{0.25}As$, from the n_H and μ_H, we calculate scattering time $\tau_m = 2.23$ ps, Fermi wavelength $\lambda_F = 2\pi/k_F = 19.7$ nm, Fermi velocity $\upsilon_F = \hbar k_F/m^* = 7.30 \times 10^5$ m/s, Fermi energy $E_F = \hbar^2 k_F^2/(2m^*) = 76.6$ meV, elastic mean free path $l_e = 1.63\,\mu m$ and diffusion constant $D = 0.59\,m^2/s$.

4.1.2 Back gate controllable samples

In semiconductor nanostructures, it is often useful to use back gate to control the transport properties of electrons, e.g., the on/off of nanowire field-effect transistors [56], or chemical potential in QD [57, 58]. In SGM studies, λ_F is a characteristic length which is closely related to the observations [16]. With this motivation, we designed a new type of heterostructure, based on the previously used samples, but using a doped InP substrate.

The layers sequence and energy band diagram are shown in Figure 4.1 (a) and (b). First the buffer layer of InAlAs was grown directly on InP. Electrical characterization of the barrier between 2DEG and back gate indicates there is a significant leakage from the 2DEG channel to the back gate, as shown in (c). By lowering the temperature, the leakage current decreased on negative side of V_{bg} while on positive side the variation was smaller. This polarity dependence of the

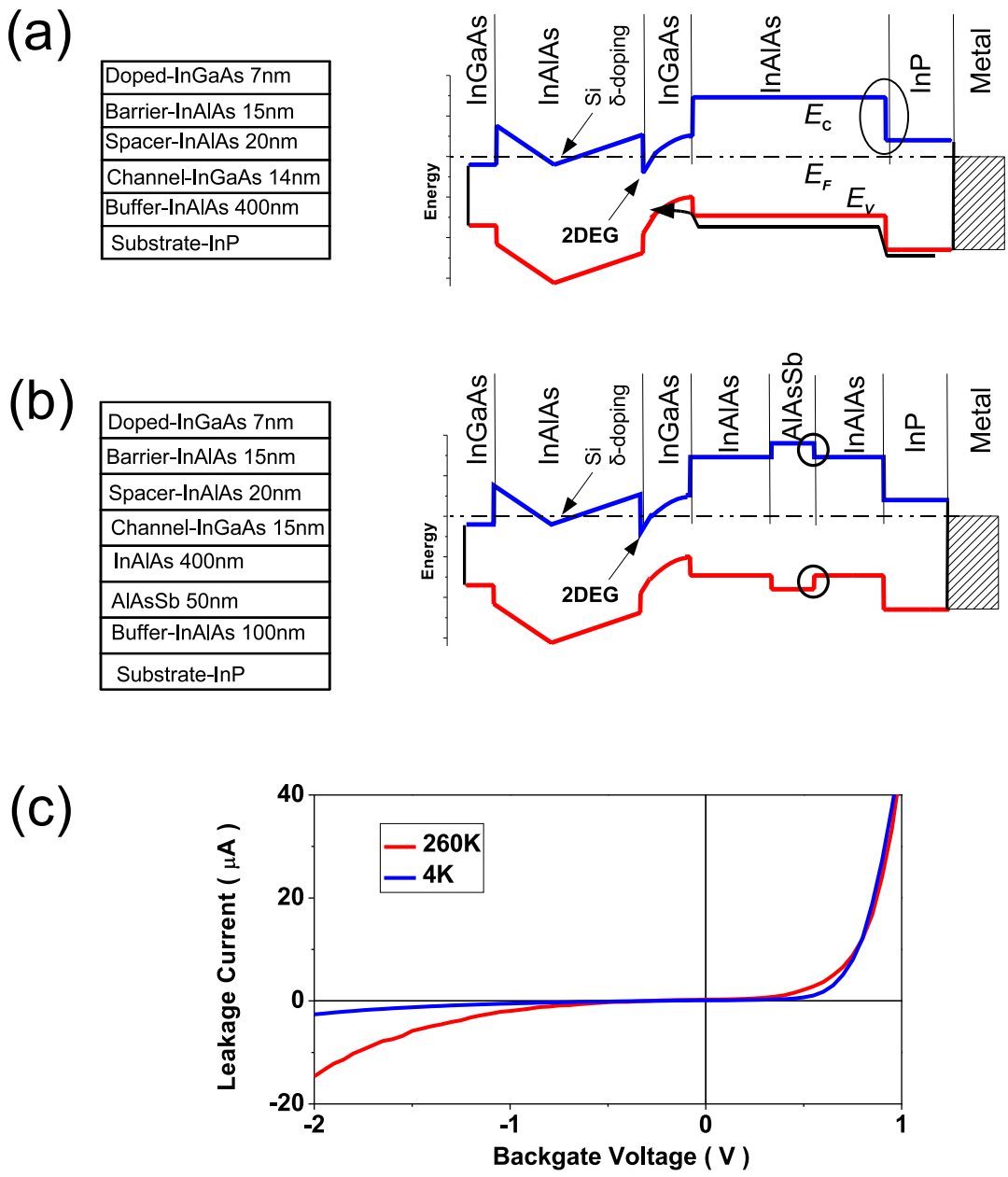

Figure 4.1: InGaAs/InAlAs heterostructures energy band diagrams with (a) doped InP substrate; (b) doped InP substrate and AlAsSb barrier. (c) Test of leakage current from the back gate to the 2DEG channel.

leakage current can be interpreted with the help of the energy band diagram in (a): for negative gate voltage, when V_{bg} is small, the barrier in the conduction band formed at the InAlAs/InP interface (solid circle) is high enough to prevent electrons to flow from the substrate to the 2DEG channel. For positive gate voltage, there is no barrier for holes in the valence band. When the back gate is positively biased, thus a hole current flows to the channel, as schematically depicted with the curved arrow. Due to the leakage, this sample could not be used in SGM experiments.

Then, the structure was modified by placing an additional AlAsSb layer with a larger energy band gap, inside the InAlAs buffer, as shown in (b). Consequently, an additional barrier is formed at AlAsSb/InAlAs interface, in both conduction and valence bands, marked by solid circles. In this sample, we did not find any observable leakage current in the range of V_{bg} [−1.0V, +1.0V].

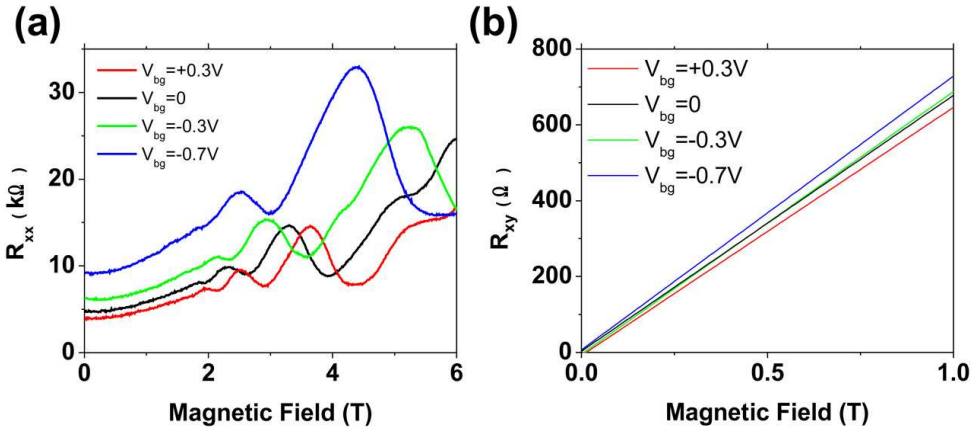

Figure 4.2: (a)-(b), Magnetoresistance measurements on the heterostructure of Figure 4.1 (b).

Table 4.1: The extracted n_{SdH}, μ_{SdH}, n_{Hall} and calculated $n_{parallel}$ from magnetoresistance measurement shown in Figure 4.2.

V_{bg}	n_{Hall} (10^{11} cm^{-2})	n_{SdH}	$n_{parallel}$	μ_{SdH} (10^5cm^2/Vs)
+0.3 V	9.55	3.95	5.6	1.05
0	9.27	3.52	5.75	1.04
-0.3 V	9.03	3.24	5.79	0.96
-0.7 V	8.67	2.83	5.84	0.81

The growth parameters of this sample were chosen by our collaborators in IEMN Lille, from their experiences, such as to make the 2DEG carriers density around the value of 1.2×10^{12} cm^{-2}. However, the density that we determined from Shubnikov-de Haas oscillations n_{SdH} deviated a lot from the designed value, as we measured 3.5×10^{11} cm^{-2}. We also find a Hall density n_{Hall} 2.5 times larger than n_{SdH}. We speculate there exists a parallel conducting layer with density $n_{parallel} = 5.7 \times 10^{11}$ cm^{-2} with lower mobility, that could be the capping layer($n_{cap} \sim 6 \times 10^{18}cm^{-3} \times 7$nm $= 4.2 \times 10^{11}$ cm^{-2}). To extract the mobility $\mu_{parallel}$, we fitted the upward curvature of the magnetoresistance with Equation 4.2 (explained later), and found $\mu_{parallel} = 100 \sim 200 \cdot$ cm^2/Vs[1]. The modulated carriers density and mobility obtained for some V_{bg} values are listed in Table 4.1. The dependence of $n_{parallel}$ on V_{bg}, with $n_{parallel}$ increasing when V_{bg} decreases, is not clearly understood.

4.1.3 Sb based heterostructures

Our collaborators at IEMN in Lille developed new type of heterostructures containing Sb element. The $Al_{0.56}In_{0.44}Sb/Ga_{0.5}In_{0.5}Sb$ system is depicted in Figure 4.3.

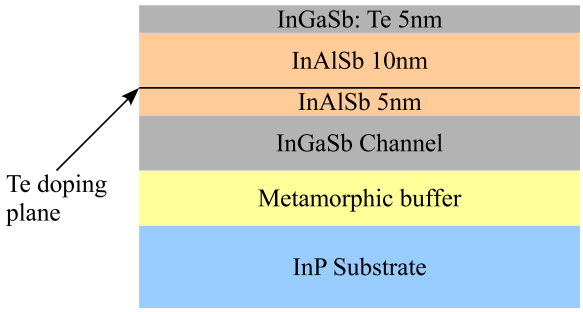

Figure 4.3: The epitaxial layers sequence of $Al_{0.56}In_{0.44}Sb/Ga_{0.5}In_{0.5}Sb$ heterostructures. The thickness of InGaSb channel is 25nm, 15nm and 10nm for the sample S090309, S090705 and S090706 respectively.

As indicated in Chapter 2, when the carriers density is high, subbands with larger index ($j > 2$ in Equation 2.2) are occupied. The occupation of the second subband was observed in this sample by means of photoluminescence spectroscopy [59].

[1] In this fitting, we used n_{SdH}, $n_{parallel}$ and μ_{SdH} as the fixed parameters.

To measure the density of the second electron subband in this sample, we performed magnetotransport measurements at 4 K in a square Van der Pauw geometry. The measured R_{xx} and R_{xy} resistances are shown in Figure 4.4.

- For S090309, the SdH density ($n_{SdH} = 1.29 \times 10^{12}$ cm^{-2}) is lower than the Hall density ($n_H = 1.55 \times 10^{12}$ cm^{-2}), indicating that a second subband is populated. This is also visible in the shape of the SdH curve, going up with increasing field, and in the shape of the Hall resistivity, going down with increasing field (a more evolved analysis will be used below to extract the density of the second subband). The Hall mobility $\mu_H^{4K} = 43,400 \text{cm}^2/\text{Vs}$ deduced from the Hall density is therefore artificially low. The SdH density gives indeed a mobility of $\mu_{SdH}^{4K} = 52,000 \text{cm}^2/\text{Vs}$, consistent with the value found by IEMN at 77 K $\mu_H^{77K} = 52,000 \text{cm}^2/\text{Vs}$.

- For S090705, the SdH density ($n_{SdH} = 1.65 \times 10^{12}$ cm^{-2}) is equal to the Hall density ($n_H = 1.64 \times 10^{12}$ cm^{-2}), but a second subband could be populated with a low mobility. This is visible in the shape of the SdH curve, going up with increasing field, but not in the shape of the Hall resistivity, showing a straight line with increasing field. It is not guarantied that the more evolved analysis below could give the density of the second subband.

- For S090706, the SdH density ($n_{SdH} = 1.90 \times 10^{12}$ cm^{-2}) is equal to the Hall density ($n_{SdH} = 1.91 \times 10^{12}$ cm^{-2}). Probably that only the first subband is populated since the shape of the SdH curve and the shape of the Hall resistivity correspond roughly to the single subband model.

We perform a more evolved analysis assuming that the two-dimensional resistivities (assuming no Landau level formation) are given by [60]:

$$\rho_{xx} = (D_1 + D_2)/[(D_1 + D_2)^2 + (A_1 + A_2)^2] \tag{4.1}$$
$$\rho_{xy} = (A_1 + A_2)/[(D_1 + D_2)^2 + (A_1 + A_2)^2] \tag{4.2}$$

where D_i and A_i (i=1 or 2) are two sets of parameters for the two subbands given by:

$$D_i = en_i\mu_i/[1 + (\mu_i B)^2] \tag{4.3}$$
$$A_i = en_i\mu_i^2 B/[1 + (\mu_i B)^2] \tag{4.4}$$

where e is the electron charge, $n_{1(2)}$ and $\mu_{1(2)}$ the electron sheet density and mobility on the first (second) subband and B the applied magnetic field. This model predicts an increase in ρ_{xx} and a decrease in the ρ_{xy} slope versus field, as

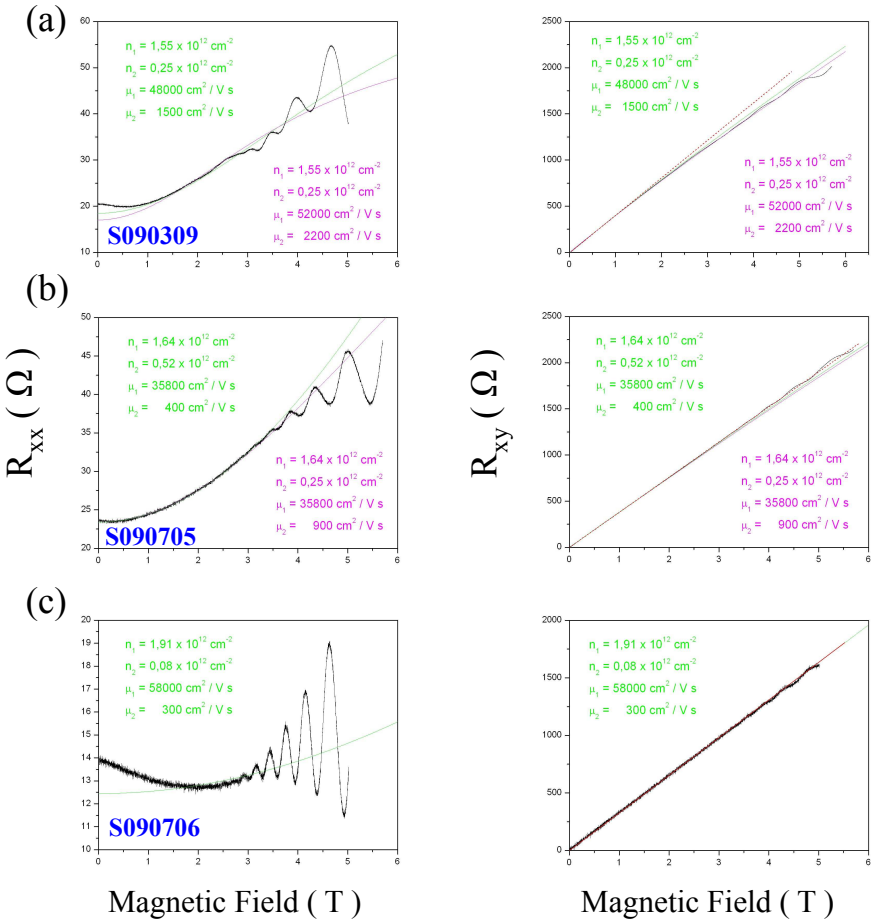

Figure 4.4: Magnetoresistance measurements on the different heterostructures of $Al_{0.56}In_{0.44}Sb/Ga_{0.5}In_{0.5}Sb$ with different 2DEG channel thickness (25 nm, 15 nm and 10 nm for S090309, S090705 and S090706 respectively). The samples were biased with AC current $I_{AC} = 10\mu A$.

Table 4.2: Carriers density and mobility of the different heterostructures of $Al_{0.56}In_{0.44}Sb/Ga_{0.5}In_{0.5}Sb$.

Sample	Channel thickness	n_1 (cm^{-2})	n_2	μ_1 (cm^2/Vs)	μ_2
S090309	25 nm	1.55×10^{12}	0.25×10^{12}	$\sim 50\,000$	$\sim 1\,800$
S090705	15 nm	1.64×10^{12}	$\sim 0.38\times10^{12}$	35 800	~ 650
S090706	10 nm	1.91×10^{12}	~ 0	58 000	~ 300

compared with the single subband model. It is indeed the case in the samples (see Figure 4.4). The experimental data (R_{xx} and R_{xy}) are fitted by adjusting D_i and A_i parameters, their respective values being summarized in Figure 4.4.

For S090309 and S090706, the decrease of R_{xx} resistivity at low field cannot be explained with the above model and the fit are therefore difficult to make. For S090705, the fit is better with this respect, but is worse for the R_{xy} resistivity which is perfectly linear.

- For S090309, the two densities seems robust versus fitting, but the mobilities are not robust, due to the problem mentioned above, therefore two fitting results are proposed for the mobilities.
- For S090705, the values of the first subband seems robust, but those of the second are not, and two fitting results are proposed.
- For S090706, the values of the first subband seems robust, but those of the second are too small to be determined, so the density of the second subband can be set at zero.

These values are listed in Table 4.2.

4.2 Device Fabrication

Starting from the heterostructure grown on a 2-inch wafer at IEMN, the process is done either at Université Catholique de Louvain (by Benoît Hackens) or in Grenoble at the PTA (by Hermann Sellier and Helge Haas).

4.2.1 Process in Louvain

1. Wafer dicing by diamond scriber
2. Cleaning by acetone, ethanol and deionized (DI) water
3. Drying
4. Spin coating of Poly(methyl methacrylate) (PMMA)
5. Pre-baking of PMMA
6. Device pattern by electron beam lithography (EBL) system (Philips FEG EBL + Raith laser x-y stage)
7. Post-baking of PMMA
8. Development and rinsing

9. Wet etching: mixture of $H_3PO_4 : H_2O_2 : H_2O = 1 : 5 : 40$ (volume ratio), the etching speed is about 150 nm by 30s
10. Removing the residual PMMA by acetone
11. Cleaning by acetone, ethanol and DI water
12. Drying
13. Spin coating of Poly(methyl methacrylate) (PMMA)
14. Pre-baking of PMMA
15. Alignment and pattern contact pad by EBL (marks for alignment are patterned in step 5)
16. Post-baking of PMMA
17. Deposition of metals by e-beam evaporation: from the sample surface, the metal layer sequence is Ni 2.5 nm, Ge 40 nm, Au 80 nm, Ni 5 nm and Au 20 nm
18. Lift-off and rinsing
19. Annealing by Rapid Thermal Annealing (RTA) System. The temperature is ramped as: 150℃ 5s, ramped up to 250℃ in 5s, 250℃ 5s, ramped up to 315℃ in 5s, 315℃ 25s, ramped down to 100℃ rapidly.
20. Wet etching of capping layer (heavily doped InGaAs): the solution is prepared as (1) weigh 50 g of succinic acid in a 400 ml beaker; (2) put 125 ml of DI water and 30 ml of NH_4OH 25% in a second beaker (3) pour this mixture in the first beaker, containing the succinic acid, and mix the solution (4) put a pH-meter in the solution (5) add 120 ml of DI water (6) add 5 ml of NH_4OH 25% (7) measure the temperature (it should be around 32℃) and the pH (it should be around 4.9 or below) (8) wait for the solution to cool down to around 22℃ (if this is the room temperature) (9) Add small quantities (about 2 ml each time) of NH_4OH 25%, until reaching pH=5
21. Gluing the die on plastic chip carrier with (1) insulating paste for non-backgate devices; or (2) silver epoxy for backgate devices
22. Connecting wires from die to lead frame with silver epoxy manually
23. Baking the sample to solidify silver epoxy in oven

4.2.2 Process in Grenoble

1. Wafer dicing into about (8mm × 8mm) size with a diamond scriber machine
2. Cleaning by acetone, isopropanol and deionized (DI) water
3. Drying

4. Spin coating of UV5 DUV photoresist (4,000 rps, 60s). The thickness is 500 nm.
5. Pre-baking of UV5 (130℃, 90s)
6. E-beam lithography of alignment marks and contact pads with JEOL 6300FS (100 kV, 1 nA, dose=60 $\mu C/cm^2$)
7. Post-baking of UV5 (135℃, 60s)
8. Development in AZ 326MIF (50 s) and rinsing in DI water
9. Deposition of metals by e-beam evaporation: from the sample surface, the metal layer sequence is Ni 2.5 nm, Ge 40 nm, Au 80 nm, Ni 5 nm and Au 30 nm
10. Lift-off in acetone and rinsing
11. Annealing in vacuum in a furnace. The temperature ramp sequence is the same as the process in UCL.
12. Spin coating of ZEP-520A photoresist (4,000rpm, 60s). The thickness is 360nm.
13. Baking of ZEP-520A [180℃, 5min]
14. E-beam lithography of 4 devices on the same sample with alignment on marks (100 kV, 1 nA, dose=300 $\mu C/cm^2$)
15. Development (MIBK:IPA=1:1, 60s) and rinsing (MIBK:IPA=89:11, 15s)
16. Reactive ion etching (RIE) at LETI/DEOPT: gas flow $SiCl_4$ (3sccm) + Ar (75sccm), pressure=15 mTorr, power=37 W. The etching speed of the heterostructure is about 45 nm for 5 min, and 100 nm for 10 min
17. Removing ZEP-520A in acetone.
18. Dividing the chip into 4 devices with a dicing machine
19. Gluing the die on plastic chip carrier with insulating paste for non-backgate devices
20. Connecting wires by bonding machine.

After RIE, we found that a re-deposition layer appeared around the etched areas, shown as the bright parts in Figure 4.6(a). The formation process is schematically depicted in (b)-(d). During the RIE, etched materials are deposited on the sidewalls of trenches as well as the sample surface. EDX analysis indicates that the re-deposition layer contains Indium (from In-rich $In_{0.75}Ga_{0.25}As$), and chlorides compound (from $SiCl_4$). And from the shallow pattern in Figure 4.7(e), we also speculate the re-deposition layer contains the O element. We tried to remove this layer by DI water in ultrasonic cleaner, or by ion beam etching, but we did not succeed. This layer was problematic for the SGM experiment (as discussed in Section 5.1).

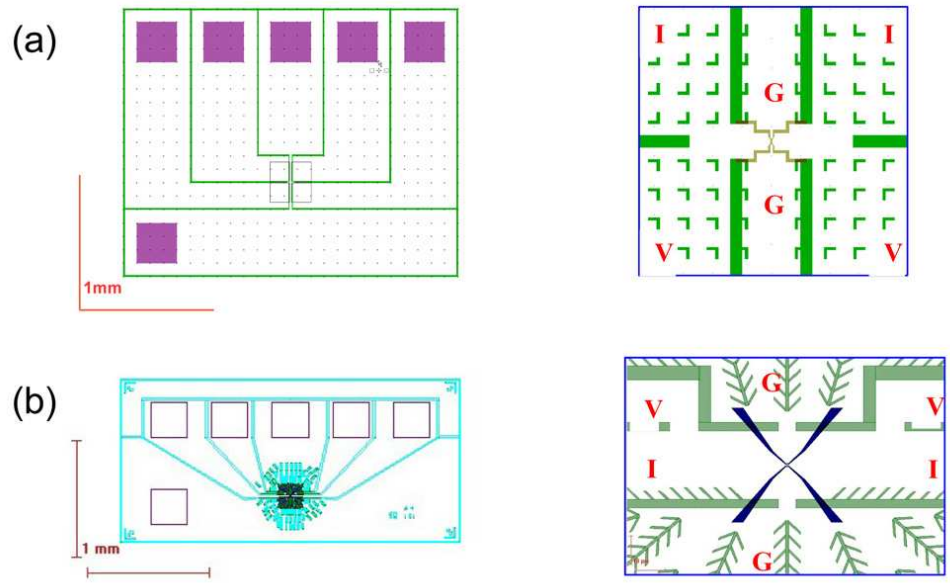

Figure 4.5: EBL layouts used in Grenoble (a) and UCL (b). The arrows are used for guiding the scanning probe microscope to the central region. Different colors correspond to different layers in the layout designing, which represent different dose or beam size during the electron exposure: for fine structures, a small beam is necessary.

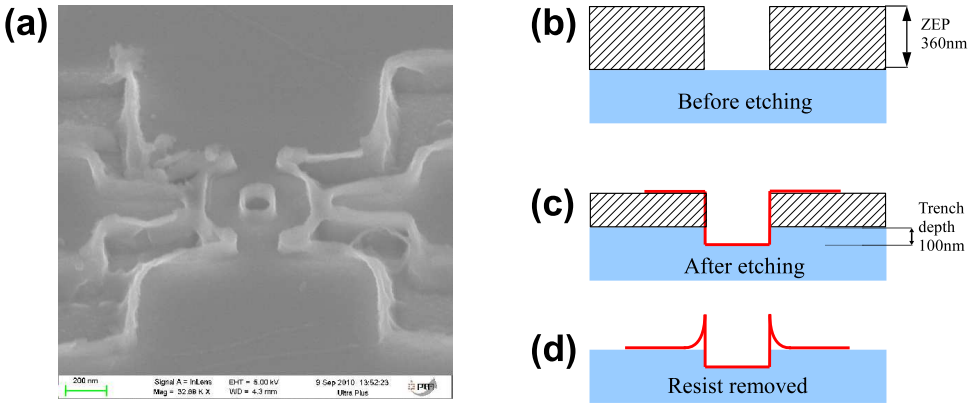

Figure 4.6: (a) SEM image of the re-deposition layer, in bright color. (b)-(d) Schematics of the formation of re-deposition layer, in red color. In the process of RIE, In-Cl compounds deposit on the sidewall of ZEP resist and etched trench. After the ZEP is removed by acetone, the re-deposited layer is left on the sample surface, or standing above the sidewall of trenches.

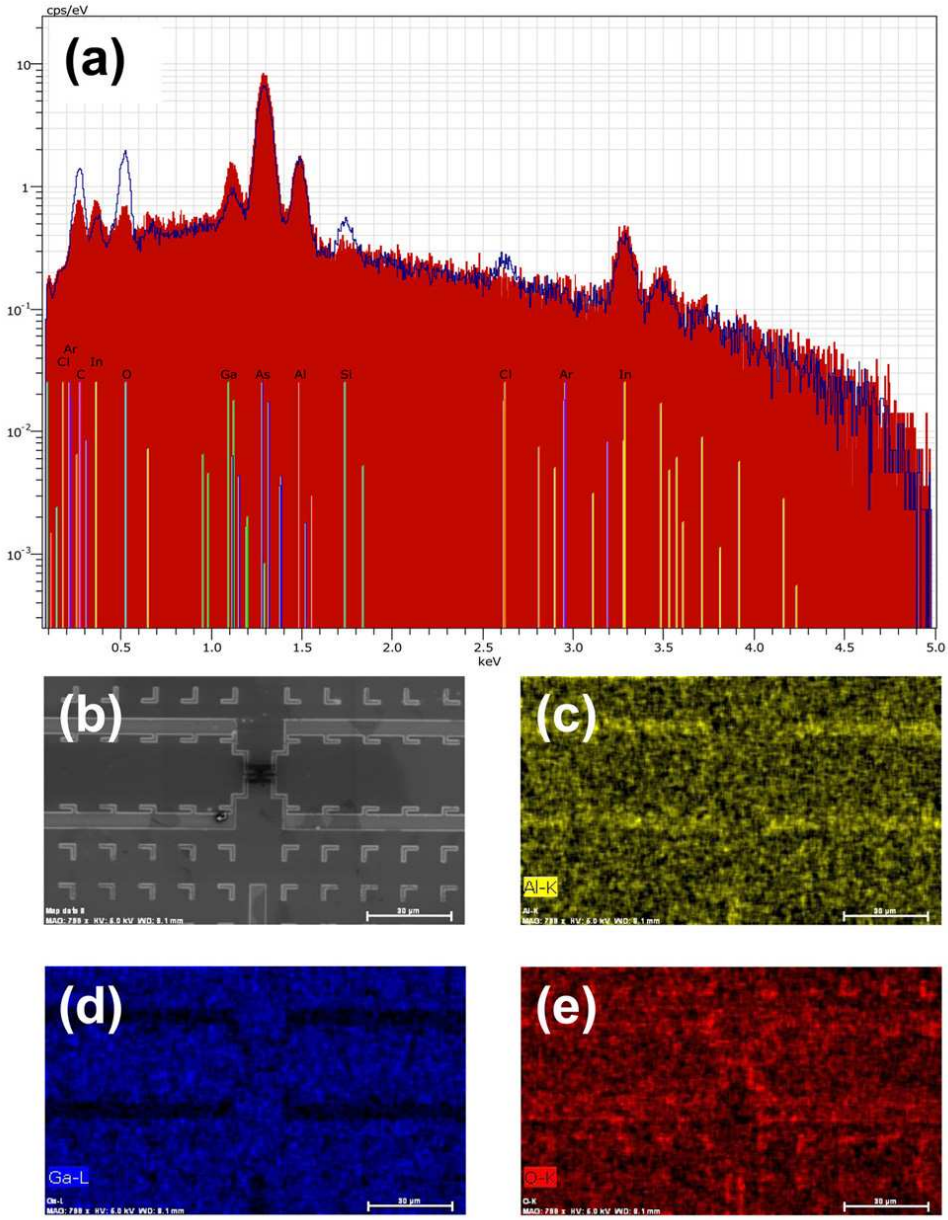

Figure 4.7: Results of the EDX analysis on the re-deposition layer. (a) The spectral analysis on the un-etched surface (red) and the nearby region of the etched trenches with re-deposition layers (blue). In the red spectrum, the peaks correspond to the elements of Ga, As, Al, In (from the capping layer), C, and O (from the vacuum chamber). In the blue curve, new peaks of Si and Cl appear (from $SiCl_4$ gas and Si dopants), the peak of Ga is lowered (capping layer and channel are etched) and the peaks of C and O become higher. (b) SEM image of the EDX mapping region. (c)-(e) The filtered EDX mapping results. (c) The Al-filtered map: the strong signal of Al is due to the etching that arrives in the InAlAs layer. (d) The Ga-filtered map. (e) The O-filtered map.

4.3 Device characterization

4.3.1 Testing operation

After bonding the device, the electrical properties are tested before mounting in the microscope. A standard multimeter is not suitable because the voltage applied when measuring the resistance can be so high (> 1V) that nano-devices are easily burnt. A precise low voltage source should be used. We used the "kOhms-meter" (developed in the laboratory) to test whether the metallic pads have ohmic contacts with 2DEG. The source delivers a low frequency AC voltage that polarizes a resistance bridge. The unbalanced current is amplified and detected with a lock-in chip. The 'bridge' part is depicted by the blue rectangle in Figure 4.8.

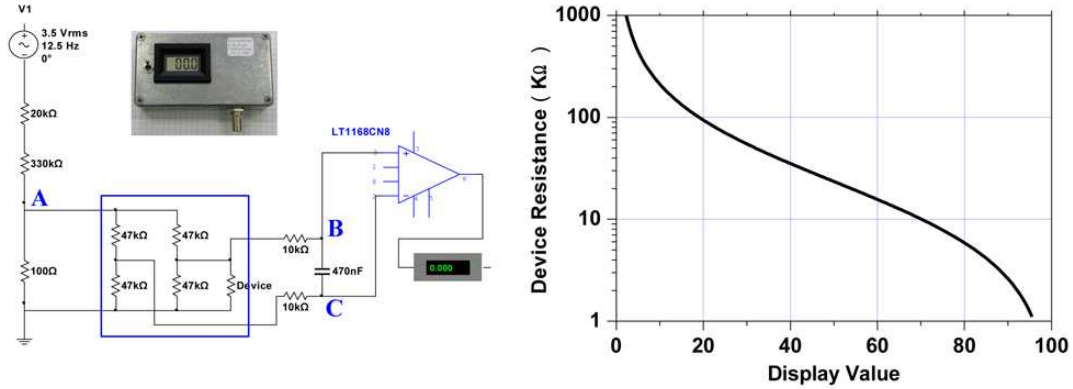

Figure 4.8: Working principle of the 'kOhms-meter'. (a) Circuit diagram. (b) Relation between the resistance of the tested device and the displayed value.

$V_A = 100\Omega \times \frac{3.5V}{330k\Omega+20k\Omega} = 1mV$; $V_B = 1mV \times \frac{R_1}{(R_1+47k\Omega}$, $R_1 = \frac{47k\Omega \times R}{(47k\Omega+R)}$, where R is the resistance of tested device; $V_C = \frac{1mV}{2}$. The measured voltage is thus given by:

$$V_C - V_B = \frac{0.5mV}{1 + 2R/47k\Omega} \tag{4.5}$$

The display indicates a value between 0 and 100 proportional to $V_C - V_B$:

$$V_{\text{display}} = \frac{100}{1 + 2R/47k\Omega} \tag{4.6}$$

$R = \infty \rightarrow V_{\text{display}} = 0$; $R = 23k\Omega \rightarrow V_{\text{display}} = 50$, and $R = 0 \rightarrow V_{\text{display}} = 100$. The relation between device resistance and displayed value is plotted in Figure 4.8.

4.3.2 Behavior during the cooling down

Figure 4.9 shows the recorded resistance change during a cooling down to 4.2 K. In opposition to bulk semiconductor materials with activated carriers, the resistivity of the 2DEG decreases as lowering the temperature. This behavior can be interpreted as the increase of the mobility μ_s as the temperature decreases ($\sigma = en_s\mu_s$), since the carrier density n_s of the 2DEG channel is almost constant. The mobility increase is due to the decreased phonon scattering at lower temperatures. The increasing resistance from 10 K to 4.2 K can be interpreted as the freeze-out of electrons in the parallel conducting layers which do not contribute any more to the conduction [61].

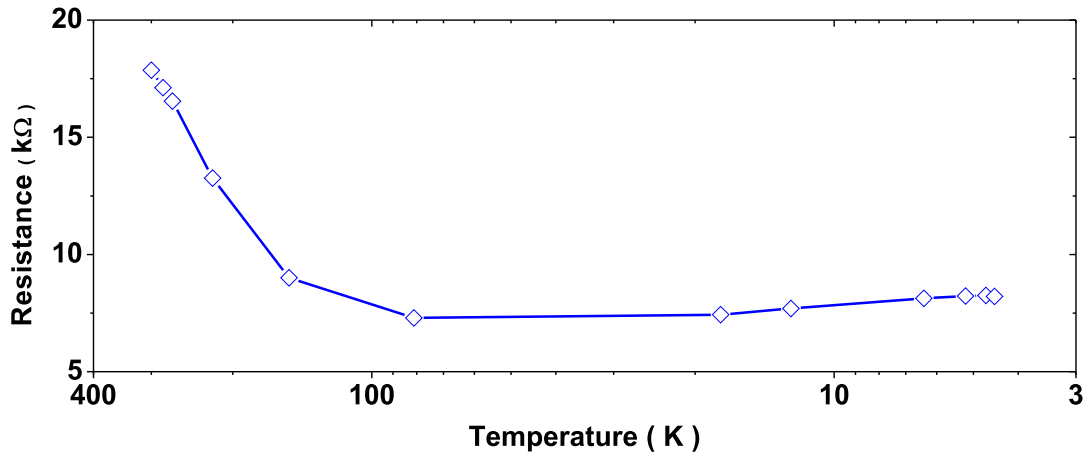

Figure 4.9: The device resistance change during cooling down. The test device is the Braess paradox device described in Section 5.2. The biased current is 10 nA, and the resistance is measured by 4-probe method.

4.3.3 Blocking and effect of device illumination.

Since the device and the measurement electronics are not isolated from the mains electricity, any fluctuations induced on the electricity lines are coupled to the measurement system, bringing spikes on the conductance signals that change the device properties. If a discharge is coupled to the device, it excites a lot of electrons, and the electrons might be trapped inside the crystal. At low temperature, the thermal energy of electrons is so low that they cannot escape from the traps. Sometimes these trapped electrons block the conduction channel of the

2DEG plane. This blocking phenomenon can also occur in the process of cooling down from 300 K to 4 K. We found that the electron transport properties are influenced by the cooling process [62].

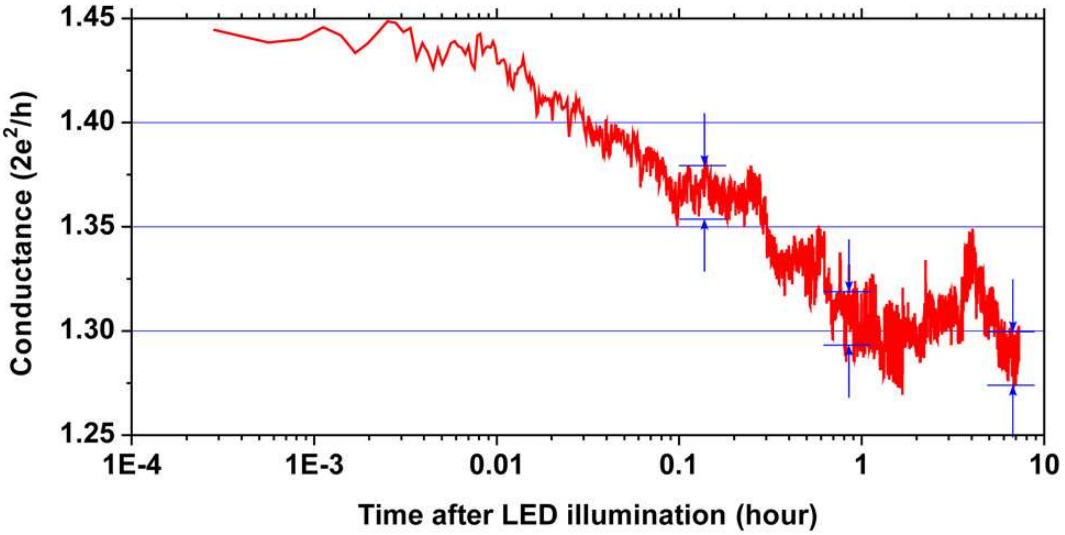

Figure 4.10: The stabilization of the device conductance after the illumination by an orange color LED. This curve is recorded on the device of the Braess paradox described in Section 5.2. The biased current is 10 nA, and the resistance is measured by 4-probe method.

In both cases the devices have to be reset. Here we use the method of sending photons with a light emitting diode (LED) in orange color. The working mechanisms of the reset include:

(i) Generation of electron-hole pairs in InGaAs because the photon energy E(eV) = 1240/λ(nm) of the orange LED with $\lambda \sim 600$ nm is higher than the band gap of the semiconductor (both InGaAs and InAlAs) (Δ_{InGaAs}=0.76 eV, Δ_{InAlAs}=1.48 eV).

(ii) Activation of electrons from the dopants that transfer to the channel.

(iii) Activation of deep donors which lie far below the Fermi energy. At low temperature, these deep levels are filled with electrons. After illumination, the photo-excited electrons are transferred from the deep levels to the channel [63].

As a result, most of the traps are erased, and the conductance returns to a normal value. The triangle-shaped potential well at the InGaAs/InAlAs interface also prevents the photo-generated electron-hole pairs to be re-combined, thus the electron density increases a bit, leading to persistent photoconductivity.

4.4 SGM Operation

4.4.1 Sample Alignment

To perform SGM experiments, the first step is to move the tip to the central part of nano-devices. In our samples, within the region of $500\,\mu\text{m} \times 500\,\mu\text{m}$ centered at the device, numerous marks (see Figure 4.5) are patterned as guides to find the device with the microscope. These marks are formed simultaneously as etching the materials to create the device, thus the depths of these marks are the same as isolating trenches. Figure 4.11 shows the 3-D images of the marks obtained with the microscope in topography mode.

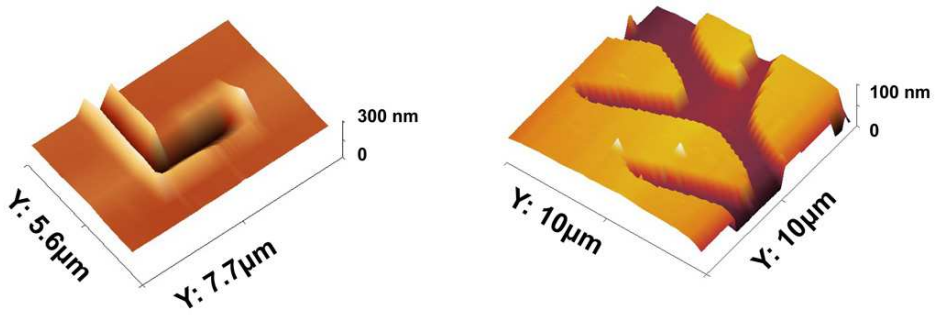

Figure 4.11: The marks patterned on the sample for the alignment of the microscope on the nano-device. Left, marks of samples prepared in Grenoble. Right, marks of samples prepared in Louvain. In the left figure, the re-deposition layers can be seen clearly. The height of the re-deposition layer is about 200 nm.

In the experiments performed during the first two years, we aligned the tip of the microscope on the nanostructure at RT, then retracted the tip, cooled down the microscope, and aligned the microscope again at LT. Later we found it's doable to move the tip within the central region of the sample ($100\,\mu\text{m} \times 100\,\mu\text{m}$) with optical microscope at RT. Alignment was only performed at LT, because the less scanning, the less of metallic layer deposited on the tip was damaged, which was more beneficial for the local gate effect.

Following the guiding marks, the tip is aligned to the device position after moving the sample by motors for several times. For SGM experiments, after the position of device is precisely aligned, we (1) use the 'follow me' function in 'Scan Control' module to move the tip on a flat region on the sample surface; (2) retract the tip with d_{ts}; (3) stop the feedback; (4) switch off the excitation signal. Then the voltage source is connected to the tip via one of the TF electrodes. The SGM image (map of conductance) is built while recording the tip position and the conductance of device at the same time.

4.4.2 Conductance map recording

The conductance of the device can be measured with different methods. Figure 4.12 shows the circuit diagram of the standard 4-probe lock-in method with current bias commonly used for low resistance devices.

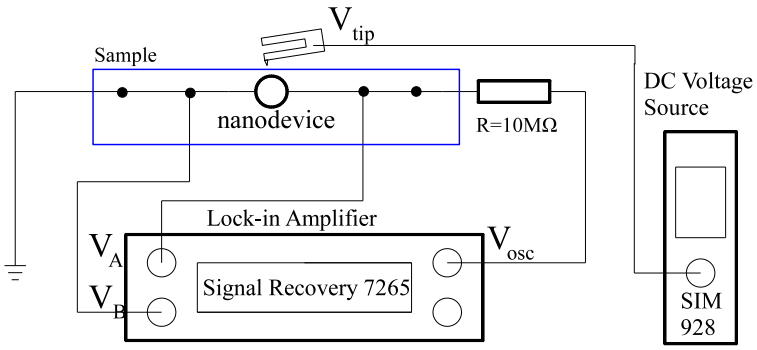

Figure 4.12: Schematic of the 4-probe measurement circuit. The current across the nano-device is $I \sim V_{osc}/R$, ($R \gg R_{device}$). The conductance is $G_{device} = I/(V_A - V_B)$. The tip gate voltage V_{tip} is applied with a DC voltage source grounded on the rack.

The lock-in oscillation voltage V_{osc} is a sinusoidal AC signal at the frequency f_{osc}. The lock-in demodulates the differential input voltage $(V_A - V_B)$ at the same frequency. This technique has the advantage of high signal-to-noise ratio, thus is widely used in small signal measurements. The analog output of the lock-in is recorded by the Nanonis input channel. The raw data recorded in SGM measurement is $V_{SGM} = (V_A - V_B) \times 10V/S$, where S is the voltage sensitivity of the lock-in. This signal is therefore proportional to the device resistance R_{device}, which can be converted later into device conductance G_{device}.

The oscillation frequency f_{osc} limits the scanning speed of SGM measurements. Generally, the time constant of the lock-in t_c is set larger than $3/f_{\mathrm{osc}}$ so that the integration time of the lock-in is long enough to filter the noise. In principle, the dwelling time of the tip on each point along the scanning path should be equal to t_c, and the time per line should be $\mathrm{P} \cdot \mathrm{t_c}$ where P is the number of points on the line (P=256 most of the time.). This results in slow scanning speed, typically in the order of 15 seconds per line. The maximum value of f_{osc} is limited by the device resistance and the capacitance of the microscope wirings.

4.5 Tip-Sample interaction

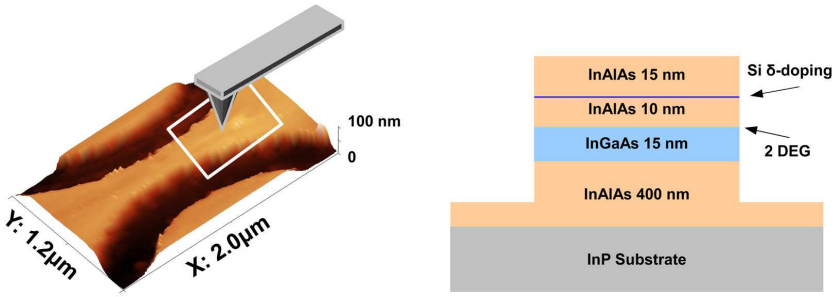

Figure 4.13: Left, the 3-D topography image of the constriction device obtained at 4.2 K. The rectangle in white color indicates the region where the SGM image shown in Figure 4.15 is obtained. Right, the epitaxial layers sequence of the heterostructures of the constriction device.

Before describing SGM experiments, it is useful to characterize the capacitive coupling between the metallic tip and the 2DEG. The capacitance can be tested via the electrostatic force by recording the frequency shift of the TF as a function of the tip voltage at a fixed distance $\mathrm{d_{ts}}$ above a large flat sample region when all the contacts on the sample are grounded. The gate effect can also be tested by recording the conductance changes of a constriction device versus tip voltage, when the tip is placed at the center of the constriction, as schematically shown in Figure 4.13. This device was fabricated from the high mobility 2DEG described in Section 4.1.1. The layers sequence is shown on the right hand side. The carriers density and mobility are $\mathrm{n_s} = 2 \times 10^{12}$ cm^{-2} and $\mu = 100,000 \mathrm{cm}^2/\mathrm{Vs}$, measured at 4.2 K.

4.5.1 Capacitive Force

The frequency shift of the TF as a function of V_{tip} is shown in Figure 4.14 (a). It can be well fitted with Equation 3.26. The fitting parabola has the expression:

$$\Delta f(\text{mHz}) = -0.558 \times (U_{ts}(\text{V}) - 0.19)^2 + 28.6$$

Here we can extract the contact potential between the tip and the InAlAs surface is about 0.19 V. The work function of Pt/Ir (on the tip) is in the range of 5.0∼5.9 eV. The work function of un-doped InAlAs can be estimated by $\chi + E_g/2 = 4.1 + 0.73 = 4.83$ eV, where χ is the electron affinity of InAlAs. However, for a semiconductor surface, the work function is strongly affected by the surface condition. The presence of tiny contamination or the occurrence of surface reactions might change the work function. The measured value of the contact potential is therefore consistent with these data. However, to describe quantitatively the interaction between the metallic tip and the buried 2DEG, the thickness of the dielectric layer (InAlAs in our case) and the shape of the tip apex have to be taken into account.

For simplicity, we first use the parallel-plate capacitor model for the situation of a large tip apex radius as illustrated in Figure 4.14 (b). The capacitance between the tip and the 2DEG can be calculated as:

$$C_{\text{total}} = \frac{\varepsilon_0 S}{x/\varepsilon_1 + d/\varepsilon_2} \tag{4.7}$$

where $\varepsilon_0, \varepsilon_1, \varepsilon_2$ are the dielectric constant of vacuum, relative dielectric constant of the medium between tip and surface (air or low-pressure He) and of the semiconductor material respectively, x is the distance from the tip to the surface, d is the distance from the surface to the 2DEG layer, S is the area of the tip apex plate. Inserting Equation 4.7 to 3.26, we get the resonance frequency shift of the TF:

$$\Delta f = \eta \frac{\varepsilon_0 S/\varepsilon_1^2}{(x/\varepsilon_1 + d/\varepsilon_2)^3} (U_{ts} + \Delta\mu_{ts}/e)^2 \tag{4.8}$$

The curve shown in Figure 3.9 for a gold surface is the result of Equation 4.8 when $d = 0$.

In ref [64], Hudlet *et.al.* calculated the capacitive force between a spherical AFM tip and a metallic surface:

$$F = \pi\varepsilon_1\varepsilon_0 \left[\frac{r^2}{x(x+r)}\right] (U_{ts} + \Delta\mu_{ts}/e)^2 \tag{4.9}$$

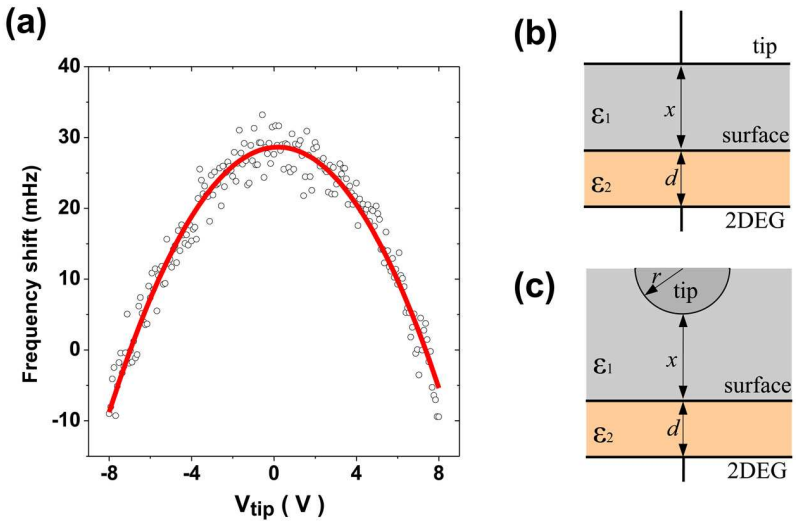

Figure 4.14: (a) Measurement of the frequency shift of the TF as a function of the voltage difference between the tip and the grounded 2DEG. The tip is placed above a large flat area with a tip-sample distance $d_{ts} = 30$ nm. (b) and (c), Schematics of the parallel-plane capacitor model and the sphere-plane capacitor model.

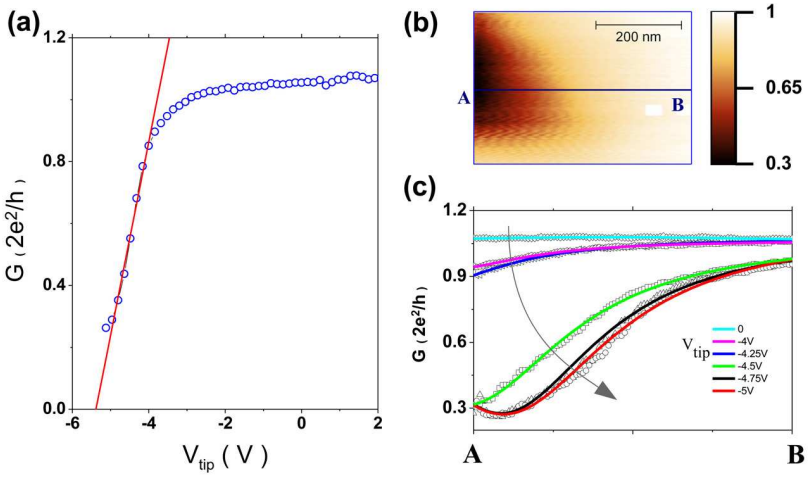

Figure 4.15: (a) Device conductance change as a function of the tip voltage. The tip is placed above the center of the constriction with a tip-sample distance $d_{ts} = 30$ nm. (b) SGM image obtained with $V_{tip} = -4.5$V, $d_{ts} = 30$ nm. Unit of color bar: $G_0 = 2e^2/h$. (c) Conductance profiles along line AB for different V_{tip}, extracted from the SGM images. Solid lines: fitting results with Lorentzian functions.

where r is the radius of a sphere-shaped tip apex as illustrated in Figure 4.14 (c). To include the effect of the insulating semiconductor layer, we assume that the effective distance x/ε_1 can be replaced by $x/\varepsilon_1 + d/\varepsilon_2$ as suggested by the expression 4.7.

Inserting the new form of F into Equation 3.22, we get:

$$\Delta f = \eta \frac{\pi\varepsilon_0 r^2(2x/\varepsilon_1 + 2d/\varepsilon_2 + r/\varepsilon_1)/\varepsilon_1^2}{(x/\varepsilon_1 + d/\varepsilon_2)^2(x/\varepsilon_1 + d/\varepsilon_2 + r/\varepsilon_1)^2}(U_{\mathrm{ts}} + \Delta\mu_{\mathrm{ts}}/e)^2 \tag{4.10}$$

Using this formula, the prefactor in the fitting parabola ($-0.558\mathrm{mHz/V^2}$) gives a radius of curvature of the tip apex about 13 nm for $\mathrm{d_{ts}} = 30$ nm.

In the discussion above, the 2DEG is supposed to be a perfect metal. However, the low carrier density implies an imperfect screening of the tip induced potential. This effect can be neglected in the analysis of the electrostatic force, but is central for the analysis for the gate effect, since a perfect screening would cancel the potential change.

4.5.2 Local Gate Effect

When the tip is just above the constriction, the tip-sample system can be regarded as a transistor with the tip acting as a gate. The $\mathrm{V_{tip}}$ induced conductance change can be analyzed with the transistor theory, in particular with high electron mobility transistor (HEMT) models involving a threshold gate voltage $\mathrm{V_{th}}$. When $\mathrm{V_{GS}} < \mathrm{V_{th}}$, the device is off. When $\mathrm{V_{GS}} > \mathrm{V_{th}}$, the transistor is turned on, and a channel has been created which allows current to flow between the drain and the source. In the regime $\mathrm{V_{DS}} < \mathrm{V_{GS}} - \mathrm{V_{th}}$, the transistor operates like a resistor, controlled by the gate voltage relative to the source. The current from drain to source is modeled as:

$$I_{DS} = \mu\frac{W}{L}C\left[(V_{GS} - V_{th})V_{DS} - \frac{V_{DS}^2}{2}\right] \tag{4.11}$$

where μ is the mobility of carriers, W is the gate width, L is the gate length and C is the gate capacitance per unit area. In our case, because $\mathrm{V_{DS}} \sim \mu\mathrm{V}$ and $\mathrm{V_{GS}} - \mathrm{V_{th}} \sim \mathrm{V}$, equation 4.11 can be re-written as:

$$G = \frac{I_{DS}}{V_{DS}} = \mu\frac{W}{L}C(V_{GS} - V_{th}) \tag{4.12}$$

This indicates that the conductance in linear regime is proportional to $(\mathrm{V_{GS}}-\mathrm{V_{th}})$. This linear dependence is visible in Figure 4.15 (a), with $\mathrm{V_{th}} = -5.5$ V.

Figure 4.15 (b) shows a SGM image recorded by scanning the tip above half of the constriction as depicted in Figure 4.13 (white rectangle) with d_{ts} = 30 nm and V_{tip} = −4.5 V. Extracted conductance profiles on the central line of the SGM images at different tip voltages are plotted in (c). Note that, the maximum of the conductance change (center of the constriction) is outside this scanning range. These curves can be fitted with Lorentzian functions. The fittings yield the same FWHM (full width at half maximum) value $w = 350 \pm 50$ nm. From Equation 4.12, we know that the spatial distribution of the conductance change reflects the shape of the gate induced potential, through the tip-channel capacitance $C(x)$:

$$C(x) = C_0 \frac{w^2}{4(x - x_c)^2 + w^2} \tag{4.13}$$

where x_c denotes the coordinate of the constriction center, and w is related to the vertical tip-sample distance and the tip apex radius. Thus, the conductance along the central path in horizontal direction is:

$$G(V_{tip}, x) = \mu \frac{W}{L} C_0 \left[\frac{w^2}{4(x - x_c)^2 + w^2} \right] (V_{tip} - V_{th}) \tag{4.14}$$

where V_{th} depends on the tip position x.

4.5.3 Finite screening length

For a better description of the tip induced potential inside the 2DEG, we analyzed the influence of the screening length. In ref [65], the authors studied the electrostatic screening by free surface carriers on a semiconductor when a charge q is placed above the surface. This model might be used to describe our system, although the 2DEG resides 25 nm below the surface, with the biased tip taking the role of the charge q. They found that the magnitude of electrostatic screening is determined by the factor k_{s0}/ε_r, where $k_{s0} \equiv \frac{e^2}{\varepsilon_0}\frac{\partial N_s}{\partial E} = \frac{e^2}{\varepsilon_0}\frac{m^*}{\pi\hbar^2} = 3\text{nm}^{-1}$. If the value of k_{s0}/ε_r is small (e.g., low density of carriers in the 2DEG), the conducting film can be neglected. On the other hand, if k_{s0}/ε_r is large, the potential perturbation in the 2DEG is small (screened).

According to ref [65], The potential $V(r)$ in the 2DEG plane for $z_0 > \lambda_F$ is given by an integral with two parameters: the mean dielectric constant ϵ_r around the 2DEG and the bare screening wave vector k_{s0} in the 2DEG:

$$\epsilon_r = \frac{\epsilon_{r1} + \epsilon_{r2}}{2} \tag{4.15}$$

$$k_{s0} = \frac{e^2}{\epsilon_0}\frac{\partial N}{\partial E} = \frac{e^2}{\epsilon_0}\frac{m^*}{\pi\hbar^2} \tag{4.16}$$

$$V(r) = \frac{Q}{4\pi\epsilon_0}\int_0^\infty J_0(q\,r)\,e^{-q\,z_0}\,\frac{2\,q}{2\,\epsilon_r\,q + k_{s0}}\,dq \tag{4.17}$$

where $J_0(qr)$ is the zeroth-order Bessel function. This integral can be approximated by a combination of the asymptotic behavior at large r and the value at $r = 0$ which requires the calculation of an integral $I(a)$ of the parameter a.

$$a = \frac{k_{s0}\,z_0}{2\,\epsilon_r} \tag{4.18}$$

$$I(a) = \int_0^\infty \frac{x\,e^{-x}}{x + a}\,dx \tag{4.19}$$

$$V(r) = \frac{Q}{4\pi\epsilon_0\,\epsilon_r\,z_0}\,\frac{I(a)}{1 + a\,I(a)\left((1 + r^2/z_0^2)^{3/2} - 1\right)} \tag{4.20}$$

Figure 4.16 shows both the potentials calculated from Equation 4.20 and a Lorentzian function. Within the FWHM these two curves are almost identical while for a larger distance from the tip, the potential given by Equation 4.20 decreases faster. Thus, we know that Lorentzian function is a good approximation to describe the tip induced potential.

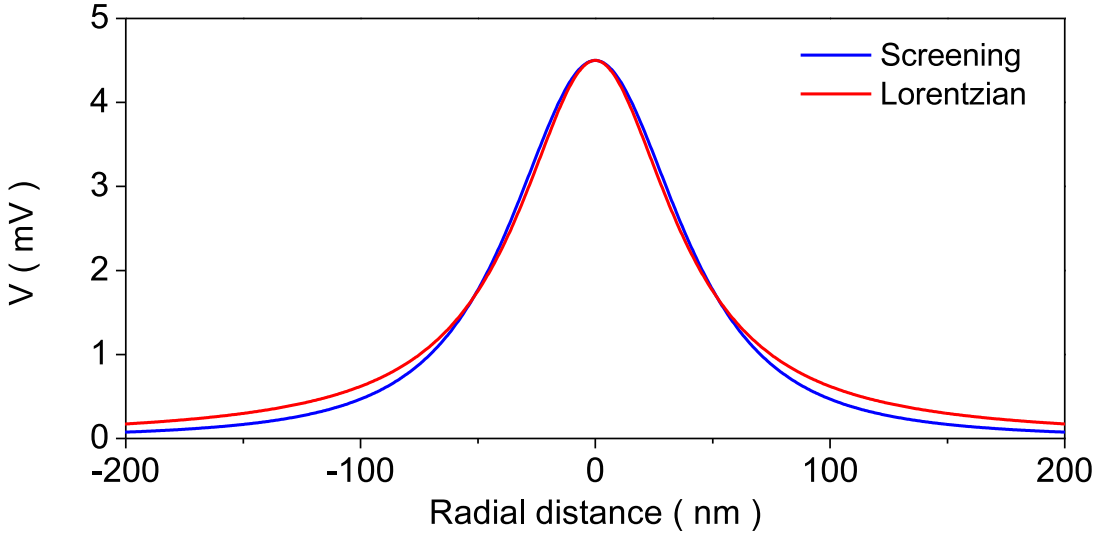

Figure 4.16: Blue: Potential $V(r)$ for $\epsilon_{r1} = 1$, $\epsilon_{r2} = 14$, $k_{s0} = 3\,\mathrm{nm}^{-1}$, $z_0 = 50\,\mathrm{nm}$, $Q/4\pi\epsilon_0 = V_{\mathrm{tip}}\,R_{\mathrm{tip}} = 1\,\mathrm{V}\times 20\,\mathrm{nm}$. The curve calculated from Equation 4.20. Red: Potential distribution calculated from a Lorentzian function with FWHM 80 nm.

4.6 SGM test experiment on an elliptic cavity

In the 1990's, the scientists in IBM developed a method for confining electrons to artificial structures at the nanometer scale. They successfully demonstrated that the surface state electrons on Cu(111) were confined in closed structures (corrals) defined by barriers built from Fe adatoms. The barriers were assembled by individually positioning Fe adatoms using the tip of a low temperature STM [66, 67]. Similarly, in a nano-device made by etching from a 2DEG sample, the vacuum gap in the region where the semiconductor material is removed by etching can be regarded as a corral (barrier) for the electrons flowing in the 2DEG plane. Among the different possible cavity shapes, we chose to consider the elliptic shape because of its focusing property: a light or acoustic wave leaving one focus will pass through the other one after reflection on the ellipse.

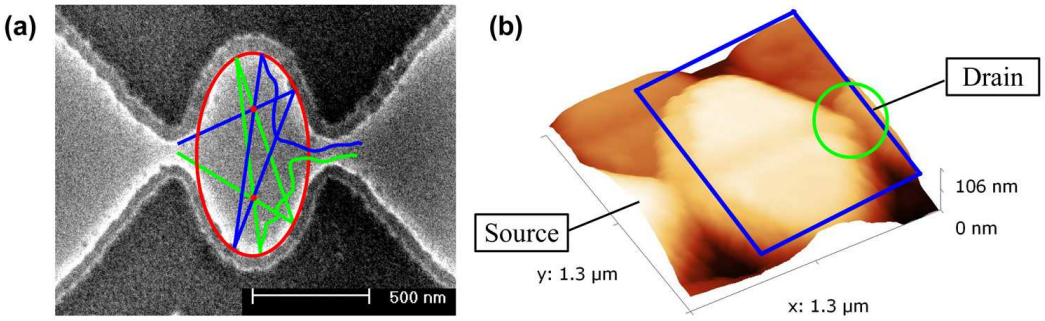

Figure 4.17: (a) The SEM image of the ellipse device. The blue and green lines schematize the trajectories of electrons. (b) The topography image of the ellipse device obtained at 4.2 K. The green circle indicates a damage on the sample surface, exactly at the right constriction.

In Figure 4.17, (a) shows the SEM image of the 'elliptic corral' device made from the 2DEG heterostructure presented in Section 4.5. From the well known optical properties of ellipses, one can speculate that the electrons emitted from the left constriction will pass one of the two focuses of the elliptic corral (red spots), and after the reflection by the 'corral', will pass the other one, as schematically shown by the green and blue lines. The elastic mean free path of the electron in this sample is calculated as $l_e = 2.3\mu$m. The size of the device L is designed ($L < l_e$) such as to allow the electrons to elastically reflect on the 'corral' for a few times before leaving the ellipse. The SGM measurement is proposed as follow: when a negatively biased tip scans above the device, if the tip is right

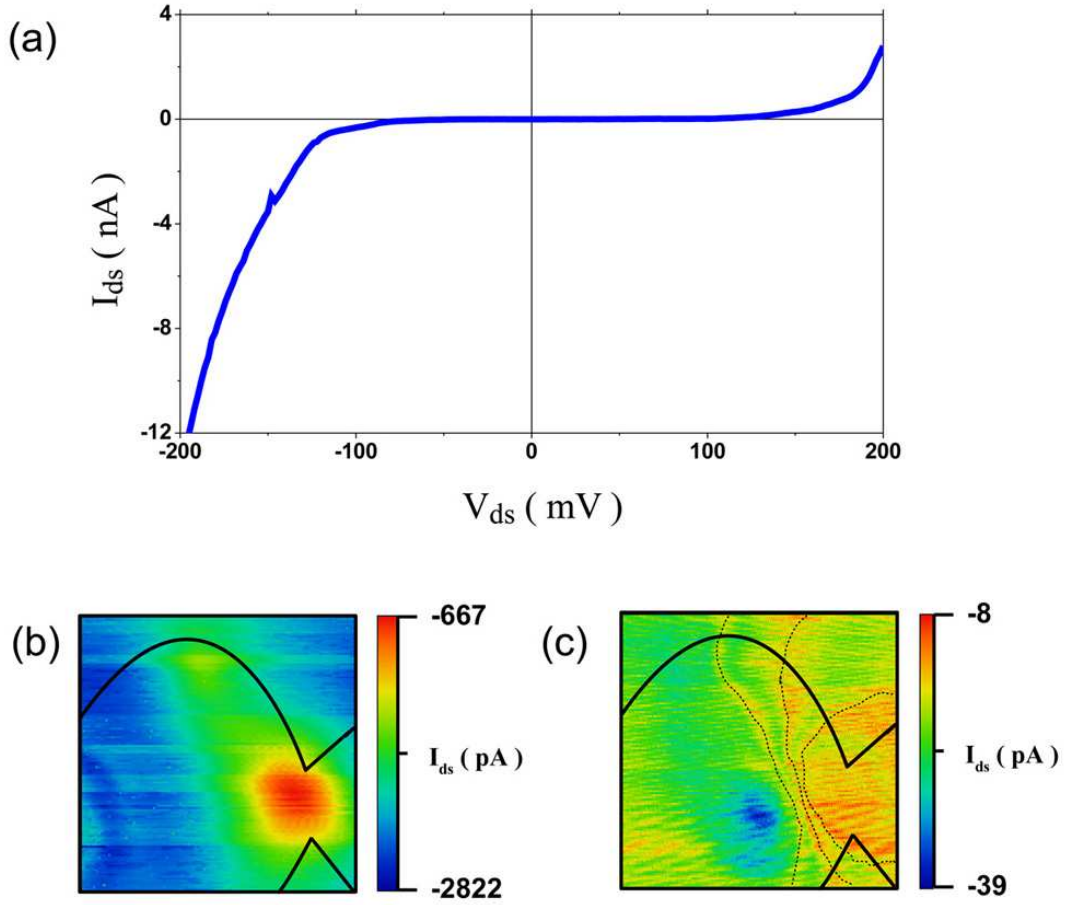

Figure 4.18: (a) I-V characteristics of the ellipse device. The curve is measured with the 2-probe method: the drain electrode is biased with a DC voltage V_{ds}^{DC}, and the source electrode is grounded via a current amplifier with a gain of 10^7V/A. (b) and (c) Maps of the device current obtained with $V_{ds}^{DC} = -150$ mV, $V_{tip} = -1$V (b), and $V_{ds}^{DC} = -50$ mV, $V_{tip} = 1$V (c). The scanning area is $1\mu m \times 1\mu m$, denoted by the blue square in Figure 4.17 (b). The black lines denote the ellipse and one constriction. The tip sample distance is $d_{ts} = 30$ nm.

above one of the two focuses, the conductance would be strongly affected because the tip induced potential blocks the paths of many electrons. The conductance will increase or decrease depending on the connections to leads: the tip can help electrons to escape the cavity or on the opposite reflect them back to the entrance.

In the experiment, this effect could however not be studied because of a large potential barrier at the opening. Figure 4.18 (a) shows the I-V characteristics of the device when the tip is far. In the V_{ds}^{DC} range [−80 mV, 120 mV], the current is indeed very low (less than 100 pA), showing that the Fermi energy is lower than the potential barrier, which is larger than 100 meV. When V_{ds}^{DC} is small, the electron tunneling dominates; when V_{ds}^{DC} increases, the electrons can be transmitted above the barrier and the current increases dramatically. From the topography image of the device shown in Figure 4.17 (b), we find a shallow trench located on the surface of the right side constriction, as denoted by a green circle. We suspect that the depletion induced by this trench might be the origin of the potential barrier.

In the SGM measurements, we find that a negative tip voltage $V_{tip} = -1V$ induces a large current drop at the right constriction ($|I_{ds}| = 2822$ pA $\rightarrow$ 667 pA at $V_{ds}^{DC} = -150$ mV), as shown in Figure 4.18 (b). The drop might be due to an increase of the potential barrier discussed above. The SGM images therefore reveal the location of the barrier and confirm the above interpretation, based on the topography image, with a barrier located at the right constriction.

We also find that a positive tip voltage $V_{tip} = 1V$ induces a large current increase when the tip is inside the ellipse ($|I_{ds}| = 8$pA $\rightarrow$ 39 pA at $V_{ds}^{DC} = -50$ mV), as shown in Figure 4.18 (c). We also observe current oscillations making a set of lines (black dotted lines) around the region of the right constriction. This suggests that the current is blocked by negative charges in a trap located somewhere in the heterostructure, with a number of charges changing one by one when the tip moves, due to a Coulomb blockade effect in the trap. When the tip is just above the trap, the positive V_{tip} compensates the effect of the charges, explaining the large current increase. Similar effects will be described in detail in Section 5.3.

This experiment was not continued because of the presence of the strong barrier at the opening.

Chapter 5

SGM Experiments

Contents

5.1 Coulomb blockade in a quantum dot

With the advances in materials synthesis and processing techniques, people developed various nano-devices. One of these devices that attracted a lot of interests is the quantum dot (QD). In a QD, electrons are confined in a spatial region with typical length scales less than 100 nm [68]. There are several different ways to produce QDs, including epitaxial growth on crystals [69], chemical synthesis in solutions [70], direct fabrication by lithographic methods [71], or gate-defined on 2DEG materials [43, 72], nanotubes [19] and nanowires [18]. At such scales, quantum mechanics has to be used to interpret the phenomena [41, 73], that makes QDs ideal environment to test fundamental physics, e.g., single electron transport already discussed in Section 2.2.2 or energy level spectrum in these 'artificial atoms'.

In the following, we discuss QD on InGaAs/InAlAs heterostructure. Different from defining QDs by applying a negative voltage on metallic gates deposited on the sample surface, we patterned the QD by etching method (see Section 4.2 for details of the process done in Grenoble). The electronic states of QD are controlled by tuning the voltages of two lateral gates made in the 2DEG layer. Figure 5.1 shows both the layers sequence of the heterostructure and the SEM images of the QD device.

This type of QD device with lateral gates was designed for our SGM study because with metallic surface gates, (i) the tip would be difficult to scan with small distance due to the height of metallic gates, (ii) the phenomena at the vicinity of the two tunneling barriers would be difficult to explore due to the strong screening of tip potential by the metallic gates, and (iii) touching the metallic gates with the tip at large voltage differences (of the order of a few volts) would damage the tip and/or gates.

5.1.1 Transport measurements

Hall and Shubnikov-de Haas measurements on a Hall bar yield the carriers density and mobility as $n_s = 1.6 \times 10^{12}$ cm^{-2}, $\mu = 78,000\,\mathrm{cm}^2/\mathrm{Vs}$, as shown in Figure 2.3. To perform electrical measurements on QDs, the current-biased 4-probe method does not work because the premise of constant current for current-biased measurement is not correct when the QD is in the high resistance state. Instead, we use a voltage bias configuration, as shown in Figure 5.2. The thermal energy of electrons at 4.2 K is $k_B T = 362\,\mu$eV, which is the upper limit of device bias to

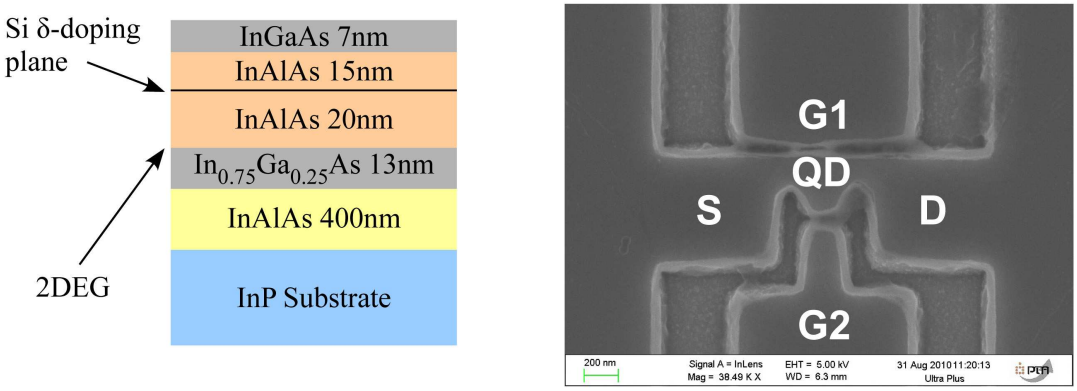

Figure 5.1: Left, the epitaxial layers sequence of the InGaAs/InAlAs heterostructure grown on the InP substrate. The 2DEG plane is buried 42 nm below the surface. Right, the SEM image of the QD device.

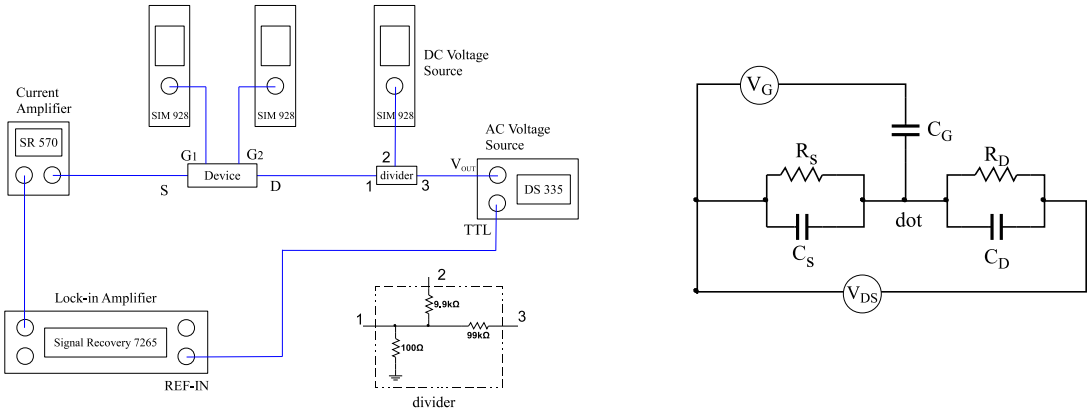

Figure 5.2: Left, the measurement circuit diagram of the voltage-biased configuration. The $V_{DS}^{AC} = 100\ \mu V$ is generated by dividing the $V_{OUT} = 100$ mV from the AC voltage source (output minimum 50 mV) by 1000. The $V_{DS}^{DC} = -3$ mV $\rightarrow +3$ mV is generated by dividing the output of DC voltage source (output minimum 1 mV) by 100. The current through the device is amplified with a gain of 10^6 V/A. The output of the current amplifier is then demodulated by the lock-in amplifier at the same frequency as V_{DS}^{AC}. The voltage on the two gates V_{G1} and V_{G2} are applied by the isolated voltage sources. Right, the equivalent circuit of the QD device. For simplicity, only one of the two gates is depicted here.

ensure the device to work in the linear regime. In Figure 5.3, (a) and (b) show the linear conductance $G = I_{DS}^{AC}/V_{DS}^{AC}$ as functions of two lateral gates voltages V_{G1} and V_{G2} when the device is biased at $V_{DS}^{AC} = 100\ \mu V$; (c) shows the charge stability diagram measured by sweeping the gate voltage V_{G1}, and the bias voltage V_{DS}^{DC} in the range $[-3\ mV, +3\ mV]$.

Discussion

1. In Figure 5.3 (a), when V_{G1} decreases from -0.4 V to -0.75 V, the conductance is a superposition of a monotonically decreasing signal and a set of peaks that appear at some specific V_{G1}. The monotonic decrease is similar to the behavior of a normal transistor, and can be interpreted as the reduction of electrons density inside the QD and the narrowing of the two constrictions between QD and drain/source, both due to the depletion by the negatively biased gate electrode.

   The appearance of peaks in a weakly coupled dot can be explained by the Coulomb blockade effect, with a charging energy larger than temperature and bias voltage. As V_{G1} raises, the increasing coupling to the reservoirs (source and drain) results in broadened, overlapping peaks with minima that do not go to zero [41, 74, 75].

   When V_{G1} is smaller than -0.775 V, the QD is fully blocked, as can be seen in the inset showing the last visible Coulomb peak. This is due to the closure of the two constrictions.

   Below -0.7 V, the QD device can be described by the Coulomb blockade model depicted in Figure 2.7. As V_{G1} is continuously decreased, the electrochemical potential (μ_N) of electrons inside the QD increases and when it gets aligned between μ_S and μ_D, the number of electrons inside the dot is fluctuating between (N) and (N-1), which results in a current peak as observed at $V_{G1} = -0.773$ V, -0.743 V, -0.729 V, -0.707 V. The capacitance deduced from this series of peaks spaced by $\Delta V_{G1} \approx 20$mV is $C_{G1} = e/\Delta V_{G1} = 8$ aF.

2. By sweeping V_{G2}, a similar behavior of the conductance is observed, as shown in Figure 5.3 (b). The difference is the spacing between peaks which is much larger than that obtained with V_{G1}. This feature can be interpreted as the size of G_2 is smaller, thus the capacitance C_{G2} is smaller than C_{G1}. As can be seen in Equation 2.22, the spacing of adjacent peaks is indeed inversely proportional to the gate capacitance. The spacing between peaks

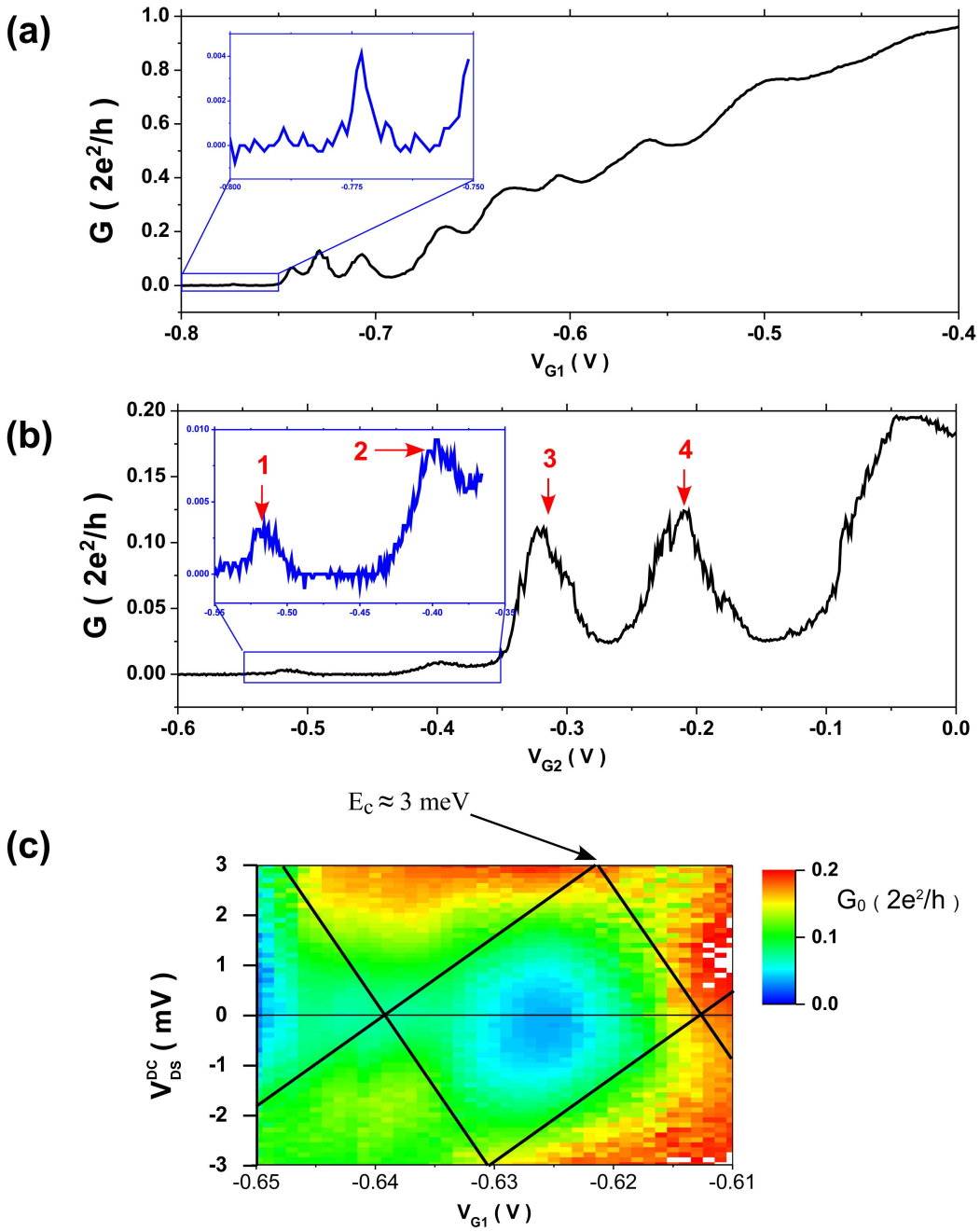

Figure 5.3: (a) The conductance of the QD as a function of V_{G1}, at $V_{G2} = 0$, $V_{DS}^{DC} = 0$. (b) The conductance of the QD as a function of V_{G2}, at $V_{G1} = -0.65$ V, $V_{DS}^{DC} = 0$. (c) The charge stability diagram measured by sweeping V_{G1} and V_{DS}^{DC}, at $V_{G2} = 0$.

1 and 2, or between 3 and 4, is $\Delta V_{G2} \approx 100$ mV. The capacitance is therefore $C_{G2} = e/\Delta V_{G2} = 1.6$ aF.

3. To determine the charging energy of QD, we need to sweep the DC source-drain voltage V_{DS}^{DC} and record the charge stability diagram as shown in Figure 5.3 (c). From the Coulomb diamond depicted by oblique lines, the charging energy of the QD is determined as $E_c \approx 3$ meV. The total capacitance is therefore $C_\Sigma = e^2/E_c \approx 85$ aF. The source/drain capacitances would be $C_s \approx C_d = (C_\Sigma - C_{G1} - C_{G2})/2 = 38$ aF. For a symmetric QC, the different slopes in the Coulomb diamond indicate a certain asymmetry.

In different measurements of G versus V_{G1} and V_{G2}, we found that the position of Coulomb peaks varied. This indicates that the charge states in our QD device are very sensitive to the sample history.

To observe clearly the discrete nature of charging via the Coulomb blockade effect, two conditions have to be met: (i) tunneling resistance $R_t \gg h/e^2 = 26$ kΩ, and (ii) charging energy $e^2/C_\Sigma \gg k_B T$. (i) could be improved by reducing the coupling of the QD to source/drain. (ii) could be improved by further reducing the temperature or the size of QD.

5.1.2 SGM measurements

The SGM measurement was performed with the procedure described in Section 4.4. Figure 5.4 (a) shows the topography of the QD recorded in AFM mode at 4.2 K. Due to the height of the walls from the re-deposition layer, the tip had to be scanned in a plane at a larger distance from the sample surface such as to preserve the tip, 130 nm in this case. Figure 5.4 (b) shows the conductance map of the QD obtained in SGM mode with $V_{tip} = -3.6$ V.

One can see that a large response of conductance on V_{tip} occurs at the central region of the QD. This result indicates that the conductance is dominated by the dot. The capacitance coupling between the tip and the QD decreases when the tip moves away from the QD. When the tip is placed right above the center of QD, or in a very small area around, the device is fully blocked (G=0, black color). This can be interpreted either as the two connections are converted into thicker tunneling barriers, or as the dot is depleted. One can see also concentric fringes around this blocked region.

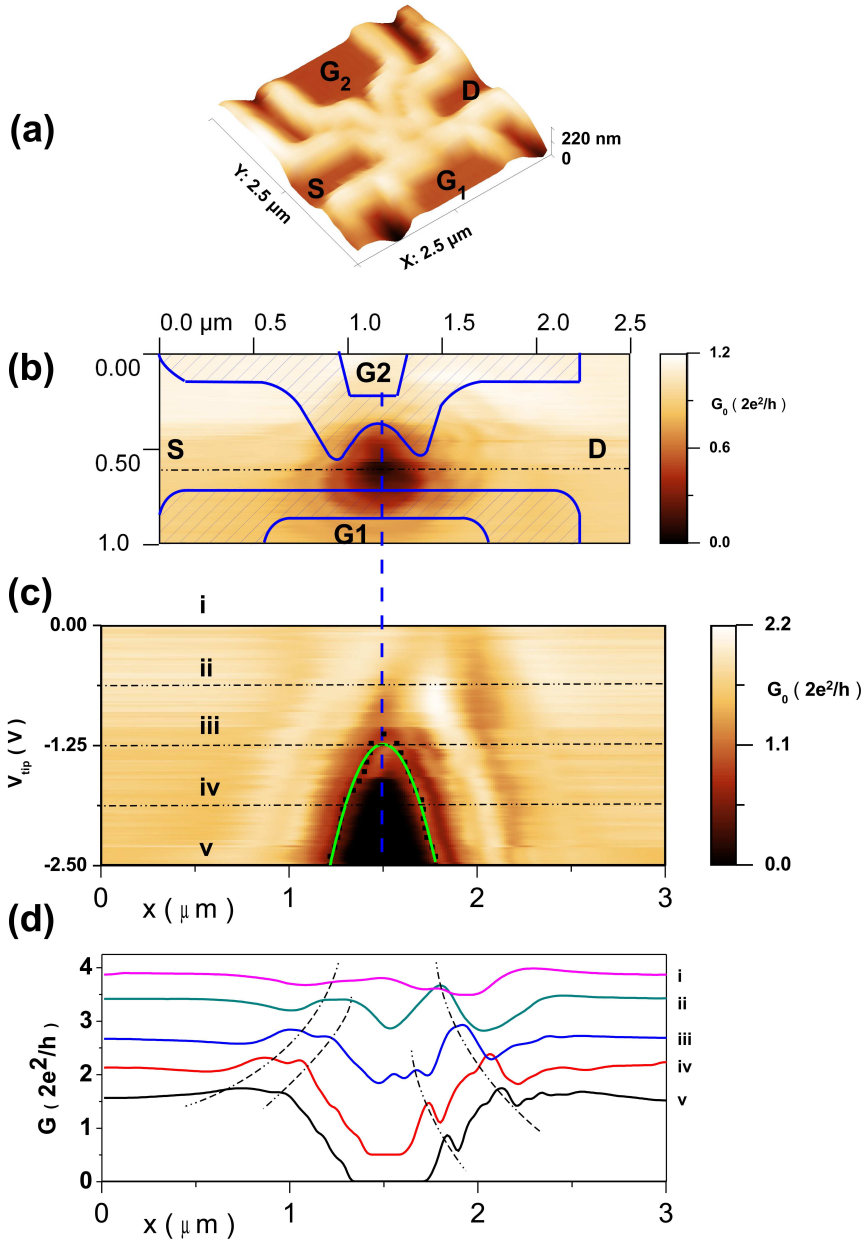

Figure 5.4: (a) Topography of the QD, obtained at 4.2 K. (b) Conductance map of the QD obtained by SGM with $V_{tip} = -3.6$ V. The hatching areas represent the etched trenches with a depth of about 100 nm. (c) V_{tip} resolved measurement obtained by scanning the dashed line depicted in (b) with V_{tip} changed from 0 to -2.5 V with a step of -20 mV. The black dots mark an iso-conductance line. The solid curve in green is the fitted result of the dots with a parabola function. In (b) and (c), $V_{DS}^{AC} = 100$ μV, $V_{DS}^{DC} = 0$, $V_{G1} = V_{G2} = -1.3$ V, $d_{ts} = 130$ nm. Between the measurements of (b) and (c), the background charge state around the QD changed due to a discharging. (d) Conductance profiles extracted from (c) at $V_{tip} = 0, -0.62$ V, -1.24 V, -1.88 V, -2.5 V. A shift of e^2/h is introduced between each curve.

Figure 5.4 (c) shows the V_{tip} dependence of the conductance, obtained by scanning the tip along the dashed line in (b) and changing V_{tip} from 0V to -2.5 V with a step of -20 mV. The experiment is performed with the following procedures[1]: (1) Record a topography image in AFM mode. (2) Lift the tip from the surface with $d_{ts} = 130$ nm, while stopping the feedback, and set the TF excitation to zero. (3) Apply a DC voltage (V_{tip}) to the tip and scan the biased tip along the dashed line depicted in (b), at a speed of 200 nm/s (15 s for 3 μm); (4) after one SGM image (a rectangle of 3 $\mu m \times 1$ nm, 256×1 pixels) is completed, V_{tip} is changed and the procedure is repeated at step (3). Loops of (3) and (4) are controlled by a LabView program, thus it is possible to leave the microscope working automatically. In the voltage resolved measurement shown in (c), we see that the patterns are asymmetric on different sides of the central line (blue dashed). This is an indication that the QD (or the tip) is not symmetric. The two constrictions are probably not identical.

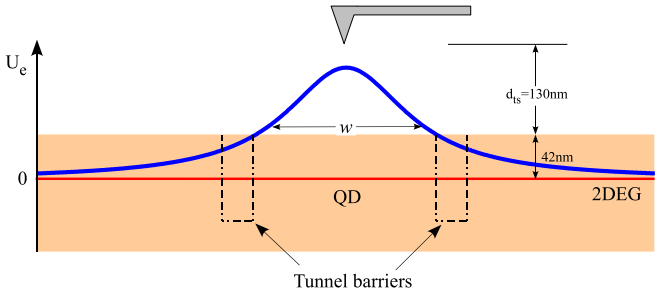

Figure 5.5: Schematic of the tip induced potential U_e in the 2DEG plane. In practice, the shape of U_e might be asymmetric, and/or the maximum of U_e might be shifted from the point beneath the tip apex.

In Figure 5.4 (d), comparing the conductance profiles extracted from (c) for 5 V_{tip} values, we can see as the tip moves away from the device in the right side direction, two conductance peaks are superimposed on the increasing conductance. This feature seems to have the same origin as the curve obtained by sweeping the lateral gate voltage shown in Figure 5.3. In the left side direction, similar phenomena are observed but the amplitude is much weaker. Since better Coulomb blockade (more symmetric QD barriers) is obtained when the negatively biased tip is above the right constriction, we conclude that the tunnel barrier of the right side is 'thinner' (or 'lower') than that of the left side, and becomes 'thicker' (or 'higher') in presence of the tip.

[1]This type of measurement method is referred as 'line spectroscopy' in the sections on Braess paradox and charge traps.

If we simply assume that the tip-induced potential distribution in the 2DEG channel is Lorentzian-shaped, the potential U_e experienced by the electrons inside the QD is:

$$U_e = \beta \cdot \frac{V_{\text{tip}}}{x^2 + (w/2)^2} \tag{5.1}$$

where x is the distance from QD to tip, w and β are functions of the tip-sample distance, the tip shape and the screening in the 2DEG.

Since the device conductance is a function of this potential: $G = f(U_e)$, an iso-conductance line means the same U_e, thus we get a relation $V_{\text{tip}}(x)$ at a constant U_e:

$$V_{\text{tip}}(x) = U_e \cdot \frac{x^2 + (w/2)^2}{\beta} \tag{5.2}$$

The innermost iso-conductance line is determined by following a resonant peak on each trace (marked with dots in (c)) and fitting these dot with Equation 5.2. The fitted result $V_{\text{tip}} = -7.93 \times [(x - 1.5)^2 + 0.39^2]$[1] indicates that the FWHM of tip induced potential is w=780 nm. This is a larger value than that obtained on the (simple) constriction in Section 4.5, because the tip height is larger here due to the re-deposition layer.

The tip capacitance

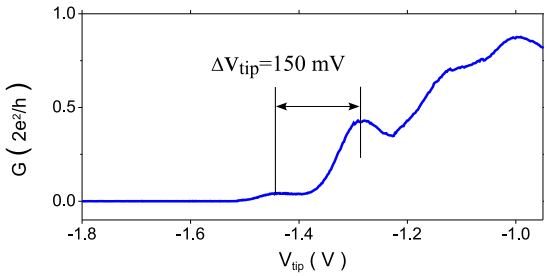

Figure 5.6: The conductance of the QD as a function of V_{tip}, at $V_{\text{DS}}^{\text{AC}} = 100\ \mu$V, $V_{\text{DS}}^{\text{DC}} = 0$, $V_{\text{G1}} = V_{\text{G2}} = -1.3$ V, $d_{\text{ts}} = 130$ nm. The tip is placed above the center of the QD.

The tip capacitance deduced from the conductance peaks shown in Figure 5.6 spaced by $\Delta V_{\text{tip}} = 150$ mV is $C_{\text{tip}} = e/\Delta V_{\text{tip}} = 1.1$ aF.

[1]The center of the QD locates at $x = 1.5\ \mu$m. Units of V_{tip} and x are V and μm

5.2 Braess paradox Device

5.2.1 Braess paradox in classical networks

The Braess paradox [76] states that adding an extra road capacity to a traffic network when the moving entities selfishly choose their route, can in some cases reduce the overall performance. This can be explained within the game theory language since it may occur that the equilibrium point of a many-person game, in which each player is aware of the supposed strategies followed by rivals, i.e., the Nash equilibrium [77], does not necessarily give an optimal payoff and may counter-intuitively lead to a poor compromise for all players.

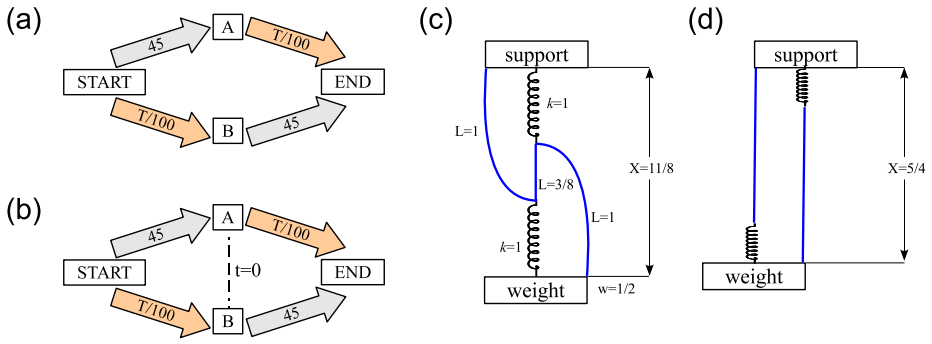

Figure 5.7: Schematics of Braess paradox: (a)-(b) in a traffic network; (c)-(d) in a mechanical network. The occurrence of Braess paradox is described in text.

Figure 5.7 (a) and (b) show the example of Braess paradox in traffic networks. Consider the road network of (a), for example, 4000 drivers wish to travel from point Start (S) to End (E). The travel time in minutes on the S-A (and B-E) road is a constant 45 minutes, and on S-B (and A-E) is the number of travelers (T) on this road divided by 100. The time needed to drive S-A-E route with A drivers would be (A/100+45), and the time needed to drive the S-B-E route with B would be (B/100+45). If either route is shorter, it would not be a Nash equilibrium as any rational driver would switch routes from the longer route to the shorter route. As there are 4000 drivers, the fact (A + B = 4000) can be used to solve that A = B = 2000 when the system is at equilibrium and therefore each route takes (2000/100+45=65) minutes. In (b), the dashed line means an additional road with a very small travel time of approximately 0 minutes. In this situation, all drivers will choose the S-B-A-E path, as S-B-A will take 40 minutes at its worst while simply driving S-A is always 45 minutes. Upon reaching B, every rational driver will select to take the 'free' road to A and continue to E, as B-E is

always 45 minutes while B-A-E is at worst 40 minutes. Each driver's travel time is (4000/100+4000/100=80) minutes, an increase from the 65 minutes required when the fast A-B road did not exist. No driver has an incentive to switch, as the two original routes (S-A-E and S-B-E) are both now 85 minutes. If every driver were to agree not to use the A-B path, every driver would benefit by reducing his travel time by 15 minutes. However, because any single driver will always benefit by taking the A-B path, the socially optimal distribution is not stable and so Braess paradox occurs [78]. In real transportation world, Braess paradox were found for example in the closure of 42$^{\text{nd}}$ street of New York city in 1990 [79], and remove of motorway in Cheonggyecheon of Seoul in 2003.

Figure 5.7 (c) and (d) schematically show the Braess paradox occurred in a mechanical network. The springs are identical having zero un-stretched length, spring constant k=1 N/m, and safety strings with length 1 m. The string that link the two springs has the length of $\frac{3}{8}$ m. The weight exerts a force of $\frac{1}{2}$ N. In (c), both the safety strings are limp, and the distance from support to weight is $X = \frac{11}{8}$ m. In (d), after the linking string is cut, the weight is higher at equilibrium, and the new distance is $X = \frac{5}{4}$ m. The Braess effect resides in the fact that cutting a link increases the height of the weight instead of the expected decrease [80].

5.2.2 Braess paradox in quantum device: Theory

Collaboration with Marco Pala, IMEP, Minatec, Grenoble[1]

In order to study the occurrence of the Braess paradox in a quantum system, we focus on mesoscopic samples with sizes of hundreds of nanometers, where many conducting channels contribute to the total current, but the physical length of the device remains smaller than the phase coherence length L_ϕ (several microns for high-mobility 2DEG samples at low temperatures). We deal with such structures motivated by the principle, which states that for a large number of quantum states, a classical behavior would be recovered by macroscopic quantities like the current. Another reason for focusing on large mesoscopic samples at low temperature is that the large number of transverse modes involved in the transport would allow us to distinguish the occurrence of the Braess paradox from a genuine resonant tunneling or from size effects which are important only when the structures are weakly coupled to the leads and a few transverse modes propagate through them.

[1]The numerical simulations are accomplished by M. Pala and S. Baltazar.

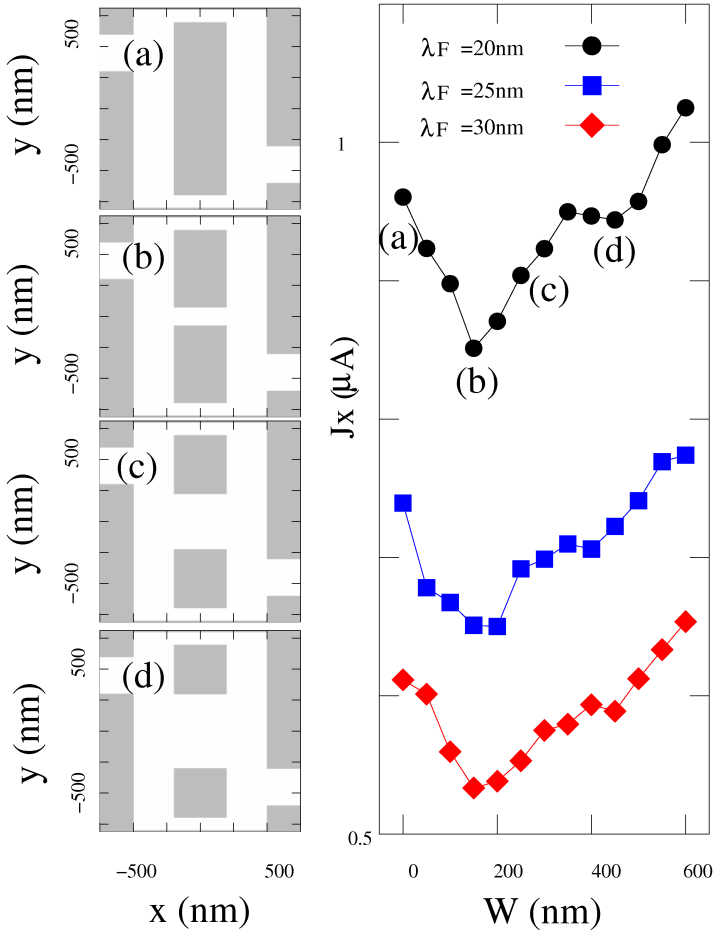

Figure 5.8: Left: sketch of the device configurations with a central wire width of 0, 150, 300 and 450 nm. Right: net current through the device as a function of the width of the central wire W for $\lambda_F \approx 20$, 25 and 30 nm.

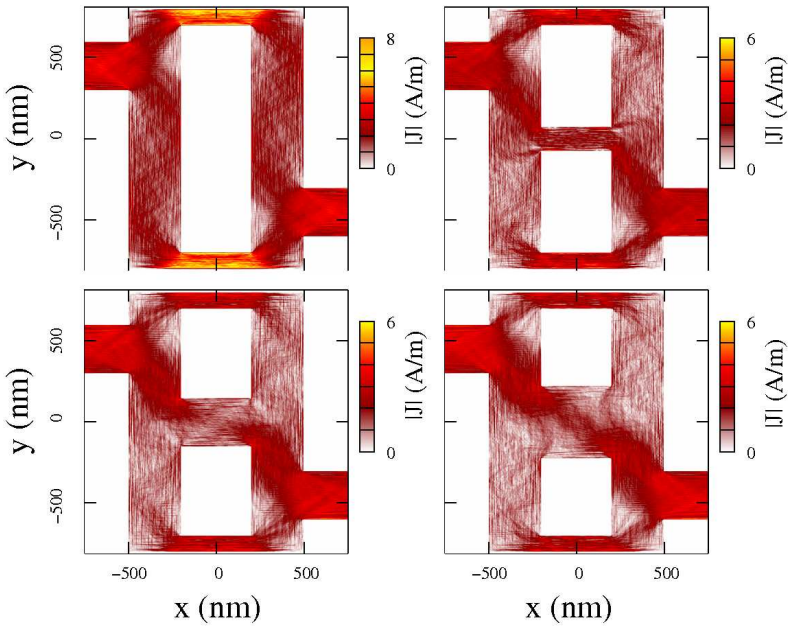

Figure 5.9: Contour plots of the absolute value of the current density distribution $|\mathbf{J}|(x, y)$ for the device configurations of Figure 5.8

Figure 5.8 illustrates the simulation, testing the occurrence of the Braess paradox. The structure takes the form of a 1.0μm $\times$ 1.6μm rectangular open dot that is connected to left (source) and right (drain) leads via two planar wires (openings) of width $W_{\text{open}} = 300$ nm each. A 0.4μm $\times$ 1.0μm central antidot defines two upper and lower wires of width $W_1 = W_2 = 100$ nm, which behave as constrictions for propagating electrons. A central wire directly connecting source to drain and opening an alternative third path to cross the antidot would intuitively result in an increase of current with respect to case (a). The properties of the third path can be studied by progressively increasing its width W like in cases (b), (c) and (d).

The choice of constrictions with total widths smaller than the opening widths ensures that the electron flow is congested. In a system where electrons can be back-scattered only by the walls defining the structure geometry, a sufficient condition to deal with a congested system is obtained when the number of conducting modes allowed by internal constrictions is smaller than the number of conducting modes in the external openings, which implies $W_1 + W_2 < W_{\text{open}}$.

In order to evaluate the transport properties of such a system we have adopted an exact numerical approach based on the Keldysh Green's function formalism to compute the transport properties of this rather complex system. The Green's function of the system is described in the real-space representation that allows us to take into account all possible conducting and evanescent modes. In order to reduce the computational time and memory requirements we adopt a recursive strategy that is based on the Dyson equation. In this framework the spatial distribution of the current along the propagation direction (x axis) between the nodes (x_{i+1}, y_k) and (x_i, y_k) reads

$$J_x(x_i \rightarrow x_{i+1}, y_k) = -\frac{4e}{h} \int d\omega \Re \left\{ H(i, i+1, k, k) G^<(i+1, i, k, k; \omega) \right\} \qquad (5.3)$$

where $H(i,k)$ represents the discrete Hamiltonian and $G^<(i, i', k, k'; \omega)$ is the lesser-than Green's function of the system in the real space representation and energy space.

In case of typical InGaAs/InAlAs heterostructures the electron concentration in the 2DEG results in a Fermi energy E_{F} of several tens of meV which, assuming an effective mass of 0.04 m_0, corresponds to a Fermi wavelength λ_{F} of tens of nm, and therefore to the injection of tens of conducting modes through the openings. The current has been calculated in the linear transport regime by applying a bias

voltage of 1 mV and a thermal average at 4.2 K has been done around E_F. The mesh size is $\Delta x = \Delta y = 2.5$ nm.

The right panel of Figure 5.8 reveals the occurrence of the Braess paradox by depicting the net current at the right lead $J(W)$ as a function of the width of the central wire. In order to demonstrate the robustness of the effect we have considered three different Fermi energies corresponding to $\lambda_F \approx 20$, 25 and 30 nm. Even if the intuition suggests that enlarging the central wire should increase the total current, we find that over a large width range, $J(W)$ monotonically decreases until loosing more than 10 percent of the initial value at around W=150/200 nm. Furthermore, as far as W becomes much larger than the opening width, it slowly increases and overcomes $J(0)$ only when the central path is large enough to strongly reduce reflections due to the antidot. This counter-intuitive behavior cannot be attributed neither to resonant effects due to the large number of conducting modes participating to the transport and the weak influence of λ_F, neither to conductance fluctuations which are of the order of 1 percent of the average conductance at T=4.2 K.

More physical insight into the W dependence of the net current is obtained by mapping the spatial distribution of the current density as computed from Equation 5.3. Figure 5.9 shows the current distribution $|\mathbf{J}|(x, y)$ obtained for the same configurations in Figure 5.8 and for $\lambda_F \approx 20$ nm. Congested electron flows are clearly observed in (a), where current maxima are located inside the upper and lower wires. The effect of adding a third path to electrons via the central wire is to reduce the congestion and hence to decrease the net current flowing in the two original paths. However, as long as the central wire is not large enough to permit a significant direct coupling between left and right contacts, the net current at the right lead decreases as a function of W. In the case of (b) the central wire is more coupled to the upper and lower constrictions rather than to the two openings, showing that when the Braess paradox occurs, electrons are quasi-bound in closed orbits inside the dot region. (c) and (d) show the cases when the coupling between the central wire and the two openings increases and becomes dominant with respect to the competing coupling between internal paths.

5.2.3 Braess paradox in quantum device: Experiments

5.2.3.1 Device

The 2DEG sample properties are described in Section 4.1.2. The fabrication process is described in Section 4.2, the UCL part. From the magnetoresistance measurement, we found a density $n_s = 3.5 \times 10^{11}$ cm^{-2} at $V_{bg} = 0$ (with the Hall bar located on the same sample). The SEM and topography images of the device are shown in Figure 5.10. The conductance measurement setup for SGM images is the same as that described in Section 4.4.

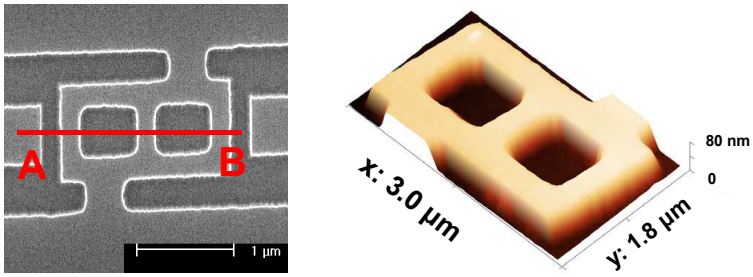

Figure 5.10: SEM and AFM topography images of the paradox devices. The AFM image is obtained at 4.2 K.

5.2.3.2 Point Spectroscopy

To test the presence of a Braess paradox effect as shown in the simulations, we fixed the tip above the central arm of the device, and measured the conductance of the device while sweeping V_{tip}. According to the simulation, as the width of the central arm becomes wider, the net current would exhibit a non-monotonic behavior. In real experiment, we are not able to increase the width of the electron channel, but instead we can reduce its effective size $W_{c,eff}$ by changing V_{tip} more negative. If the prediction is true in our device system, by decreasing V_{tip}, $W_{c,eff}$ would continuously decrease and in some regime of V_{tip}, we may find $dG/dV_{tip} < 0$ instead of the standard positive slope $dG/dV_{tip} > 0$.

The experimental curve shown in Figure 5.11 shows such a non-monotonic behavior around -3 V and also smaller fluctuations around 0 V. This type of curve can be obtained for several times, but with modifications depending on device history.

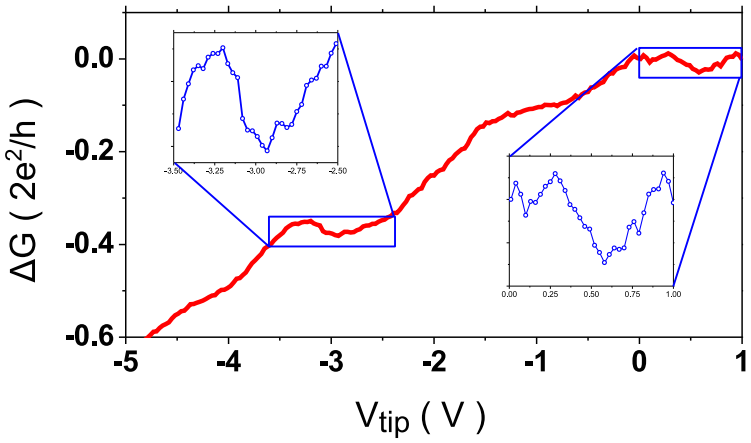

Figure 5.11: Point spectroscopy measurement, showing the Braess paradox effect around −3 V and 0 V. The measurement is performed with bias current $I_{AC} = 10$ nA and $d_{ts} = 100$ nm.

5.2.3.3 Line Spectroscopy

From the point spectroscopy measurements, we found that the appearance of Braess paradox effect is sensitive to the position of the tip, thus we performed spatially resolved measurements along a single line (line AB, see Figure 5.10) which crosses the central parts of all the three arms. The line spectroscopy measurement was performed as the procedure described in Section 5.1.2.

Figure 5.12 (b) and (d) show two conductance maps obtained with the 'line spectroscopy' method for different sample history. The conductance at zero tip voltage $G(V_{tip} = 0)$ is subtracted to enhance the gate effect. We therefore assume that there is no gate effect when V_{tip} equaled to zero (contact potential difference not taken into account) and remove the effect of the un-biased tip (screening, residual charges on the tip, etc.).

Voltage sweeps are extracted and plotted in Figure 5.12 (c) and (e). In (c), above the central arm (label i), the conductance shows a small non-monotonic dependence on V_{tip} recorded in the range of $[-3.6V, -3.2V]$ and another one in the range of $[+0.4V, +0.8V]$ (inset), i.e., with the decreasing of V_{tip}, the conductance did not decrease but increase instead. In (e), at the vicinity of central arm on right side (label ii), we can see a stronger feature in the range of $[-1.3V, -0.3V]$.

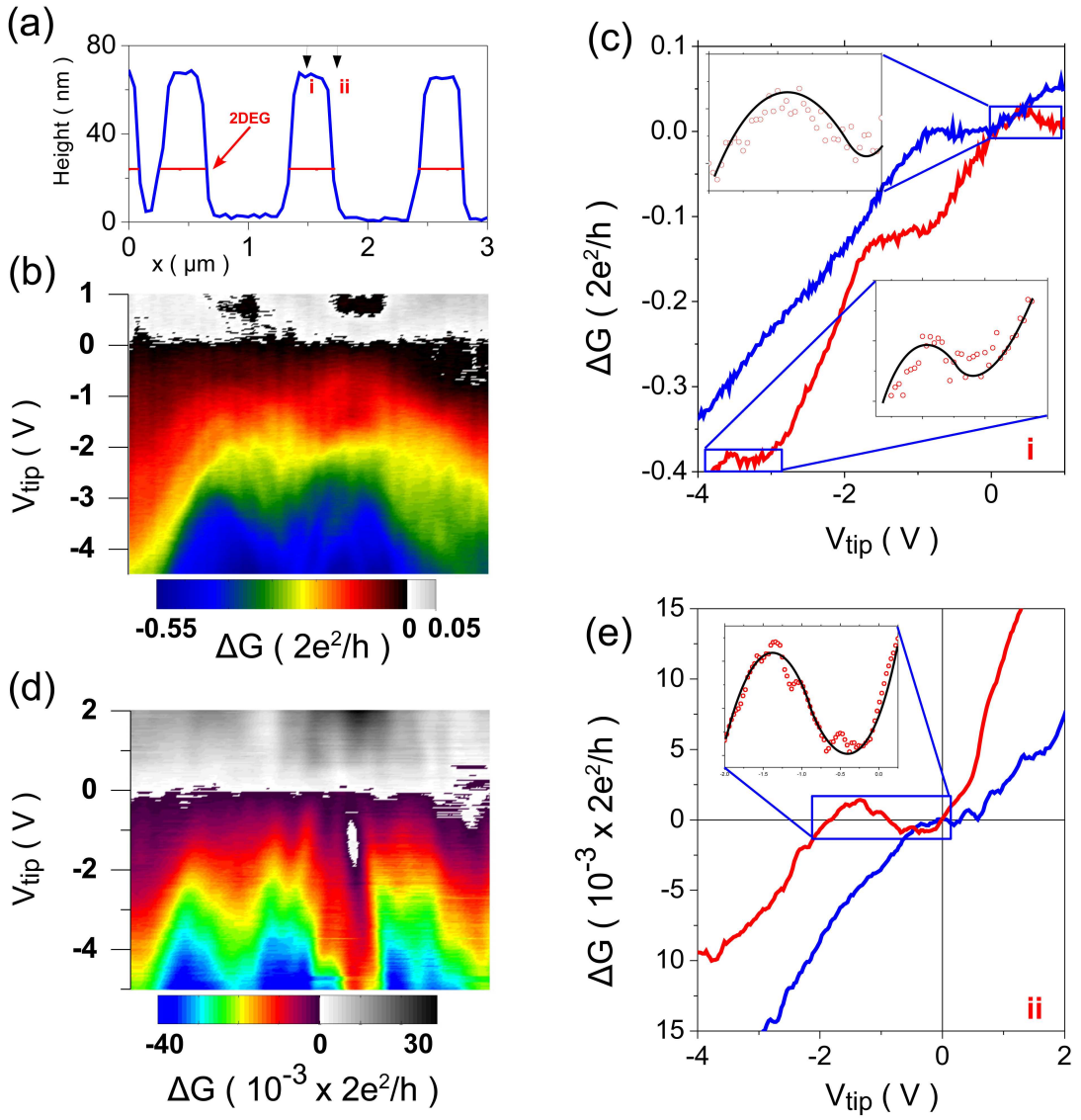

Figure 5.12: (a) Topographic profile along line AB as shown in Figure 5.10. (b) and (d): V_{tip} and spatially resolved conductance maps obtained from 'line spectroscopy' measurement along line AB for different sample history. Both these two measurement are performed with a bias current I_{AC} = 10 nA and d_{ts} = 100 nm. (c) and (e): Conductance profiles extracted from (b) and (d) respectively. The red curves are extracted at the points (i) and (ii) as depicted in (a). The blue curves are the averaged conductance profiles over the line AB.

For comparison, we also show the averaged conductance profiles (averaged over the line AB) in blue curves in Figure 5.12 (c) and (e). These averaged profiles show a more monotonic dependence on V_{tip}. This indicates that the non-monotonic behaviors are local effects, which only occur around the central arm: this is supported by the absence of features at other locations.

In different measurements, the differences in the positions where the non-monotonic events occur could be related to the differences of tip-induced potential experienced by the electrons, that varied in different experiments due to the different shapes and tilted angle of tips, and the different background charge states of the devices. These effects also influence the magnitude of the conductance 'valley' and the value of the tip voltage where the Braess effect occurs.

5.2.3.4 Influence of back gate and side gate

To study further the Braess paradox dependences on the widths of two side arms and on the Fermi wavelength (λ_{rmF}), We performed point spectroscopy with different side gate voltage V_{sg}, and back gate voltage V_{bg} respectively. The results are shown in Figure 5.13.

From (a) and (b), we can see as V_{sg} decreases, the two non-monotonic regions at $V_{tip} = -1.7$ V, -3.9 V (i and ii in (a), I and II in (b)) stand unchanged for V_{sg} in the range of [-0.5V, 0V][1]. The analysis of (b) indicates that for $V_{tip} > -3$V, the conductance slightly decreases as V_{sg} decreases, due to the depletion by V_{sg} that reduces the effective channel widths of two side arms. However, as $V_{tip} < -3$V, the conductance does not change with respect to V_{sg}. The gate effect experienced by the two side arms are dominated by V_{tip}, rather than V_{sg}. This can be interpreted as the electrical field from metallic layer on the tip is much stronger than from the thin layer of 2DEG, although the distance is about twice larger (screening effect).

The difference in the curves shown in (a) and (c) is due to a slight position shift (a few tens of nm) between these two measurements. From (c) and (d) recorded at a different time, we found that the non-monotonic region (iii) only appears at $V_{bg} > 0$V (III in (d)); and region (iv) starts to appear from $V_{bg} = 0.075$V, and is visible down to $V_{bg} = -0.225$ V (IV in (d)). As V_{bg} decreases, the V_{tip} value of region (iv) increases. This feature cannot be interpreted by the change of Fermi

[1]The lower limit of V_{sg} is set at -0.5 V to avoid leakage current between the side gates and the device.

wavelength λ_F because 0.3V change of V_{bg} only induces a 5%[1] change of λ_F.

Interestingly, we observed multiple non-monotonic regions. This feature is not clearly understood from the simulations, and will be explored in future investigations.

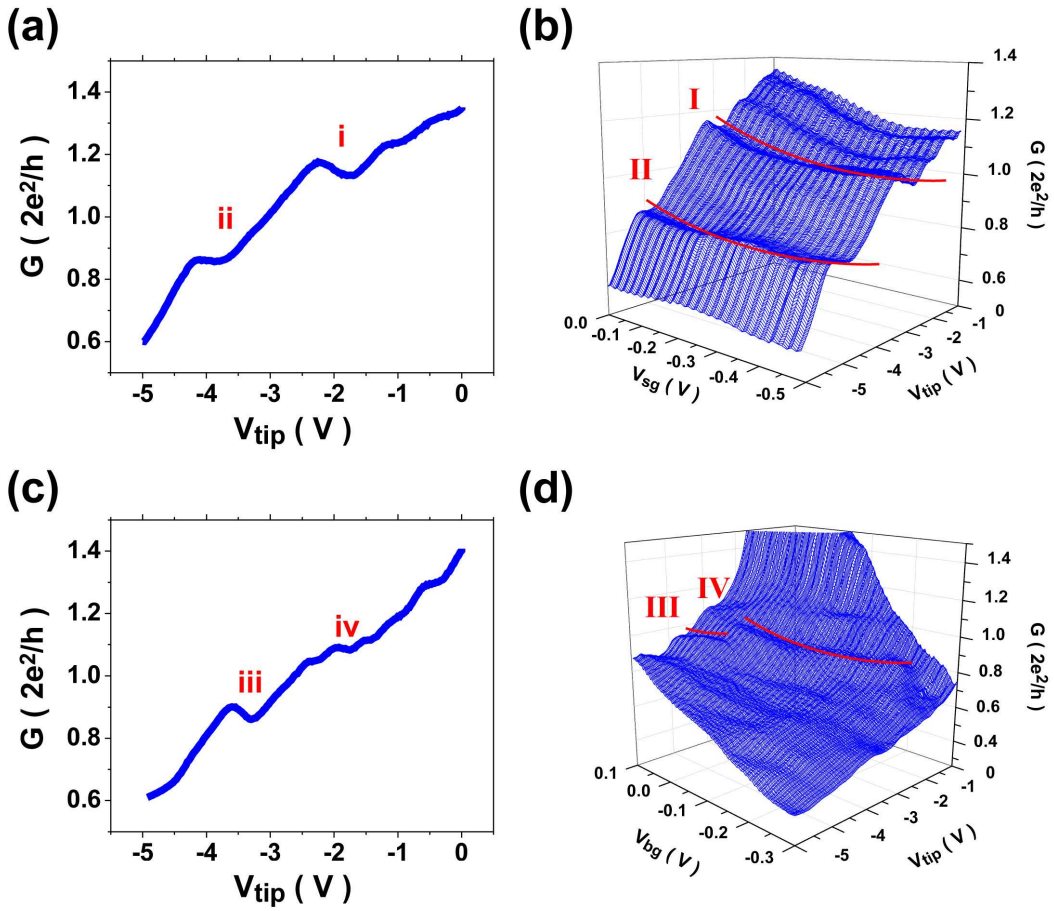

Figure 5.13: (a) and (c): Point spectroscopy measurements obtained at $V_{bg} = V_{sg} = 0$ above the central arm. (b) V_{sg} resolved point spectroscopy measurement performed right after (a). (d) V_{bg} resolved point spectroscopy measurement performed right after (c). All the measurements are performed with a bias current $I_{AC} = 10$ nA and $d_{ts} = 100$ nm.

[1] According to the SdH measurements shown in Figure 4.2, at $V_{bg} = 0$, $\lambda_F = 42$ nm; at $V_{bg} = -0.3$ V, $\lambda_F = 44$ nm.

5.3 Imaging single charge traps

Charge traps have been studied in the field of electronics for a long time. When the trap is close to the electron channel, the trapped charges induce a local electrostatic potential that scatters the conducting electrons. As a consequence, thus the performance of semiconductor devices will be degraded, e.g., lower carrier mobility [81], threshold voltage instability [82, 83], lower efficiency of solar cell [84, 85], etc. The origins of charge traps vary in different materials or device structures. Generally speaking, the traps can be formed due to surface/interface states [86, 87], dopants [88], vacancies [89] or dislocations [90]. Most of the time, people do not want to have charge traps in the devices. However, charge traps can be implemented in new conceptual devices, for example charge trap flash memory [91, 92], which stores the information in charge traps located in the dielectric layer between gate and channel. The locations of the charge traps can be determined by means of EFM [93], electroluminescence [94], STM [95] and SGM [96, 97].

In the following, we present our work of imaging charge traps in a nanodevice (the same device as used in the study of the Braess paradox). This part is organized as follows: (1) discovery of charge traps in conductance maps, (2) direct mapping of charge traps by means of transconductance measurement, (3) relations between charge traps and device conductance, and (4) determination of the vertical position of the traps.

5.3.1 Discovery of charge traps by SGM

In Figure 5.14, (a)-(m) show conductance maps obtained in SGM mode by changing V_{tip} from -3.6 V to $+3.6$ V with a step of 0.6 V (details in the caption) and (n) schematically shows the current paths across the device in the absence of tip. We will use this drawing to interpret the features in the SGM images.

Discussion of Figure 5.14

1. In (a-f), there is a large response centered on the device. The decrease of conductance is due to the smaller electron density (depletion). In (g), $V_{tip} = 0$, there is no response. In (h-m), $V_{tip} > 0$, there is small response centered on the device. The increase of conductance is due to the larger electron density (accumulation).

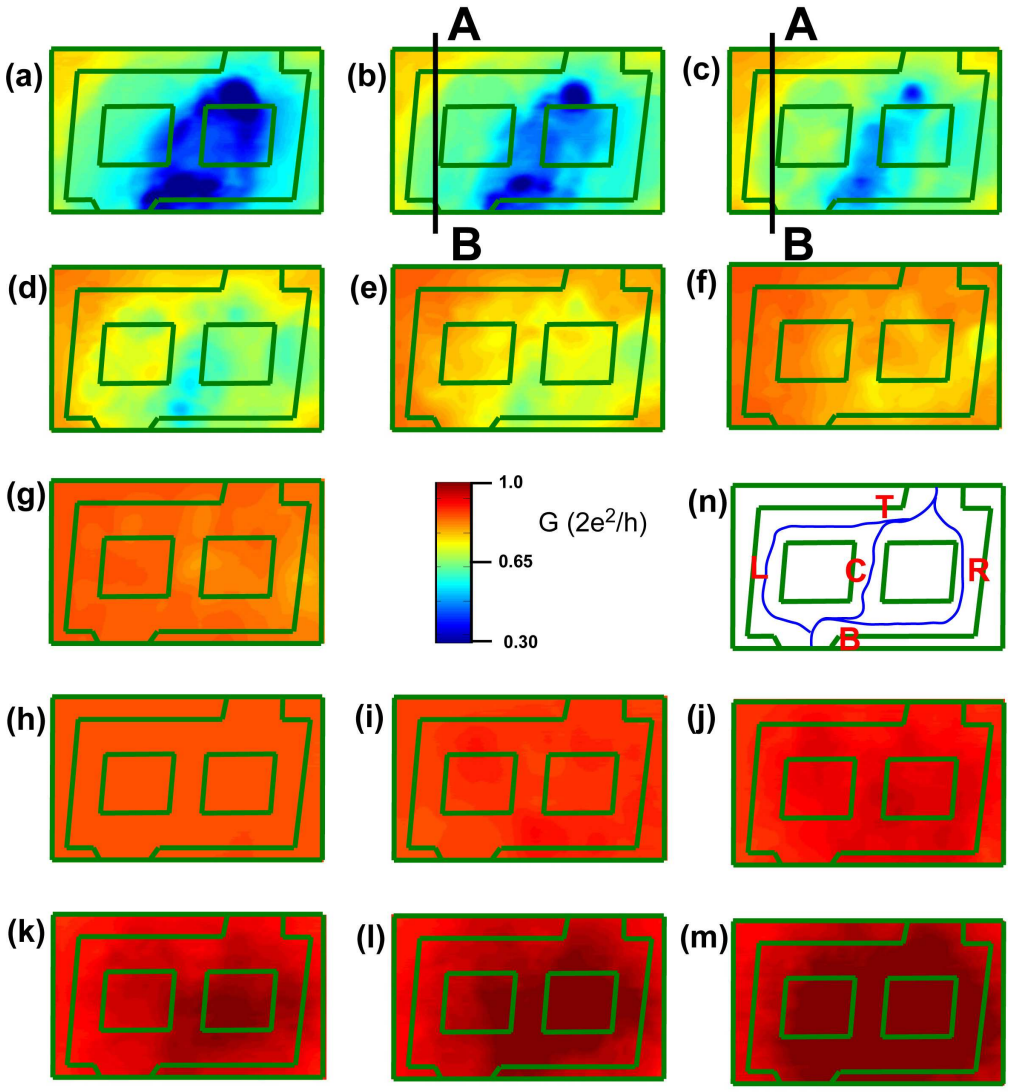

Figure 5.14: SGM images. (a)-(m) Conductance map obtained with d_{ts} = 100nm, V_{tip}=−3.6 V (a) to +3.6 V (m), increasing step ΔV=+0.6V. The conductance is measured by lock-in with the 4-probe current bias configuration, with I_{AC}=10 nA@68 Hz. Scanning speed: 200nm/s. (for all the experiments presented in the following, the speed is the same.) A topography image taken after the last SGM scan confirms that the position shift during this SGM experiment for about 15 hours is less than 10 nm. (n) Schematic of current flow across the different device paths.

2. When the negatively biased tip is placed above position 'T', the current through left (L) and central (C) arms is partially blocked because of depletion induced by the tip potential. Symmetrically, the same situation occurs when the tip is moved to position 'B'. As a result of such partial depletion, the conductance of device decreases, as can be seen clearly in Figure 5.14 (b), i.e., at the vicinity of two openings, the presence of the tip leads to a minimum of conductance as indicated by the two darkest blue spots. The device openings show a smaller response than 'T' and 'B' because of their larger widths.

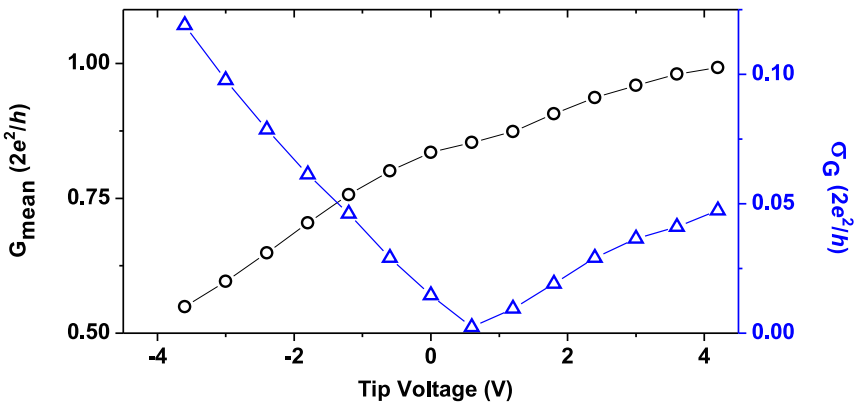

Figure 5.15: Mean value of the conductance G_{mean} and standard deviations of conductance σ_G calculated for each conductance map of Figure 5.14 (a)-(m).

Figure 5.15 shows the mean values G_{mean} of the conductance averaged over each map of Figure 5.14 (a)-(m), as well as the standard deviation σ_G, calculated as:

$$G_{mean} = \frac{\sum_{map} G(x,y)}{n_x \cdot n_y}\ ,\ \sigma_G = \sqrt{\frac{\sum_{map} [G(x,y) - G_{mean}]^2}{n_x \cdot n_y}}$$

where n_x and n_y are the pixels number in x and y directions.

- The curve of G_{mean} can be interpreted with the model discussed in Sec 4.5, i.e., the conductance exhibits a linear dependence on V_{tip} (the tip is the gate in our case) in the linear regime ($V_{GS} > V_{th}$ and $V_{DS} \ll V_{GS} - V_{th}$).
- The minimum of σ_G occurring at $V_{tip} = 0.6V$ means that the conductance fluctuations (gate effect) are minimized around $V_{tip} = 0.6V$. In Figure 5.14 (h), the conductance map is indeed almost homogeneous. Thus we can speculate the contact potential $\Delta\mu_{ts}/e$ to be around 0.6V. In Section 4.4,

the contact potential between the tip and InAlAs layer is determined to be 0.19V by electrostatic force measurement. In the present device, we were not able to extract the contact potential from the electrostatic force probably due to the quite low electron density of the 2DEG layer.

This result indicates that the appearance of the conductance map can be explained by the spatial distribution of the tip induced potential that induces a global response over a large area of the device; and by local electronic effects that create local fluctuations in the conductance map. The conductance therefore appears as the sum of global and local responses, and can be expressed as:

$$G(V_{\text{tip}}) = G_{\text{global}}(V_{\text{tip}}) + G_{\text{local}}(V_{\text{tip}}) \tag{5.4}$$

where G_{global} is linear with V_{tip}. Hence we get:

$$\frac{\Delta G(V_{\text{tip}})}{\Delta V_{\text{tip}}} = \frac{G(V_{\text{tip}} + \Delta V_{\text{tip}}) - G(V_{\text{tip}})}{\Delta V_{\text{tip}}} = \text{const.} + \frac{\Delta G_{\text{local}}(V_{\text{tip}})}{\Delta V_{\text{tip}}} \tag{5.5}$$

The difference of two conductance maps obtained with adjacent V_{tip} will therefore reveal the information of $G_{\text{local}}(V_{\text{tip}})$. Figure 5.16 shows the results of $\Delta G(V_{\text{tip}})$ obtained by subtracting one conductance map from its neighbor in Figure 5.14 ($\Delta V_{\text{tip}} = 0.6$V).

Discussion of Figure 5.16

1. In Figure 5.16 (a)-(e), ring(ellipse)-shaped contours appear in some regions, (marked by black lines in (c)). From (f) to (l), these contours start to disappear, showing that the appearance of such contours is dependent on the polarity of V_{tip}.

2. The centers of the contours are located within the device region, rather than the area where 2DEG is etched away. Hence the patterns originate from interactions between the 2DEG channel and the heterostructures nearby.

3. The size of these contours increases when V_{tip} becomes more negative. Similar features have been reported in SGM experiments studying Coulomb blockade in quantum dots [19, 23, 43]. So, we may suspect the contour is related to a single electron phenomenon.

Figure 5.17 (a) shows the extracted profile from the conductance difference maps. The edges of the circular contours appear as a set of two peaks (green

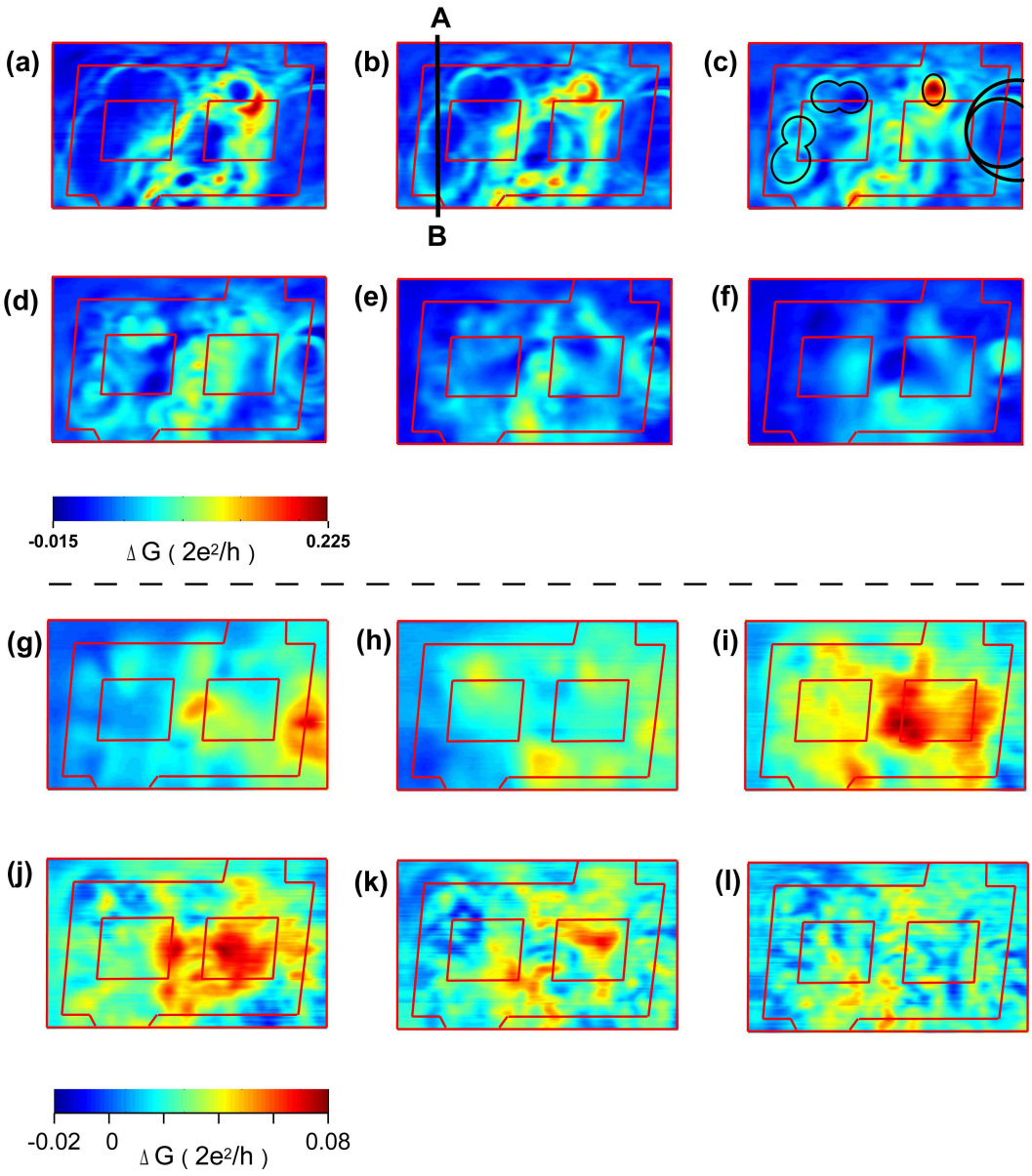

Figure 5.16: (a)-(l) Maps of conductance difference $\Delta G = G(V_{tip}) - G(V_{tip} - 0.6V)$ calculated from Figure 5.14 (a)-(m). (a)-(f) Negative tip voltages around the average voltage $\bar{V}_{tip} = V_{tip} - 0.3$ V=−3.3 V (a) to −0.3 V (f). (g)-(l) Positive tip voltages around the average voltage $\bar{V}_{tip} = V_{tip} - 0.3$ V=+0.3 V (g) to +3.3 V (l).

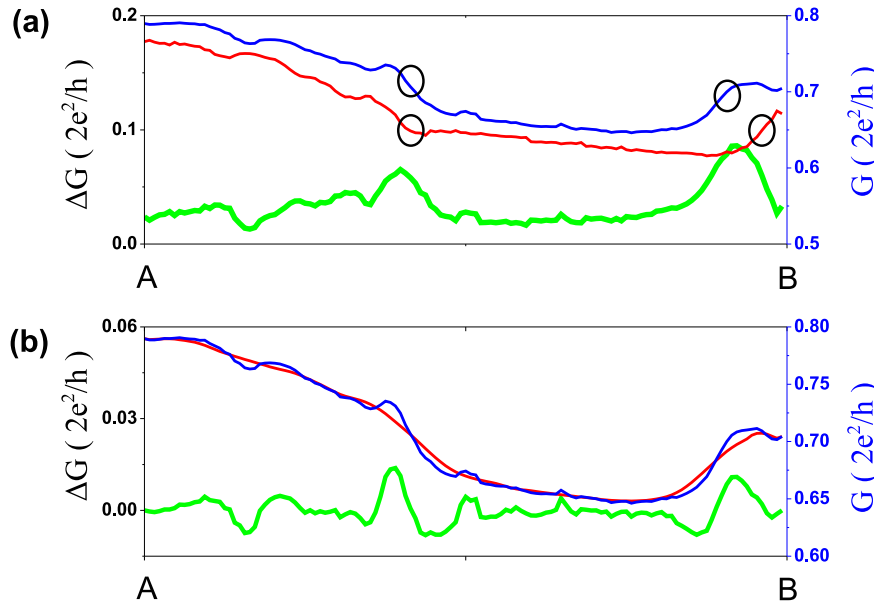

Figure 5.17: (a) Blue and red: conductance profiles extracted from line AB respectively in Figure 5.14 (c) ($V_{tip} = -2.4$ V) and (b) ($V_{tip} = -3.0$ V). Green: conductance profile extracted from line AB in Figure 5.16 (b) which is the difference of the blue and the red curves. (b) Blue: conductance profile extracted from line AB in Figure 5.14 (c). Red: smoothed result of the blue curve. Green: result of subtracting the red curve from the blue curve.

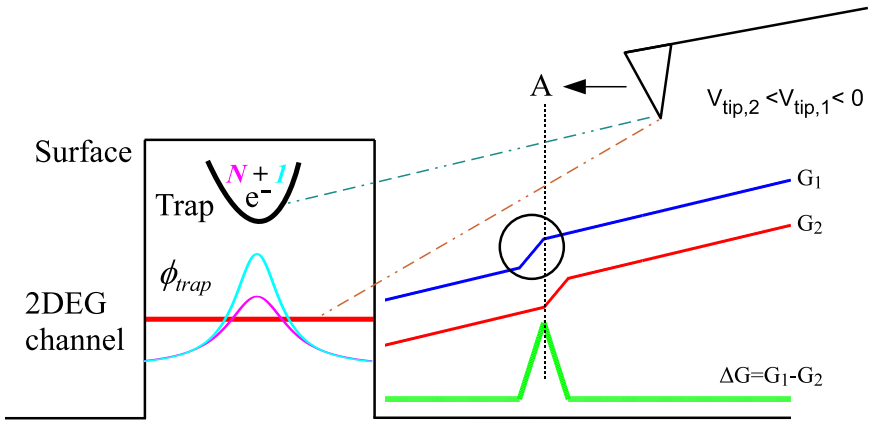

Figure 5.18: Schematics of the charge trap model described in the text..

curve). However, the conductance profiles (blue and red curves) extracted from the original conductance maps (Figure 5.14) only show tiny decreases of conductances indicated by the black circles. The conductance difference (green curve) is therefore useful to enhance the features of G_{local} superimposed on G_{global}.

Figure 5.17 (b) also shows that these features become more visible if the background of G_{global} is removed by subtracting a smoothed curve. The resulting curve (green in (b)) is close to the curve obtained by differencing two maps (green in (a)).

From this discussion, we can speculate that the decrease of conductance inside the circular contours is due to charge traps located at the center of the contours. A model describing the interactions between tip, trap and conduction channel is schematically depicted in Figure 5.18. The electrostatic potential ϕ_{trap} induced by the trapped electrons (number N) scatters the electron flow in the 2DEG channel and contributes to increase the value of the resistance. In SGM experiment with $V_{tip} < 0$, the depletion induced by V_{tip} decreases the overall conductance of the device (G_{global}) and when the tip arrives at some point (A), the trap is charged with an additional electron (from e.g. the cap layer at the surface) and the number of electrons inside the trap is increased by one ($N \rightarrow N + 1$), thus ϕ_{trap} is raised (from magenta to cyan), and we observe a sudden decrease of conductance (G_{local}). The resulting profile of $G = G_{global} + G_{local}$ is shown by the G_1 curve in Figure 5.18, that reproduces the experimental curve presented in Figure 5.17. The black circle on the G_1 curve indicates the decrease of G_{local}. If V_{tip} becomes more negative, along the same scanning path, the conductance G_{global} will become smaller and the position where G_{local} changes will be farther from the trap compared to G_1 curve, as shown by the G_2 curve. This subtle decrease becomes a sharp peak in the plot of $\Delta G = G_1 - G_2$ (green curve in Figure 5.18 and in Figure 5.17 (a)). If $V_{tip} > 0$, approaching the tip to the trap does not remove electrons out of the trap, thus ϕ_{trap} remains unchanged and no sudden conductance change appears.

5.3.2 Direct imaging of charge traps

We now know that the contours shown in the plot of $\Delta G(V_{tip})$ in Figure 5.16 reveal the information of the local conductance changes versus tip voltage, $\Delta G_{local}(V_{tip})$. To study in more details $\Delta G_{local}(V_{tip})$, we rewrite Equation 5.5 in the form:

$$\frac{dG_{local}(V_{tip})}{dV_{tip}} = \frac{dG(V_{tip})}{dV_{tip}} - \text{const.} \tag{5.6}$$

Equation 5.6 indicates that the local response can be measured by differentiation of G versus V_{tip}. This can be done with differential measurement, i.e., by adding a small AC perturbation voltage V_{tip}^{AC} on V_{tip}^{DC}, and measuring the conductance change at the same frequency as V_{tip}^{AC}.

Assuming the device is biased with a DC current I_0, the voltage across the device V_{device} as a function of V_{tip} can be expressed as:

$$V_{\text{device}}(V_{\text{tip}}) = I_0 \cdot R(V_{\text{tip}}) = I_0 \cdot \left[R(V_{\text{tip}} = 0) + \frac{dR}{dV_{\text{tip}}} V_{\text{tip}} + \mathcal{O}(V_{\text{tip}}^2) \right] \tag{5.7}$$

Considering the signal V_{device}^{AC} at the frequency of V_{tip}^{AC}, and the relation R = 1/G, we get:

$$V_{\text{device}}^{AC} = I_0 \cdot \frac{dR}{dV_{\text{tip}}} \cdot V_{\text{tip}}^{AC} = \frac{I_0}{G^2} \cdot \left(-\frac{dG}{dV_{\text{tip}}} \right) \cdot V_{\text{tip}}^{AC} \tag{5.8}$$

Thus, the local response will be obtained experimentally with the following relation:

$$\frac{dG}{dV_{\text{tip}}} = -\frac{G^2}{I_0} \cdot \frac{V_{\text{device}}^{AC}}{V_{\text{tip}}^{AC}} \tag{5.9}$$

The derivative of G can also be written as: $dG/dV_{tip} = dI/(V_{ds}dV_{tip}) = g_m/V_{ds}$, where $g_m = dI/dV_{tip}$ is defined as the transconductance of device, and we get:

$$g_m = -G \cdot \frac{V_{\text{device}}^{AC}}{V_{\text{tip}}^{AC}} \tag{5.10}$$

Transconductance is one important parameter of an electronic device, which reveals the response in drain current to the change in gate voltage. The maps of the conductance difference shown in Figure 5.16 therefore reveals approximately the information of transconductance variations of the device with the tip as gate. The method of adding a small AC modulation on V_{tip} not only increases the signal-to-noise ratio, but also offers the possibility to directly map the spatial variations of g_m. Figure 5.19 (a)-(h) show the results of measuring dG/dV_{tip} with a current I_0=10 nA and a modulation V_{tip}^{AC} = 40 mV@930 Hz for a few V_{tip}^{DC} values.

Discussion of Figure 5.19

1. Compared with Figure 5.16, similar contours appear in Figure 5.19 which consist in several sets of concentric rings, but the spatial resolution is increased as expected by measuring dG/dV_{tip} instead of $\Delta G/\Delta V_{tip}$.

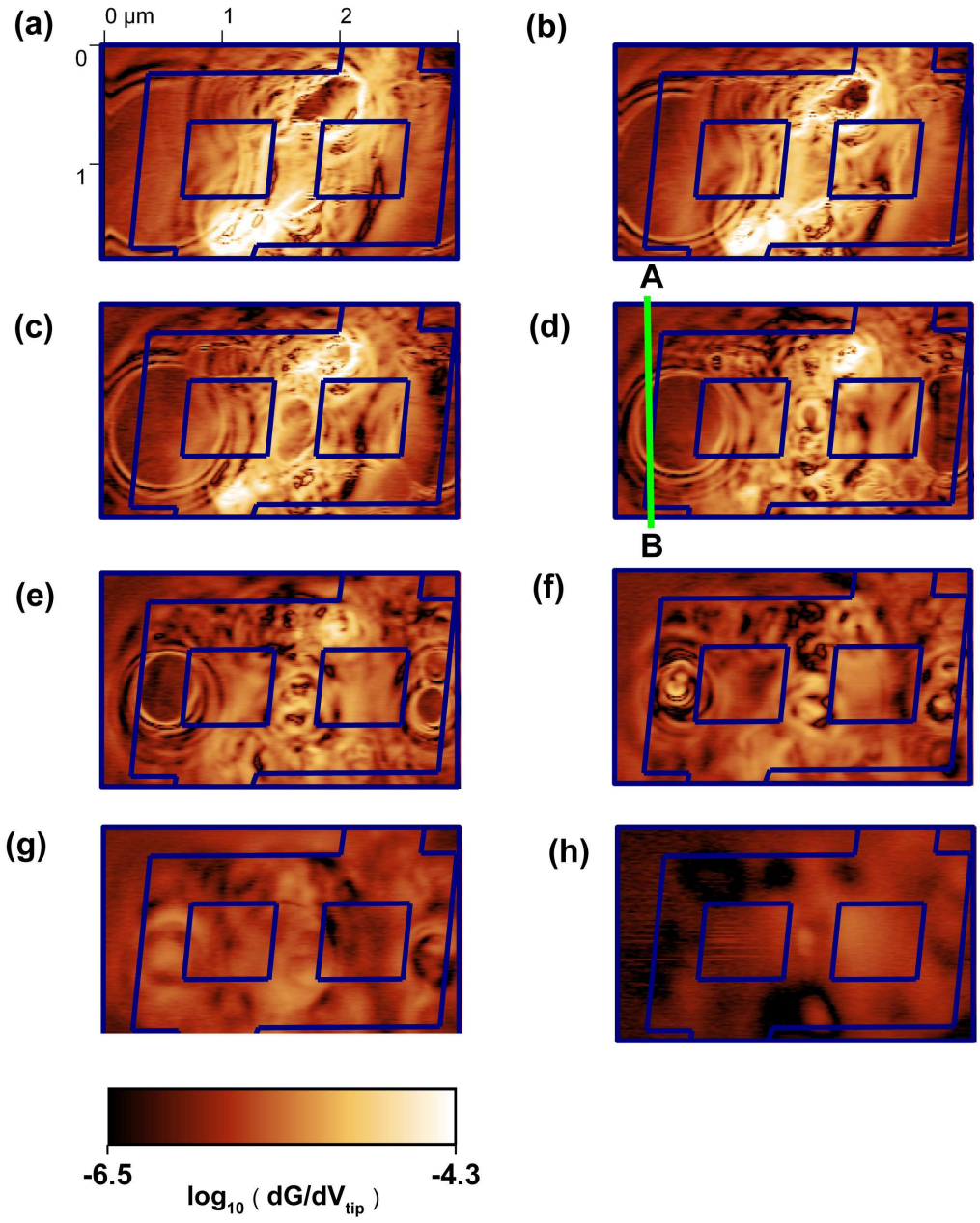

Figure 5.19: Transconductance maps obtained with $I_0 = 10$nA, V_{tip}^{DC}=−3.6V (a) to +0.6V (h), increasing step ΔV=+0.6V, $d_{ts} = 100$nm, $V_{tip}^{AC} = 40$ mV@930 Hz. The unit of dG/dV_{tip} is S/V, plotted in $\log_{10}$ scale.

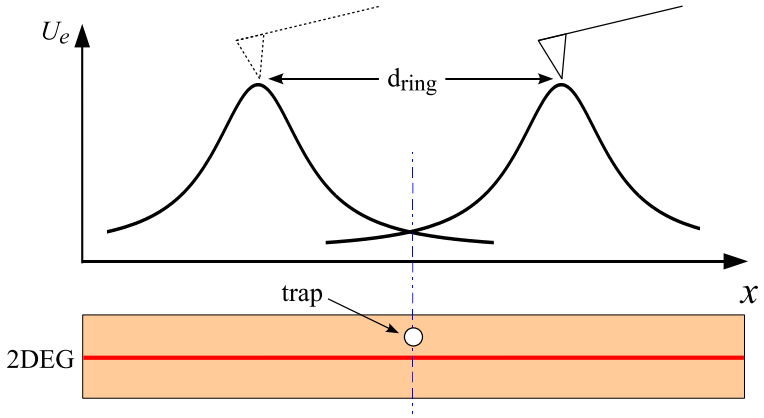

Figure 5.20: Schematic of the electrostatic potential induced by V_{tip} at the trap position when the tip is moving along a transconductance contour with a diameter of d_{ring}.

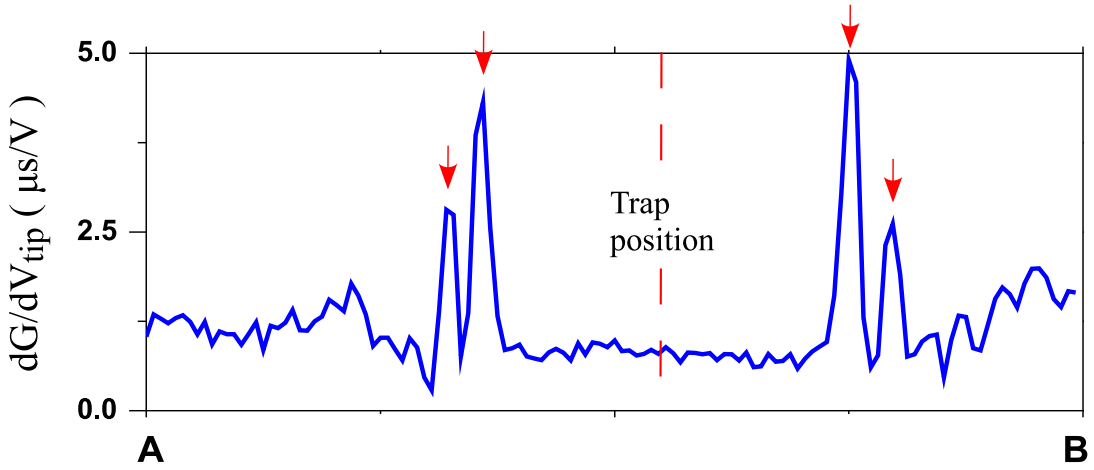

Figure 5.21: Profile of the transconductance map along the line AB in Figure 5.19 (d) crossing two concentric rings centered on a trap.

2. From the trap model, we know that each individual ring is related to a given number of electrons inside the trap. The V_{tip} induced potential U_e in the trap is therefore constant as the tip moves along a ring centered on the trap (Figure 5.20).

3. The extracted transconductance profile shown in Figure 5.21 confirms the model proposed in Figure 5.18. The positive derivative on the rings is consistent with the charging of the traps when the tip voltage is more negative.

4. The existence of several concentric rings indicates that the event of 'single electron charging into the trap' occurred several times (equals to the number of concentric rings) as the tip approaches to the traps positions (center of the rings). The observation of discrete rings is a signature of Coulomb blockade in the trap with a charging energy larger than the temperature.

5. The rings that appear in the left arm are found to be discontinued at the top-left arm of the device in (a), (b) and (c). This is because in that region, the tip is interacting with other traps simultaneously blocking the current in this arm. As the amplitude of V_{tip} becomes smaller in (d) and (e), the rings become smaller and do not overlap.

The same experiment was performed later, after the device was reset by illumination with an orange LED, and after waiting a long time for the stabilization of the photo-generated excessive carriers. The result of this measurement with a DC current $I_0 = 20$ nA is shown in Figure 5.22.

Discussion of Figure 5.22

1. Compared to Figure 5.19, both the number and the position of traps have changed in Figure 5.22. After numerous experiments, we have learnt that the formation of electron traps strongly depends on the 'history' of the device. The factors that affect such formations include the cooling of the sample, the electrostatic discharge, and the photon illumination.

2. In the central arm (and near the top opening), the ring-shaped contours are more visible than in Figure 5.19. The coupling of multiple traps in this region is extremely strong.

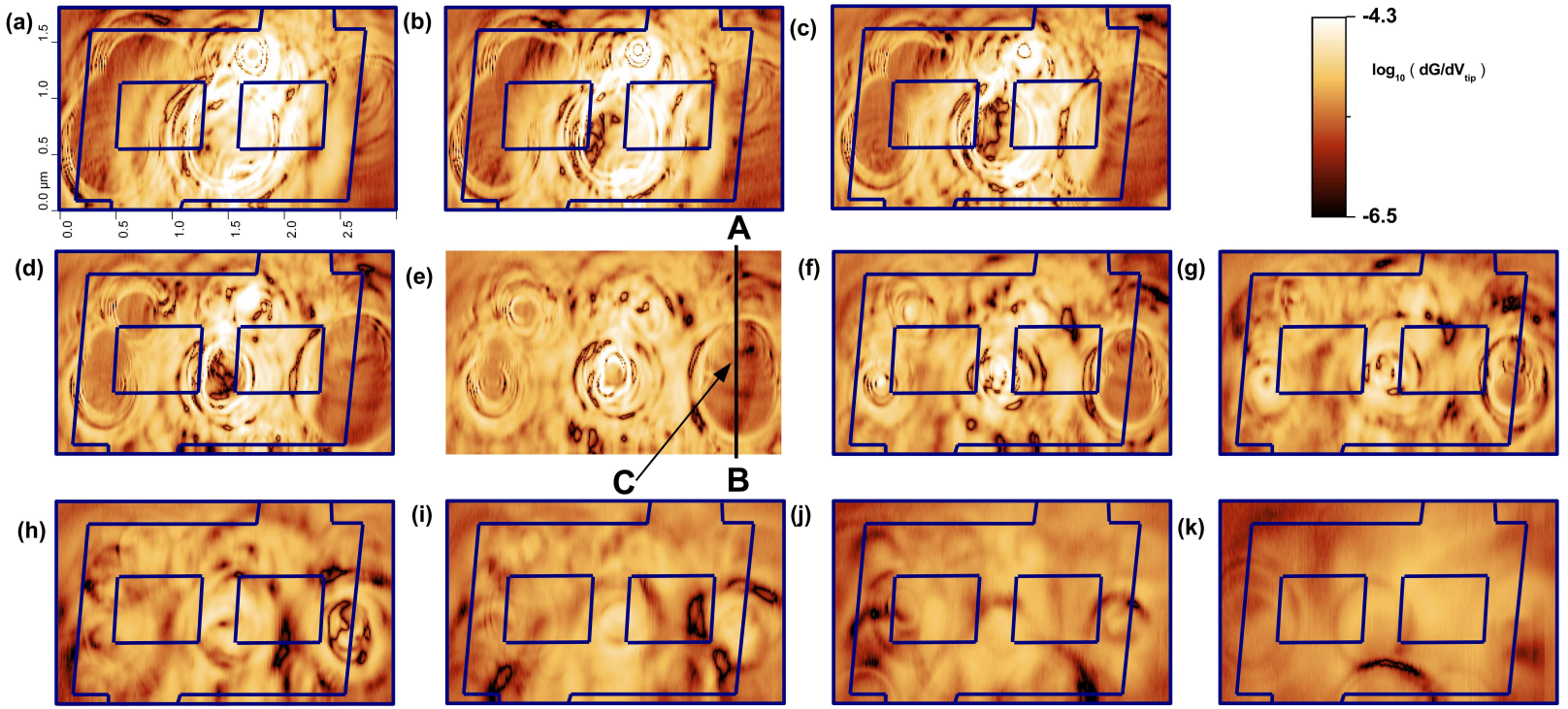

Figure 5.22: Transconductance maps obtained with $I_0 = 20$ nA, $V_{tip}^{AC} = 40$ mV@930 Hz. V_{tip}^{DC}=−5.0V (a) to 0V (k), increasing step ΔV=+0.5V. $d_{ts} = 100$ nm. The unit of dG/dV_{tip} is S/V, plotted in $\log_{10}$ scale.

3. The absence of ring inside the large rings does not necessarily mean that the number of charge is fixed (trap full/empty), but that the conductance becomes insensitive to the trap charges. This can occur if the channel is fully depleted (see discussions later in Figure 5.24).

Assuming that the V_{tip} induced potential has a Lorentzian function shape, the diameter of a ring d_{ring} is related to V_{tip} by:

$$U_e = V_{tip} \cdot \frac{\beta}{(d_{ring}/2)^2 + w^2} = \text{const.} \Rightarrow V_{tip} = a \cdot d_{ring}^2 + b \tag{5.11}$$

Equation 5.11 predicts that for a contour, V_{tip} is a parabola function of d_{ring}. A precise $d_{ring} - V_{tip}$ measurement is presented in Figure 5.23.

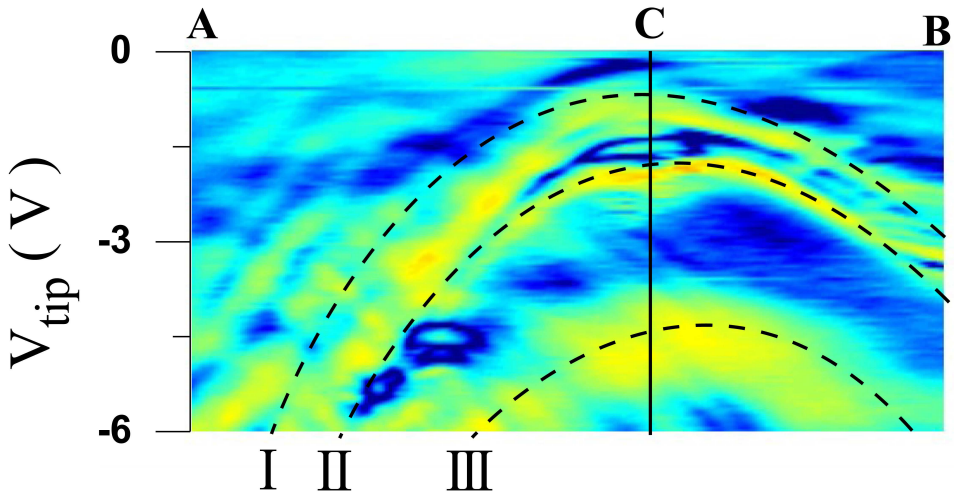

Figure 5.23: V_{tip}^{DC} resolved line spectroscopy along the line AB depicted in Figure 5.22 (e).

A single line spectroscopy has been done along the right arm as indicated by the line AB in Figure 5.22 (e), crossing a large ring centered point C. The result shown in Figure 5.23 shows the dependence of the transconductance contours on the amplitude of V_{tip}^{DC}. This feature can be analyzed with the same theory discussed in the section on QD, the difference here is that transconductance replaces conductance. The Lorentzian distribution of the tip induced potential results in several parabolas for the iso-transconductance lines, as guided with dashed lines. The different lines are associated with different numbers of trapped electrons. The absolute value of N is not known. These iso-transconductance lines correspond to the same point C, which is the trap position.

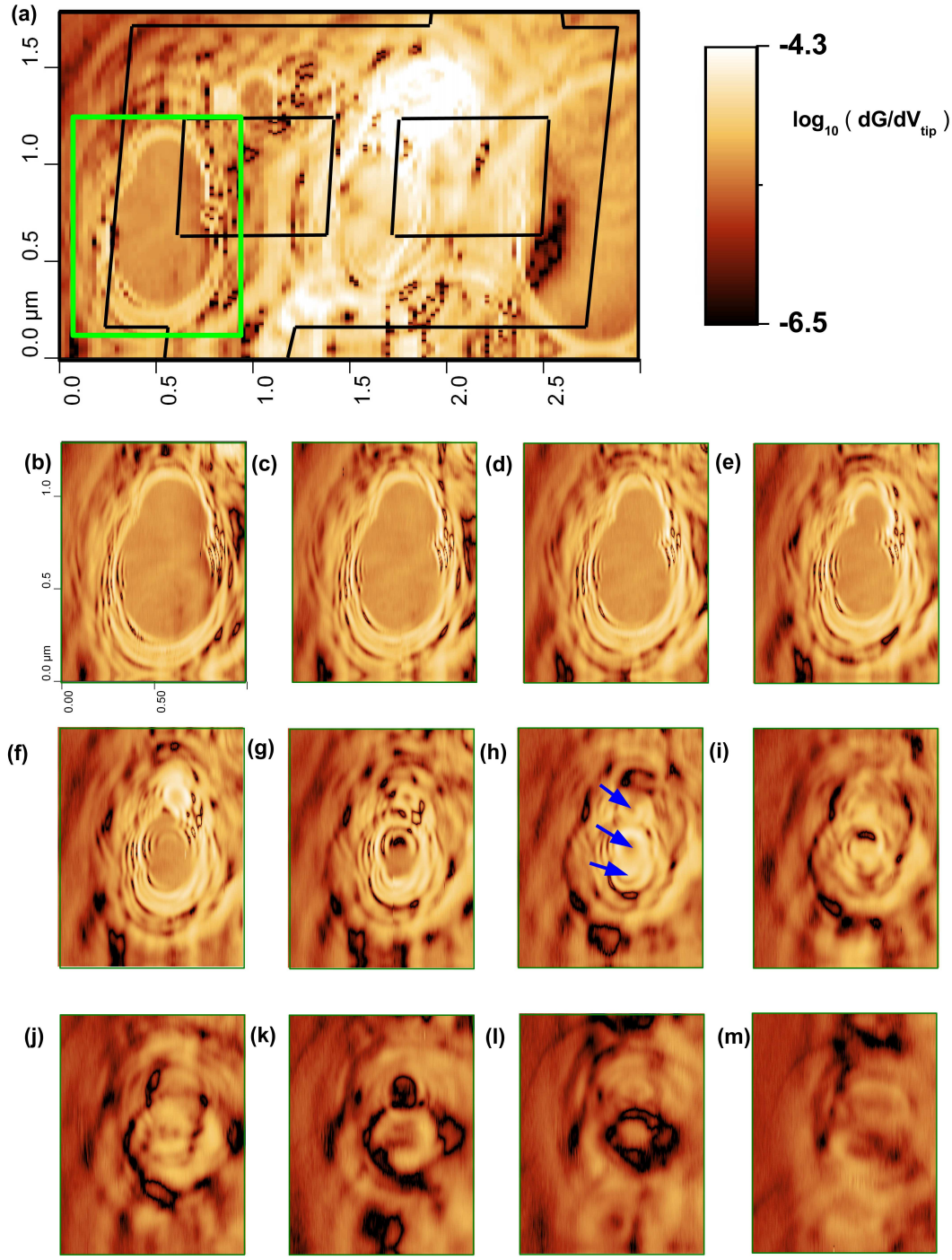

Figure 5.24: Transconductance maps measured with d_{ts} = 100nm, I_0 = 20nA, V_{tip}^{AC} = 40 mV@930 Hz. (a) Transconductance map obtained with $V_{tip}^{DC} = -4$ V; (b)-(m) Zoom of the region in the green rectangle in (a) with V_{tip}^{DC}=−4.0V (b) to −0.7V (m), increasing step $\Delta V = +0.3$V. The unit of dG/dV_{tip} is S/V, plotted in $\log_{10}$ scale.

In Figure 5.24, we show a zoom in a small region measured with different V_{tip}^{DC}. The number of traps can be determined to be 3, as indicated by arrows in (h). In (b-e), we find there exists a shadow region, within which the transconductance is constant. One possible interpretation is when the tip is flying above this region, the left arm is fully blocked, and any further changes in trapped charges disappear from the conductance measurement.

Besides the features already discussed above, we observed several sets of fringes near the 'main' rings. The spacing between adjacent fringes is much smaller than that of 'main' rings. The fringes show strong anisotropy, i.e., they are found only in the horizontal direction (fringes are essentially vertical). These fringes could be related to interference of electrons, but we could not find a consistent model to explain them.

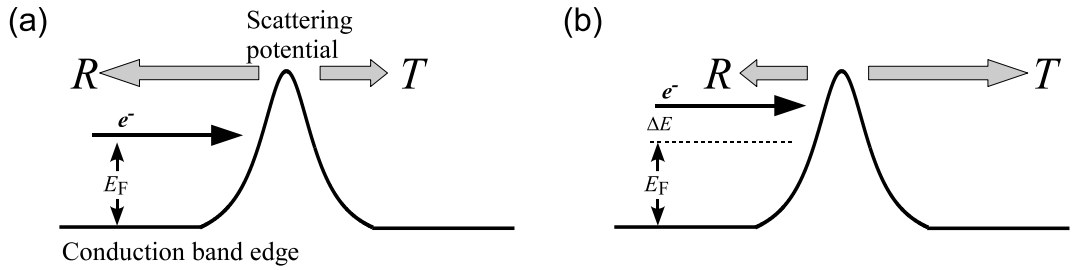

Figure 5.25: Schematics of the electron transport with the presence of scattering potential. From (a) to (b), the kinetic energy is increased by ΔE.

Transconductance Measurement at different DC currents

In previous discussions, we proposed that the electrostatic potential induced by the trapped electrons becomes scattering centers for the electron flow in the 2DEG channel. In principle, the scattering magnitude depends on kinetic energy of incoming electrons and the height of the scattering potential barrier. As the kinetic energy of transport electrons increases, the scattering magnitude would decrease, thus the transconductance would decrease, and it would change the SGM images, as schematically depicted in Figure 5.25. Based on this simple prediction, we performed SGM measurements with different DC currents across the device while keeping the same V_{tip}. Figure 5.26 shows the transconductance maps obtained with different current values in the range [−60 nA, 90 nA].

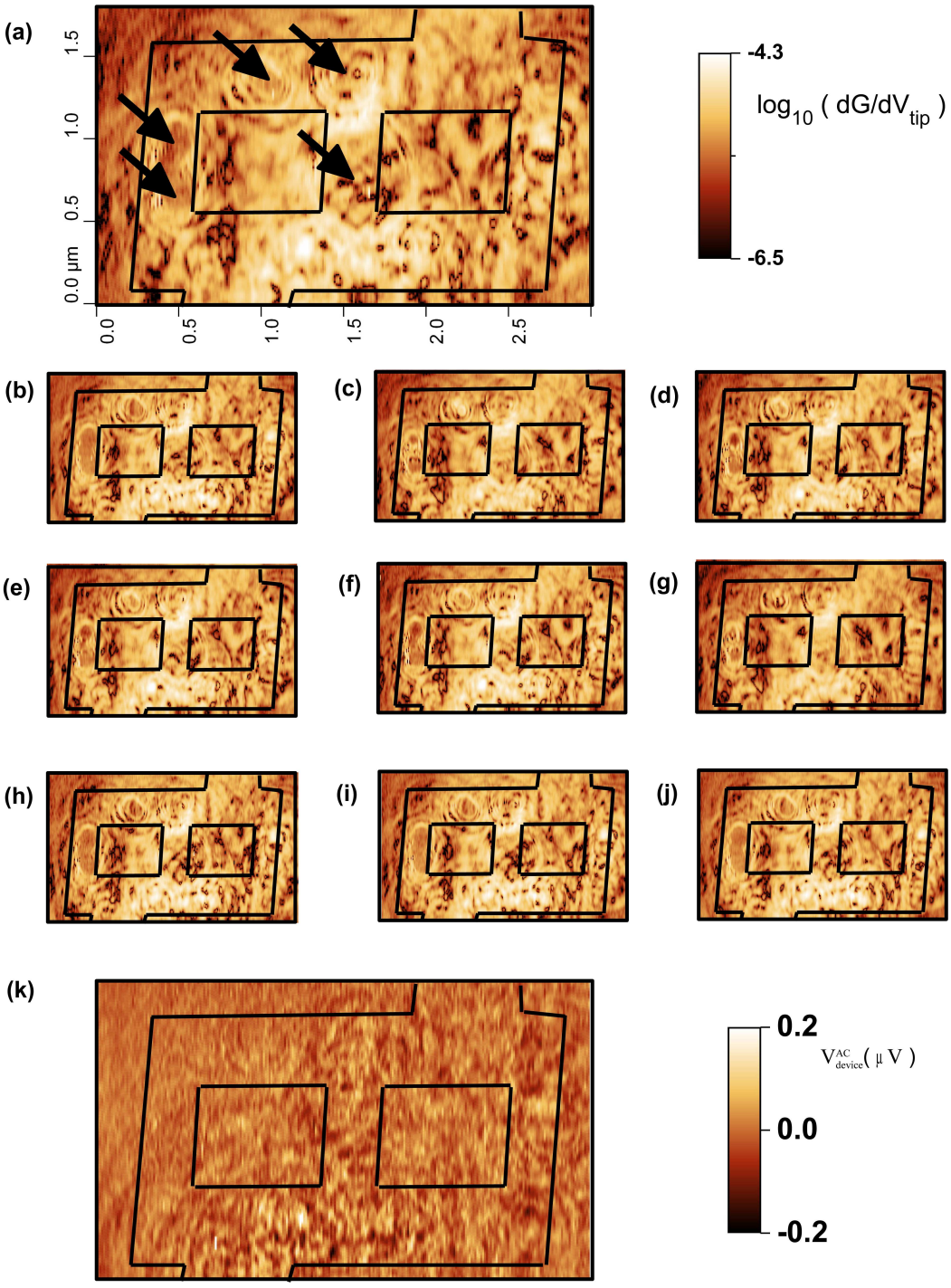

Figure 5.26: Transconductance maps obtained d_{ts} = 100nm, $V_{tip}^{DC} = -4V$, V_{tip}^{AC} = 40 mV@930 Hz. (a) I_0 = 15nA. (b)-(f) Positive currents: I_0=90nA (b) to 30nA (f); (g)-(j) Negative currents: I_0=−15nA (g) to −60nA (j), ΔI_0 =-15nA. The unit of dG/dV_{tip} is S/V, plotted in $\log_{10}$ scale. (k) $I_0 = 0$. Color bar: V_{device}^{AC} in μV.

Discussion of Figure 5.26

1. Figure 5.26 (a) shows the map obtained with $I_0 = 15$ nA. We see that there exist several traps, as indicated by arrows. For the other currents, the patterns of the transconductance maps are nearly identical. This result indicates that the measured signal V_{device} is linearly dependent on the amplitude of I_0, in other words, the transconductance is independent of I_0 in this range. The energy of electrons flowing across the device is estimated to be $\Delta E = e \cdot (90nA \times 12k\Omega) \sim 1meV$ above the Fermi energy[1]. Since 1 meV is only 3 times the thermal energy k_BT at 4.2 K, it would be interesting to investigate deeper the non-linear regime.

2. Figure 5.26 (k) measured at $I_0 = 0$ still shows a response in V_{device}, but much smaller than with $I_0 \neq 0$. The pattern is quite random, and does not reveal any interesting phenomenon.

5.3.3 Charge trap and device conductance

Dual-frequency mode with current bias

The local response of the conductance as a function of V_{tip} has been measured by means of the transconductance. However, to investigate the relation between the charge traps and the conduction of the device, it's necessary to measure the device responses to both V_{tip}^{DC} and V_{tip}^{AC} at the same time. The measurement principle is based on two AC modulations at different frequencies f_1 and f_2, one on the device current (conductance) and one on the tip voltage (transconductance). The device voltage can then be expressed as:

$$\begin{aligned} V &= I \cdot R \\ &= (I_{DC} + I_{AC,f_1}) \cdot [R_0 + \frac{dR}{dV_{tip}} \cdot (V_{tip}^{DC} + V_{tip}^{AC,f_2})] \\ &= \underbrace{I_{DC} \cdot (R_0 + \frac{dR}{dV_{tip}} \cdot V_{tip}^{DC})}_{DC} + \underbrace{I_{AC,f_1} \cdot (R_0 + \frac{dR}{dV_{tip}} \cdot V_{tip}^{DC})}_{f_1-signal} \\ &\quad + \underbrace{I_{DC} \cdot \frac{dR}{dV_{tip}} \cdot V_{tip}^{AC,f_2}}_{f_2-signal} + \underbrace{I_{AC,f_1} \cdot \frac{dR}{dV_{tip}} \cdot V_{tip}^{AC,f_2}}_{(f_1+f_2)\&(f_2-f_1)signals} \end{aligned} \tag{5.12}$$

[1]For the electron density $n_s = 3.52 \times 10^{11} cm^{-2}$, the Fermi energy is $E_F = 16.8$ meV.

The voltage difference across the device is a mixture of different frequencies: DC, f_1, f_2, $f_1 + f_2$, and $f_1 - f_2$. The conductance can be obtained from:

$$V_{AC,f_1} = I_{AC,f_1} \cdot (R_0 + \frac{dR}{dV_{\text{tip}}} \cdot V_{\text{tip}}^{DC}) \tag{5.13}$$

and the transconductance can be obtained from:

$$V_{AC,f_2} = I_{DC} \cdot \frac{dR}{dV_{\text{tip}}} \cdot V_{\text{tip}}^{AC,f_2} \tag{5.14}$$

To measure the conductance and transconductance simultaneously, the lock-in should be configured to demodulate the signal components at frequencies f_1 and f_2. This task could be done with two lock-ins, each one demodulating the signal with only one reference frequency. Thanks to the 'dual-reference' function of the Signal Recovery-7265 lock-in amplifier, this measurement is completed with one single lock-in. Figure 5.27 and 5.28 show the simultaneously measured transconductance and conductance.

Discussion of Figure 5.27 and Figure 5.28

1. In the transconductance map (Figure 5.27), the spatial distribution of traps changed a lot from the previous results. Some obvious pattern, e.g., those formed in the left arm, disappeared, while some new ones come out. This is because the device was reset by photon illumination after it got blocked by some electrostatic discharging.

2. The evolution of the ring-shaped contour in the central arm as a function of V_{tip} is identical to that observed previously. This indicates that the two lock-in measurement reveals identical information regarding the transconductance.

3. In the conductance map (Figure 5.28), larger responses are observed at the same positions as on Figure 5.27, in particular in the central arm. This can be explained by the presence of charge traps that reduce locally the conductance.

4. The statistical analysis shown in (l) indicates that the mean value of the conductance (G_{mean}) over the whole map and the standard deviation σ_G are linearly dependent on V_{tip}. This is consistent with the model discussed in Chapter 4 and Figure 5.15.

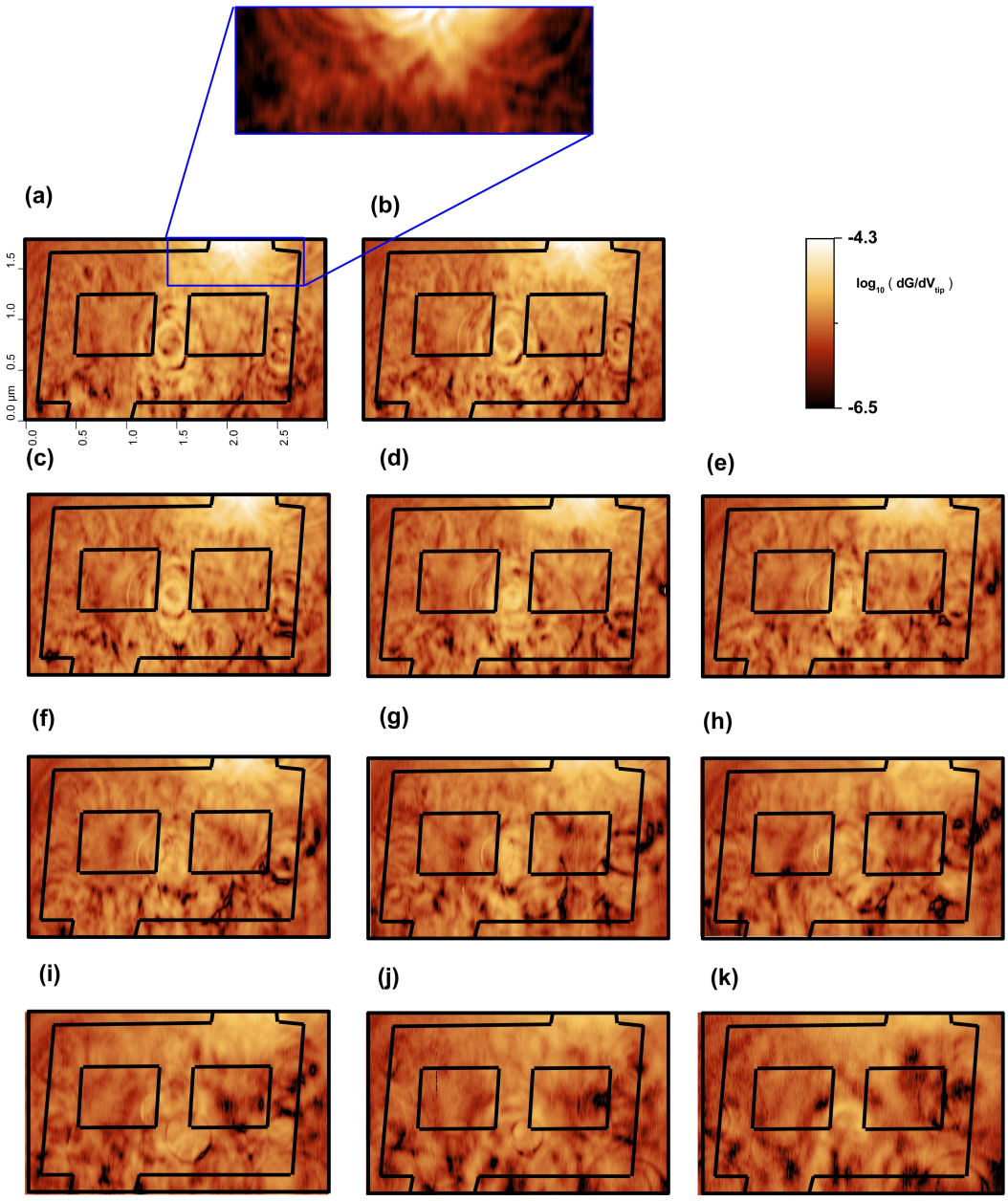

Figure 5.27: Transconductance maps obtained $d_{ts} = 100$nm, $V_{tip}^{AC} = 40$ mV@930 Hz, I = 30nA + 3nA@68 Hz. $V_{tip}^{DC} = -3.9$V(a) to -0.9V (k), increasing step ΔV_{tip}^{DC}=0.3 V. The unit of dG/dV_{tip} is S/V, plotted in $\log_{10}$ scale.

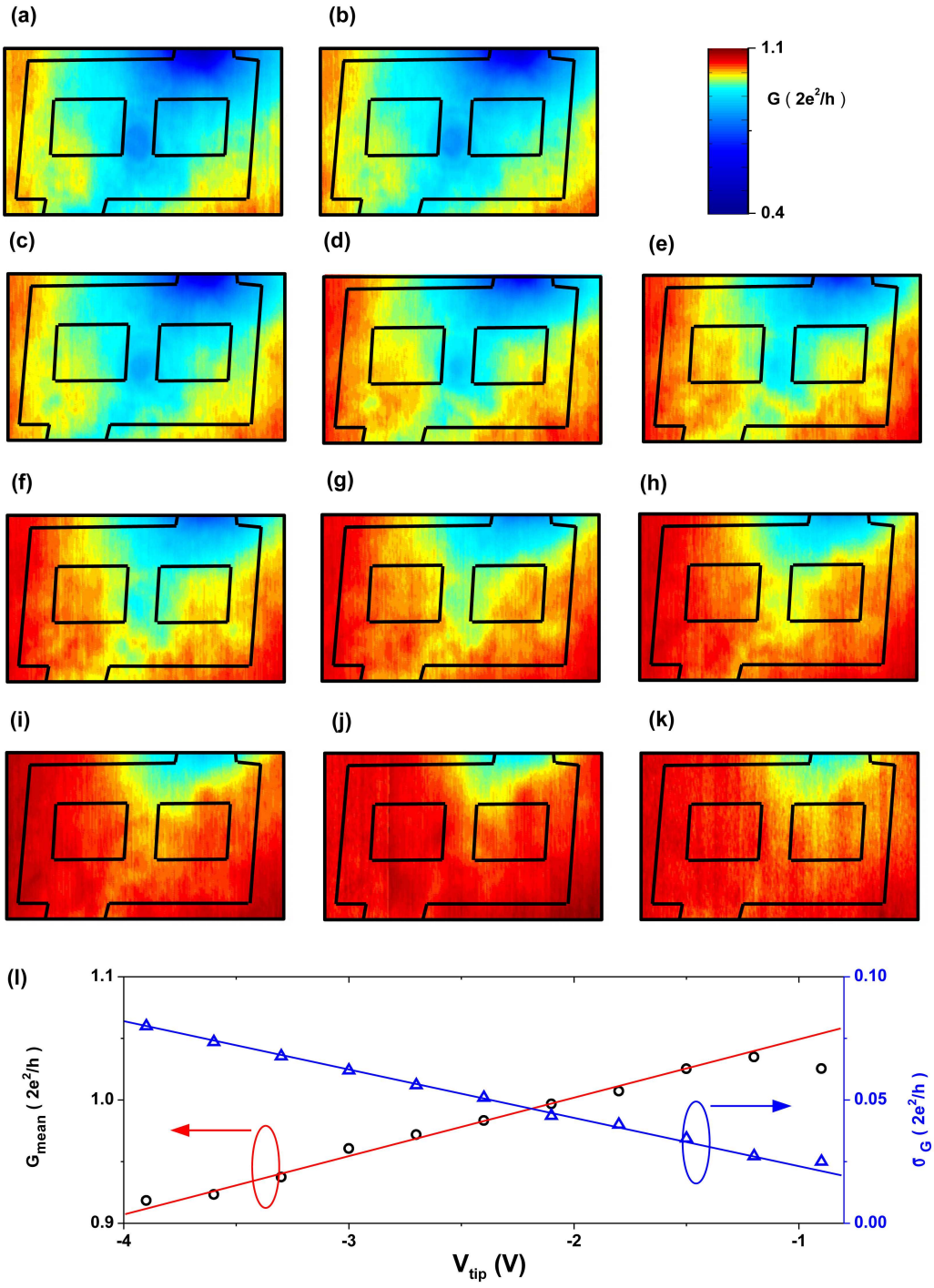

Figure 5.28: Conductance maps obtained d_{ts} = 100nm, V_{tip}^{AC} = 40 mV@930Hz, I = 30nA+3nA@68 Hz. $V_{tip}^{DC} = -3.9$V (a) to -0.9V (k), increasing step ΔV_{tip}^{DC}=0.3 V. (l) Mean value of the conductance G_{mean} and standard deviations of the conductance σ_G calculated for (a) to (k).

5. In the top opening, the tip induces a much stronger gate effect as compared to the bottom opening, i.e., the presence of the negatively biased tip decreases the conductance dramatically. In other words, the channel is partially blocked, which is not observed in the bottom opening, nor in previous results, and is probably related to the complete blocking that occurred before this measurement and the reset by illumination. It's difficult to determine the origin of the stronger gate effect that occurs in the top opening, solely from the conductance map. However, in Figure 5.27, around the top opening, several arcs can be seen clearly around the bright spot. Thus, we could suggest that charge traps are located near the top opening, and this might be the origin of the strong gate effect.

The dual-reference measurement is therefore a powerful method that yields more information than the conventional measurement of G or dG/dV_{tip} separately.

5.3.4 Charge traps at the openings

Dual-frequency mode with voltage bias

As seen from Figure 5.28, at the top opening, the negatively biased tip induces a strong gate effect on the electron channel. Thanks to this behavior, the scattering of 2DEG electrons by the charge traps can be studied in more details because the top opening is an unavoidable path for the electron flow, in contrast to the three parallel paths in previous experiment when the tip is scanned essentially over the double ring structure.

For this high impedance measurement, the current bias measurement configuration is switched to voltage bias, thus Equation 5.12 becomes:

$$\begin{aligned} I &= V \cdot G \\ &= (V_{DC} + V_{AC,f_1}) \cdot [G_0 + \frac{dG}{dV_{\text{tip}}} \cdot (V_{\text{tip}}^{DC} + V_{\text{tip}}^{AC,f_2})] \\ &= \underbrace{V_{DC} \cdot (G_0 + \frac{dG}{dV_{\text{tip}}} \cdot V_{\text{tip}}^{DC})}_{DC} + \underbrace{V_{AC,f_1} \cdot (G_0 + \frac{dG}{dV_{\text{tip}}} \cdot V_{\text{tip}}^{DC})}_{f_1-signal} \\ &\quad + \underbrace{V_{DC} \cdot \frac{dG}{dV_{\text{tip}}} \cdot V_{\text{tip}}^{AC,f_2}}_{f_2-signal} + \underbrace{V_{AC,f_1} \cdot \frac{dG}{dV_{\text{tip}}} \cdot V_{\text{tip}}^{AC,f_2}}_{(f_1+f_2)\&(f_2-f_1)signals} \end{aligned} \tag{5.15}$$

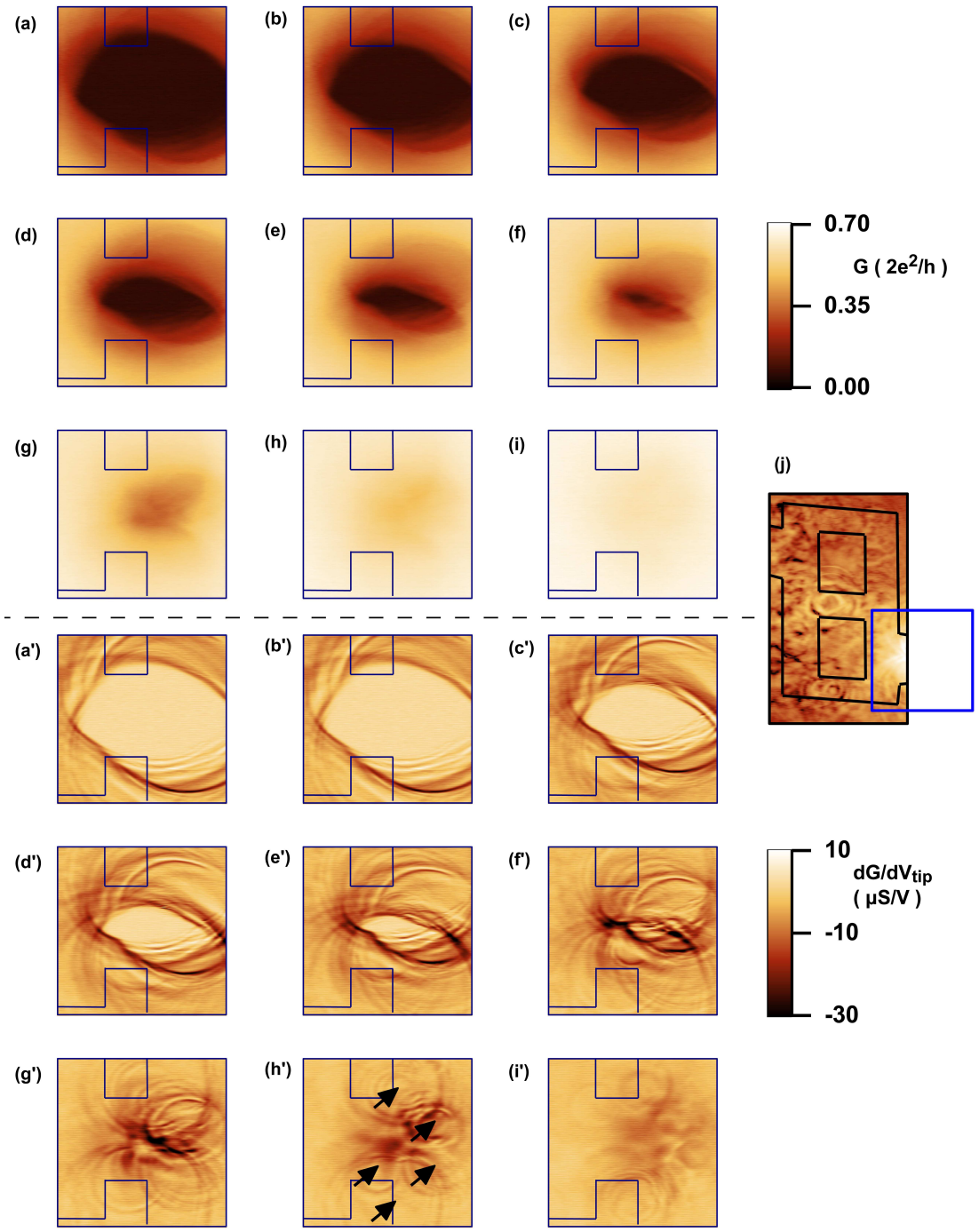

Figure 5.29: Dual frequency measurement on the top opening region as shown by the square in (j), with voltage biased configuration. d_{ts} = 100nm, V_{tip}^{AC} = 40 mV@930 Hz, V_{ds} = 1mV + 100μV@68 Hz. (a)-(i) Conductance maps, (a′)-(i′) transconductance maps, obtained with V_{tip}^{DC}=−10V (a) to −2V (i).

The simultaneously measured conductance and transconductance are given respectively by:

$$G = \frac{I_{AC,f_1}}{V_{AC,f_1}} \quad \text{with} \quad I_{AC,f_1} = V_{AC,f_1} \cdot (G_0 + \frac{dG}{dV_{\text{tip}}} \cdot V_{\text{tip}}^{DC}) \tag{5.16}$$

$$\frac{dG}{dV_{\text{tip}}} = \frac{I_{AC,f_2}}{V_{DC} \cdot V_{\text{tip}}^{AC,f_2}} \quad \text{with} \quad I_{AC,f_2} = V_{DC} \cdot \frac{dG}{dV_{\text{tip}}} \cdot V_{\text{tip}}^{AC,f_2} \tag{5.17}$$

This measurement is shown in Figure 5.29.

Discussion of Figure 5.29

1. When V_{tip} is smaller than -5 V, the channel is fully blocked when the tip is flying above the central part: in black color in (a)-(e). The size of the blocked region increases as V_{tip} becomes more negative. This effect cannot be interpreted only with the depletion of the 2DEG channel by the tip voltage, because the gate effect is much weaker around the bottom opening (Figure 5.28).

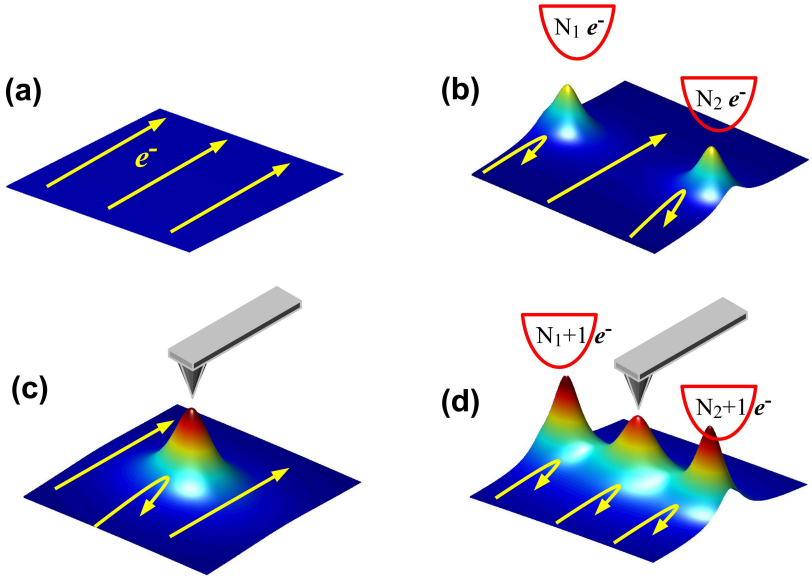

Figure 5.30: Schematics of the electron flow in the constriction studied in Figure 5.29 for different situations: (a) no charge trap nor negatively biased tip, (b) only two charge traps with N_1 (N_2) electrons, (c) only the negatively biased tip, and (d) two charge traps with one additional electrons and negatively biased tip.

2. The contours shown in (a′)-(i′) reveal the existence of multiple charge traps in the nearby region around the top opening. The number of traps is estimated around 5, as indicated by the arrows in (h′). It also appears that the boundary of the blocked region (uniform light color) follows some of the contours, as if adding an extra electron suddenly blocks the conduction. The mechanism is schematically explained in Figure 5.30. In absence of the biased tip (b), the conductance of the device is determined by the scattering potential induced by the trapped electrons; without traps (c), the tip induced potential affects the conductance like at the bottom opening; with the presences of both biased tip and trapped electrons (d), the channel is blocked by the increased negative charge in the traps as compared to (b).

3. The shapes of innermost contours that appear in the transconductance maps (a′)-(e′) are almost identical to the boundaries of the fully blocking regions (a)-(e) in black. This result is consistent with our interpretation that, when the channel is fully blocked, there is no local conductance change. The displacement of the tip within these regions still changes the number of electrons inside the traps, as well as the scattering potential, but these changes are not revealed in the transconductance measurement because the current equals to zero.

From this analysis, we conclude that the existence of charge traps affects significantly the device conductance. The influence becomes stronger as the size of device decreased (from a multiple paths device to a constriction).

5.3.5 Vertical position of charge traps

As discussed in the section on QD and Coulomb Blockade in Chapter 2, when the QD is biased with a small voltage, a conductance peak appears if the chemical potential of the N^{th} electron inside the QD is aligned with the reservoirs by tuning the gate potential ($\mu_S \approx \mu_N \approx \mu_D$). If the gate electrode is movable, like in the case of the biased tip of SGM experiments, a conductance peak would build a sphere in the 3-D space, assuming the capacitive interaction between tip and QD is isotropic. For different electron numbers inside the QD tuned by the tip potential, we therefore expect a set of concentric spherical surfaces with different radii. In the case of a 2DEG sample, only spherical caps above the surface are accessible (on the vacuum side). When the tip scans in a horizontal plane cutting these caps, concentric rings appear, which has been reported in numerous SGM experiments on different devices [18, 19, 23, 43]. When the tip

scans in a vertical plane, concentric arcs are expected to appear, as schematically shown in Figure 5.31 (a) and (b).

If the QD is replaced by a charge trap with Coulomb blockade, similar phenomena should be observed. In a SGM transconductance measurement reported in ref [97], the authors studied the events of charging/discharging occurring in traps with a QPC acting as a sensor. At the vicinity of the charge trap, concentric rings and arcs were observed in horizontal and vertical planes respectively.

In previous sections, we have analyzed in details the ring-shaped contours obtained by scanning the tip horizontally. To localize the vertical position of the charge trap, we studied the tip-height dependence of the contours by transconductance measurement. The experimental procedure is the following:

1. At the nearby region of the top opening studied in Figure 5.29, transconductance measurements are performed with a tip height of 120 nm. Again we find the concentric patterns, as shown in Figure 5.31 (c).

2. Next, we choose a single line (AB) that passes through the center of the circular contours, and lower the tip by 70 nm. The tip is now 50 nm above the surface.

3. We scan the tip along AB with different tip heights using the 'Multi-pass' module in the Nanonis controller software. 'Multi-pass' works as follow: (i) the tip is scanning along AB forth and back (pass-1) and (pass-2); (ii) after returning to the initial point (A), the tip height is increased by 1 nm; steps (i) and (ii) are looped n times (pass-$2n$), where n is a preset value to reach the maximum height. During the scanning in different passes, V_{tip} is kept constant. The recorded transconductance as a function of tip height is shown in (d). Different sets of arcs are related to different traps.

To determine the vertical position of a trap, we use the model in ref [65, 98]: the electrostatic potentials in vacuum (ϕ_v) and semiconductor (ϕ_s) regions induced by a point charge q located above a semiconductor with z_0 are:

$$\phi_v = \frac{q}{4\pi\varepsilon_0}\left[\frac{1}{\sqrt{x^2+(z_0-z)^2}} - \left(\frac{\varepsilon-1}{\varepsilon+1}\right)\frac{1}{\sqrt{x^2+(z_0+z)^2}}\right] \quad \text{for} \quad z > 0 \tag{5.18}$$

$$\phi_s = \frac{q}{4\pi\varepsilon_0}\left(\frac{2}{\varepsilon+1}\right)\frac{1}{\sqrt{x^2+(z_0-z)^2}} \quad \text{for} \quad z < 0 \tag{5.19}$$

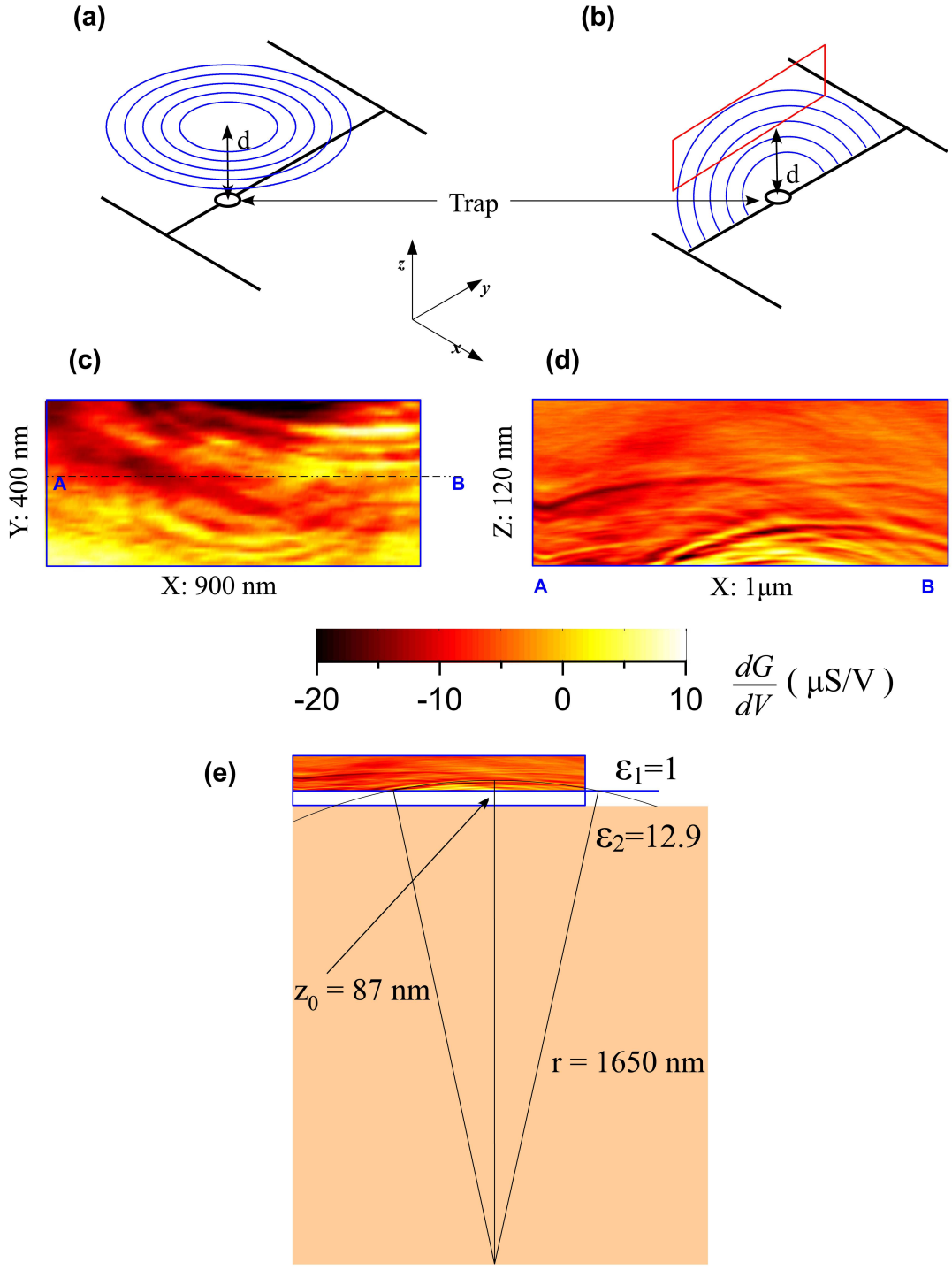

Figure 5.31: Schematics of tip scans above a charge trap in (a) horizontal plane, (b) vertical plane. Transconductance measurements obtained by scanning the tip in (c) horizontal plane with d_{ts} = 120nm, and (d) vertical plane along AB with d_{ts} = 50 to 170nm. (e) The fitted result of one of the arcs appeared in transconductance map of (d).

where x is the horizontal distance from q. From Equation 5.19 we know that when q is moving along a sphere cap with radius $r = \sqrt{x^2 + (z_0 - z)^2}$ centered at (0, z), ϕ_s is constant at the center. The vertical position of the charge trap (z) can be determined by fitting one of the iso-conductance (iso-potential) lines shown in Figure 5.31 (d).

For a typical arc we found $r = 1650$ nm. This would indicate that the trap is located 1.5 μm below the 2DEG plane, which locates 42 nm below the surface. This result is surprising because the electrical field should be screened by the 2DEG and should not induce charge states change in the traps. In this model, the effects of the doped capping layer, Si-dopants and 2DEG are not taken into account. To localize the trap vertical position precisely, a more accurate model describing the tip-trap electrostatic interaction should be developed instead of the basic one used here.

Chapter 6

Conclusions

6.1 Summary

In this thesis, we have studied the electron transport in nano-devices by the technique of scanning gate microscopy. The nano-devices have been fabricated from InGaAs/InAlAs heterostructures containing a high mobility 2DEG a few tens of nanometers below the surface. The microscope is a cryogenic AFM employing a quartz tuning fork as the force sensor, connected to a metallic tip used as a movable gate, to locally modulate the electron transport.

First, we have updated the force detection mode of the existing AFM system from traditional optical method to force sensing by a TF. The tip-sample force interaction induces a shift on the resonance frequency of the TF sensor that is tracked by means of phase-lock loop. The properties of self-actuating and self-sensing of the TF sensor simplify the experimental apparatus and the manipulations. We have demonstrated that, working with TF sensor, we avoid the problems of charge rearrangement by optical excitation.

Then, we have investigated the tip-sample interaction, in the two aspects of capacitive force and gate effect, using a constriction in the 2DEG. We have shown that the capacitor model taking into accounts both the sphere-shape of the tip apex and the dielectric property of the semiconductors materials describes well the capacitive force interaction. From the SGM measurement where the biased tip acts as a scanning gate for the electron transport, we found that the spatial distribution of the tip induced electrostatic potential in the 2DEG plane can be described by a Lorentzian function. We extracted the extension of the potential from the full with at half maximum of such distribution, and proposed a model

to describe the gate effect of the tip.

In the work on Coulomb blockade in a QD, we fabricated the device by dry etching of the heterostructure. We characterized the QD by electron transport measurement, and extracted the capacitances of the drain, source and two lateral gates as well as the charging energy of the QD. From the SGM measurement results, we verified the model describing the spatial distribution of the tip induced potential proposed in the section on SGM operation.

In the work on Braess paradox, according to the numerical simulations of quantum transport in a Braess paradox nano-device, the presence of a third channel results in a current drop under certain circumstance, which is a counter-intuitive behavior of mesoscopic systems in analogy with the Braess paradox in classical networks. We performed SGM experiments to modulate the channel widths of a double ring 'paradox device', and confirmed the occurrence of the paradox effect by both point spectroscopy measurement and mapping of the conductance variation as a function of the tip voltage and position.

In the work on charge traps, we discovered several individual traps in the SGM images of conductance variations by removing the global gate response. Following, the traps have been directly imaged by transconductance measurements. We proposed a model describing the conductance change with the presence of charge traps: as the negatively biased tip approaches the trap, the trap is suddenly getting charged by a single electron when the chemical potential of the trap reaches the Fermi level; the charged trap increases the local scattering potential, resulting in a sudden decrease of the conductance. This single electron charging results from Coulomb blockade in the trap and appears as concentric circles in SGM images. We determined the in-plane positions of the traps and explored the vertical position of the traps by scanning the tip at different heights and plotting the iso-potential lines. We revealed the relation between the device conductance and the traps charging effect from the conductance and transconductance measurements performed simultaneously by employing the dual-frequency technique.

6.2 Perspectives

On the present work:

- Our investigation of Coulomb blockade in QD should be continued as it provides a good test experiment to map the tip induced potential. For this purpose, the sample fabrication should be improved to obtain a clean sample surface (no re-deposition) and a large charging energy (small dot).

- The Braess paradox effect should be further investigated to clarify the microscopic origin of the effect, and the influence of the sample history.

- The imaging and spectroscopy of charge traps in 2DEG or nanowires is the subject of a new research project submitted to the 'Agence Nationale de la Recherche' (ANR).

On new project:

The investigation of electron-electron interaction in low density QPC will be studied by SGM in the frame of a starting ANR project called ITEM-Exp. This study will focus on the 0.7 G_0 anomaly and analyze the electron flow for the two spin states of the electrons split by the Zeeman energy under a parallel magnetic field.

On emerging fields:

In addition to the traditional III-V semiconductor 2DEG sample, recently some emerging materials systems draw a lot of attention in both academic and industrial fields, including graphene and topological insulator. The low electron density in these 2D electron systems makes them suitable candidates for the studies by SGM to explore the local electronic properties.

1. Graphene is a flat monolayer of carbon atoms tightly packed into a two-dimensional honeycomb lattice [99]. As an ideal 2D electron system, fruitful physics are to be explored therein by SGM. In ref [20], the authors reported their study of QD in graphene by SGM. In ref [100], conductance quantization is reported in a suspended graphene sheet. An interesting experiment could be the imaging of the edge state in the quantum Hall effect by scattering back the 1D electron channel in a nano-scale Hall bar.

2. Topological insulators are electronic materials that have a bulk band gap like an ordinary insulator but have protected conducting states at their edge or surface [101]. In ref [102], the authors reported the study of the quantum spin hall (QSH) state on a topological insulator surface by SGM. Undoubtedly, SGM will play an important role to study the electron transport on the topological insulator surface.

On SGM technique:

On the experimental side, the SGM technique could be further developed by combining the present gating functionality with a force sensing capability. This would be particularly interesting for the single electron charging investigations, either in lithographically designed QD or in structural defects acting as charge traps in semiconductor heterostructures.

Appendix A

Introduction (en français)

A.1 Dispositifs électroniques

En 1947, John Bardeen, Walter Brattain et William Shockley de Bell Labs ont développé le premier transistor à base de germanium. Le premier transistor en silicium a été produit par Texas Instruments en 1954, c'est alors que les technologies silicium ont commencé. En parallèle à l'avancement technologique, la recherche fondamentale sur les semi-conducteurs s'est également développée rapidement. Dès lors, la science et la technologie ont profité l'une de l'autre. Grâce à l'invention du transistor à effet de champ, la recherche fondamentale sur les systèmes d'électrons bidimensionnel (2DES) est devenue possible à partir des années 1960, initialement basée sur des semi-conducteurs à un élément comme le silicium [1], puis plus tard sur des semi-conducteurs composés III-V comme l'arséniure de gallium (GaAs) [2] et II-VI comme le tellurure de cadmium (CdTe) [3], et plus récemment sur le graphène [4] et sur des oxydes [5]. Outre l'intérêt pour l'industrie de la microélectronique, les systèmes à deux dimensions ont ouvert un nouveau domaine de recherche, où les effets Hall quantiques entiers et fractionnaires ont été observés et ont conduit à deux prix Nobel en 1985 [6] et 1998 [7].

Aujourd'hui, les propriétés électroniques des 2DES sont encore un domaine important de la recherche fondamentale, dans laquelle une grande partie du travail est basée sur des mesures de transport électronique à l'aide d'électrodes macroscopiques. Les mesures de transport sont un outil puissant qui a fourni un éclairage précieux sur les propriétés électroniques des 2DES. Cependant, ils ne sont pas adaptés pour étudier les propriétés locales de ces systèmes, car ils ne fournissent pas d'information spatiale. Afin d'étudier les propriétés électroniques

locales des 2DES plus en détail, les chercheurs ont introduit des techniques spécifiques à base de sondes à balayage.

A.2 Sondes locales à balayage

Depuis l'invention du microscope à effet tunnel (STM) en 1981 [8, 9], la famille des microscopies à sonde locale s'est élargie à la microscopie à force atomique (AFM) [10] (contact, non-contact, friction), la microscopie à force électrostatique (EFM), la microscopie à force magnétique (MFM), la microscopie en champ proche optique (SNOM) [11], la microscopie de capacitance à balayage (SCM) [12], etc.

Différente de la microscopie optique traditionnelle, les microscopies à balayage à sondes locales (SPM) utilisent des sondes matérielles pour étudier l'interaction sonde-échantillon et d'obtenir une carte spatiale des propriétés de l'échantillon. Ainsi, la résolution spatiale n'est pas limitée par la diffraction de la lumière, et peut atteindre une résolution sub-nanométrique.

Peu de temps après l'invention des SPM, les chercheurs ont réalisé que, avec ces outils puissants, non seulement les propriétés des échantillons pouvaient être obtenues à partir des mesures (par exemple, l'extraction de la densité d'état électronique à partir du courant tunnel en STM, ou l'aimantation en MFM), mais aussi la modification nanométrique des échantillons était devenue possible, par exemple, le déplacement des atomes par STM [13], la nano-lithographie par AFM [14], etc

A.3 Microscopie à balayage de grille (SGM)

La microscopie SGM a été développée à la fin des années 1990 pour résoudre la limitation du STM qui ne fonctionne pas sur les dispositifs semi-conducteurs basés sur des 2DES enterrés dans des hétérostructures [15]. La SGM utilise la technique AFM, mais la pointe métallique est utilisée comme une électrode de grille mobile couplée capacitivement au dispositif, et les propriétés de transport électronique sont mesurées en fonction de l'influence de cette grille à l'échelle nanométrique.

Lors d'une mesure SGM, la conductance dans le plan du 2DES est mesurée pendant le balayage de la pointe au-dessus du dispositif. La pointe agit comme une électrode qui contrôle le comportement du dispositif. De ce point de vue, la

SGM est différente de la plupart des types de SPM, où la pointe joue uniquement le rôle d'un capteur, comme en STM, EFM, SCM, etc. De manière générale, la SGM est la combinaison d'un nano-dispositif présentant un effet de grille et d'un microscope à sonde à balayage où la pointe est utilisée comme une nano-grille volante.

Les dispositifs qui sont étudiés par SGM peuvent être fait de semi-conducteurs 2D [16, 17], nanofils [18], nanotubes [19], graphène [20, 21, 22], supraconducteurs [23]. Les dispositifs peuvent être des 2DES en forme de boite quantique (QD) [18, 19], de contact ponctuel quantique (QPC) [16, 24], d'anneau quantique [25, 26], de barre de Hall [27, 28], etc.

Les SPM utilisés dans les études SGM sont essentiellement des AFM avec des pointes conductrices mais les capteurs de force peuvent être variés. Une spécificité importante est que le microscope doit être adapté aux basses températures (en dessous de 4,2 K) parce que les phénomènes quantiques sont les motivations principales de ces études, et au champ magnétique si des effets de magnétoconductance sont attendus, comme par exemple, l'effet Aharonov-Bohm [25], l'effet Hall quantique [27, 28], la transition supraconductrice [23] et les phénomènes de focalisation magnétique [24].

Le principe de fonctionnement de la SGM est décrit schématiquement sur la figure 1.1. La pointe polarisée à la tension Vtip est scannée dans le plan parallèle à la surface du dispositif avec une distance fixe, et la conductance G du dispositif est enregistrée simultanément afin de construire une carte de changement de conductance (ou d'effet de grille local) en fonction de la position de pointe (c'est-à-dire une image SGM). Cette carte peut être enregistrée pour des tensions de pointe différentes, ou une autre alternative est d'enregistrer des spectroscopies locales de changement de conductance en fonction de la tension de pointe pour diverses positions de la pointe.

A.4 Description du contenu

Dans cette thèse, je présente les différents éléments intervenant dans la SGM, y compris les dispositifs, l'instrumentation, le protocole expérimental, les problèmes rencontrés, les solutions, et les résultats obtenus sur différents dispositifs.

Dans le chapitre 2, je décris les propriétés physiques d'un gaz d'électrons bidimensionnel (2DEG) formé à l'interface d'une hétérostructure de semiconducteurs

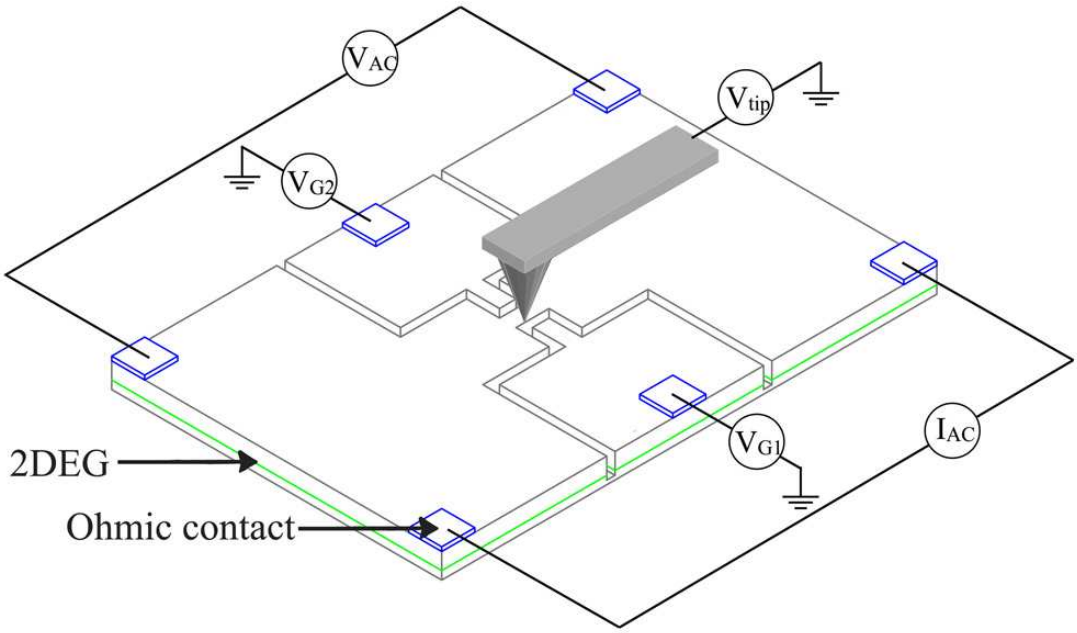

Figure A.1: Schéma du principe de fonctionnement de la microscopie à balayage de grille (SGM). Dans la configuration standard de mesure de conductance à 4 contacts, le dispositif est polarisé par un courant alternatif IAC, et la différence de tension aux bornes du dispositif VAC est détectée par une détection synchrone (lock-in). La conductance du dispositif peut être modulée en modifiant les tensions de grille latérale VG1 et VG2, ou la tension de pointe Vtip. Lorsque la pointe polarisée est scannée dans un plan au-dessus du dispositif, une carte de changement de conductance est construite en fonction de la position de la pointe.

III-V, et présente quelques phénomènes de transport électronique mésoscopique (quantification de la conductance d'un QPC, blocage de Coulomb dans un QD, et effet Aharonov-Bohm) ainsi que leur étude par des expériences de SGM.

Dans le chapitre 3, je discute le microscope utilisé dans ce travail, y compris une description détaillée du capteur de force à base de diapason (TF) à quartz (modèles mécaniques et électriques, préparation de la sonde avec pointe AFM, détection de force), une présentation de la structure du microscope, le système de contrôle (logiciel) et le fonctionnement en mode AFM pour la topographie à température ambiante et à basse température.

Dans le chapitre 4, je discute de la préparation des échantillons (dans les deux salles blanches de Louvain-la-Neuve et Grenoble), le système électronique de mesure du transport, le fonctionnement du microscope en mode SGM, une expérience simple de SGM sur une constriction (pour illustrer le couplage capacitif entre la pointe et le dispositif, et extraire la perturbation de potentiel vu par les électrons), et enfin une expérience préliminaire de SGM sur une cavité elliptique mésoscopique.

Au chapitre 5, je présente les résultats de trois expériences SGM réalisées dans ma période de thèse: (i) blocage de Coulomb sur une boite quantique contrôlée par des grilles latérales, (ii) phénomène de paradoxe de Braess dans une nanostructure en double anneau et (iii) imagerie des pièges de charge couplés au 2DEG de l'hétérostructure de semi-conducteurs III-V.

Dans le chapitre 6, j'expose les conclusions et les perspectives possible pour poursuivre et étendre ce travail dans l'avenir.

A. INTRODUCTION (EN FRANÇAIS)

Appendix B

Conclusion et perspectives (en français)

B.1 Résumé

Dans cette thèse, nous avons étudié le transport électronique dans des nanodispositifs par la technique de microscopie à effet de grille local. Les nanodispositifs ont été fabriqués à partir d'hétérostructures de InGaAs / InAlAs contenant un 2DEG de grande mobilité à quelques dizaines de nanomètres sous la surface. Le microscope AFM cryogénique utilise un diapason à quartz comme capteur de force, connecté à une pointe métallique utilisée comme une grille mobile, afin de moduler le transport des électrons.

Premièrement, nous avons modifié le mode de détection de force du précédent système AFM (utilisant une méthode optique traditionnelle) pour utiliser un diapason à quartz (TF). L'interaction pointe-échantillon induit un décalage de la fréquence de résonance de la sonde qui est suivi par une boucle à verrouillage de phase (PLL). Les propriétés d'auto-actionnement et d'auto-détection du TF simplifie le dispositif expérimental et les manipulations. En travaillant avec ce capteur, nous évitons les problèmes de création ou réarrangement de charges par excitation optique.

Ensuite, nous avons étudié l'interaction pointe-échantillon, aussi bien du point de vue de la force et que de l'effet capacitif, en utilisant une constriction gravée dans le 2DEG. Nous avons montré que le modèle de condensateur (avec une forme sphérique de l'apex de la pointe et incluant les propriétés diélectriques des

matériaux semi-conducteurs) décrit bien l'interaction capacitive. En balayant la pointe polarisée comme une grille pour le transport d'électrons, nous avons constaté que la distribution spatiale du potentiel électrostatique induit par la pointe dans le plan du 2DEG peut être décrite par une fonction lorentzienne. Nous avons extrait l'extension du potentiel à partir de la largeur à mi-hauteur de cette distribution, et proposé un modèle pour décrire l'effet de grille de la pointe.

Dans le travail sur le blocage de Coulomb dans un QD, nous avons fabriqué le dispositif par gravure sèche (RIE) de l'hétérostructure. Nous avons caractérisé le QD par des mesures de transport électronique, pour extraire les capacités des électrodes source, drain, et deux grilles latérales, ainsi que l'énergie de charge du QD. A partir des résultats de mesure SGM, nous avons vérifié le modèle décrivant la distribution spatiale du potentiel induit par la pointe (proposé dans la section précédente).

Dans le travail sur le paradoxe de Braess, selon les simulations numériques du transport quantique dans un nano-dispositif en forme de réseau à plusieurs branches, la présence d'une troisième branche induit (dans certaines conditions) une chute de courant qui est un comportement contre-intuitif, analogue au paradoxe de Braess dans les réseaux classiques. Nous avons effectué des expériences de SGM pour moduler la largeur du canal central de tels dispositifs en forme de double anneau, et confirmé l'apparition de l'effet paradoxal à la fois par des mesures de spectroscopie ponctuelle et par la cartographie de la variation de la conductance en fonction de la tension de pointe et de sa position.

Dans le travail sur les pièges de charge, nous avons découvert plusieurs pièges individuels dans les images des variations de conductance SGM en supprimant l'effet de grille global. Ensuite, les pièges ont été directement imagés par des mesures de transconductance. Nous avons proposé un modèle décrivant le changement de conductance en présence de pièges de charge. Lorsque la pointe polarisée négativement s'approche du piège, celui-ci est soudainement chargé avec un électron supplémentaire lorsque le potentiel chimique du piège atteint le niveau de Fermi, et l'augmentation de charge du piège augmente le potentiel de diffusion locale dans le 2DEG, résultant en une diminution soudaine de la conductance. Cet effet de charge discret avec un seul électron à la fois résulte du blocage de Coulomb dans le piège et apparait comme des cercles concentriques dans les images SGM. Nous avons déterminé la position des pièges dans le plan horizontal et exploré leur position verticale par balayage de la pointe à différentes hauteurs et tracé des lignes isopotentiel. Nous avons analysé la relation entre la conductance

globale du dispositif et le chargement des pièges grâce à des mesures simultanées de la conductance et de la transconductance en employant une technique à deux fréquences.

B.2 Perspectives

Sur le travail actuel:

- Notre travail sur le blocage de Coulomb dans le QD doit être poursuivi car il offre une expérience de test intéressante pour cartographier le potentiel induit par la pointe. A cette fin, la fabrication de l'échantillon doit être améliorée pour obtenir une surface de l'échantillon propre (pas de re-dépôt) et une énergie de charge élevée (petite boite quantique).
- L'effet paradoxal de type Braess doit être approfondi pour clarifier l'origine microscopique de l'effet, et l'influence de l'histoire de l'échantillon.
- L'imagerie et la spectroscopie des pièges de charge dans les 2DEG ou les nanofils est l'objet d'un nouveau projet de recherche qui a été soumis à l'Agence Nationale de la Recherche (ANR).

Nouveau projet qui débute:

L'étude des interactions électron-électron dans les QPC de faible densité seront étudiés par SGM dans le cadre d'un projet ANR appelé ITEM-Exp. Cette étude se concentrera sur l'anomalie à 0,7 quantum de conductance et sur les effets de spin en séparant les énergies des électrons par effet Zeeman sous un champ magnétique parallèle.

Sur les domaines émergents:

En plus des échantillons traditionnels à base de semiconducteurs III-V, de nouvelles classes de matériaux 2DEG attirent beaucoup l'attention dans les domaines académiques et industriels, comme le graphène et les isolants topologiques. La faible densité d'électrons dans ces systèmes 2D en fait des candidats appropriés pour les études par SGM pour explorer leurs propriétés électroniques locales.

1. Le graphène est une monocouche d'atomes de carbone dans un réseau bidimensionnel en nid d'abeille [99]. Dans ce système d'électrons 2D idéal, des

effets fondamentaux pourraient être explorée par SGM. En ref [20], les auteurs ont rapporté une étude de QD dans le graphène par SGM. En ref [100], la quantification de la conductance est rapportée dans une feuille de graphène suspendu. Une expérience intéressante pourrait être l'imagerie des états de bord dans l'effet Hall quantique par rétrodiffusion des électrons de ces canaux 1D dans une barre de Hall de taille nanométrique.

2. Les isolants topologiques sont des matériaux électroniques qui ont une bande interdite en volume comme un isolant ordinaire, mais ont des états conducteurs protégés à leur bord ou à la surface [101]. En ref [102], les auteurs ont rapporté une étude de l'effet Hall quantique de spin (QSH) sur une surface d'isolant topologique par SGM. Sans aucun doute, la SGM va jouer un rôle important pour étudier le transport des électrons sur la surface des isolants topologiques.

Sur la technique SGM:

Sur le plan instrumental, la technique SGM pourrait être développée en combinant la fonctionnalité d'effet de grille actuel avec une fonctionnalité de détection de force. Cela serait particulièrement intéressant pour les études d'effet de charge à un seul électron, que ce soit dans les boites quantiques fabriquées par lithographie, ou dans les défauts structurels agissant comme pièges de charge dans les hétérostructures de semi-conducteurs.

Bibliography

[1] Dawon Kahng. Electric field controlled semiconductor device. *US Patent*, **No. 3,120,230**.

[2] Tsuneya Ando, Alan B. Fowler, and Frank Stern. Electronic properties of two-dimensional systems. *Rev. Mod. Phys.*, **54**:437–672, 1982.

[3] Sweeney T. Cox R. T. Phelps, C. and H. L. Wang. Ultrafast coherent electron spin flip in a modulation-doped cdte quantum well. *Physical Review Letters*, **102**(23), 2009.

[4] Jiang Z. Zhang Y. Morozov S. V. Stormer H. L. Zeitler-U. Maan J. C. Boebinger G. S. Kim P. Novoselov, K. S. and A. K. Geim. Room-temperature quantum hall effect in graphene. *Science*, **315**(5817):1379–1379, 2007.

[5] A. Ohtomo and H. Y. Hwang. A high-mobility electron gas at the laalo3/srtio3 heterointerface. *Nature*, **427**(6973):423–426, 2004.

[6] Dorda G. Vonklitzing, K. and M. Pepper. New method for high-accuracy determination of the fine-structure constant based on quantized hall resistance. *Physical Review Letters*, **45**(6):494–497, 1980.

[7] H. L. Stormer. Nobel lecture: The fractional quantum hall effect. *Reviews of Modern Physics*, **71**(4):875–889, 1999.

[8] G. Binnig and H. Rohrer. Scanning tunneling microscopy. *Helvetica Physica Acta*, **55**(6):726–735, 1982.

[9] G. Binnig and H. Rohrer. Scanning tunneling microscopy - from birth to adolescence. *Reviews of Modern Physics*, **59**(3):615–625, 1987.

[10] F. J. Giessibl. Advances in atomic force microscopy. *Reviews of Modern Physics*, **75**(3):949–983, 2003.

[11] Isaacson M. Harootunian A. Lewis, A. and A. Muray. Development of a 500-a spatial-resolution light-microscope .1. light is efficiently transmitted through gamma-16 diameter apertures. *Ultramicroscopy*, **13**(3):227–231, 1984.

[12] S. Lanyi and M. Hruskovic. The resolution limit of scanning capacitance microscopes. *Journal of Physics D-Applied Physics*, **36**(5):598–602, 2003.

[13] D. M. Eigler and E. K. Schweizer. Positioning single atoms with a scanning tunneling microscope. *Nature*, **344**(6266):524–526, 1990.

[14] Zhu J. Xu F. Hong S. H. Piner, R. D. and C. A. Mirkin. "dip-pen" nanolithography. *Science*, **283**(5402):661–663, 1999.

[15] Beck R. G. Topinka M. Katine J. A. Westervelt R. M. Campman K. L. Eriksson, M. A. and A. C. Gossard. Cryogenic scanning probe characterization of semiconductor nanostructures. *Applied Physics Letters*, **69**(5):671–673, 1996.

[16] LeRoy B. J. Westervelt R. M. Shaw S. E. J. Fleischmann R. Heller E. J. Maranowski K. D. Topinka, M. A. and A. C. Gossard. Coherent branched flow in a two-dimensional electron gas. *Nature*, **410**(6825):183–186, 2001.

[17] LeRoy B. J. Shaw S. E. J. Heller E. J. Westervelt R. M. Maranowski K. D. Topinka, M. A. and A. C. Cossard. Imaging coherent electron flow from a quantum point contact. *Science*, **289**(5488):2323–2326, 2000.

[18] Zwanenburg F. A. Westervelt R. M. Roest A. L. Bakkers Epam Bleszynski, A. C. and L. P. Kouwenhoven. Scanned probe imaging of quantum dots inside inas nanowires. *Nano Letters*, **7**(9):2559–2562, 2007.

[19] M. T. Woodside and P. L. McEuen. Scanned probe imaging of single-electron charge states in nanotube quantum dots. *Science*, **296**:1098–1101, 2002.

[20] Guttinger J. Huefner M. Stampfer C. Ensslin K. Schnez, S. and T. Ihn. Imaging localized states in graphene nanostructures. *Physical Review B*, **82**:165445, 2010.

[21] Borunda M. F. Heller E. J. Berezovsky, J. and R. M. Westervelt. Imaging coherent transport in graphene (part i): mapping universal conductance fluctuations. *Nanotechnology*, **21**(27), 2010.

[22] J. Berezovsky and R. M. Westervelt. Imaging coherent transport in graphene (part ii): probing weak localization. *Nanotechnology*, **21**(27), 2010.

[23] May C. Kicin S. Ensslin K. Ihn T. Hilke M. Suter K. de Rooij N. F. Huefner, M. and U. Staufer. Scanning gate microscopy measurements on a superconducting single-electron transistor. *Physical Review B*, **79**(13), 2009.

[24] Parrott R. E. Kramer T. Heller E. J. Westervelt R. M. Hanson M. P. Aidala, K. E. and A. C. Gossard. Imaging magnetic focusing of coherent electron waves. *Nature Physics*, **3**(7):464–468, 2007.

[25] Martins F. Ouisse T. Sellier H. Bollaert S. Wallart X. Cappy A. Chevrier J. Bayot V. Hackens, B. and S. Huant. Imaging and controlling electron transport inside a quantum ring. *Nature Physics*, **2**(12):826–830, 2006.

[26] Hackens B. Pala M. G. Ouisse T. Sellier H. Wallart X. Bollaert S. Cappy A. Chevrier J. Bayot V. Martins, F. and S. Huant. Imaging electron wave functions inside open quantum rings. *Physical Review Letters*, **99**(13), 2007.

[27] Ihn T. Ensslin K. Papp G. Peeters F. Maranowski K. Baumgartner, A. and A. C. Gossard. Classical hall effect in scanning gate experiments. *Physical Review B*, **74**:165426, 2006.

[28] Ihn T. Ensslin K. Maranowski K. Baumgartner, A. and A. C. Gossard. Quantum hall effect transition in scanning gate experiments. *Physical Review B*, **76**:085316, 2007.

[29] M. Tischler, B. Parker, P. Mooney, and M. Goorsky. Effect of structural parameters on ingaas/inalas 2deg transport characteristics. *Journal of Electronic Materials*, **20**:1053–1057, 1991.

[30] Aimin M. Song, Pär Omling, Lars Samuelson, Werner Seifert, Ivan Shorubalko, and Herbert Zirath. Operation of ingaas/inp-based ballistic rectifiers at room temperature and frequencies up to 50 ghz.

Japanese Journal of Applied Physics, **40**(Part 2, No. 9A/B):L909–L911, 2001.

[31] Supriyo Datta. Electronic transport in mesoscopic systems. 1997.

[32] L. M. Lifshitz L. D. Landau. Quantum mechanics non-relativistic theory. *Butterworth-Heinemann*, **3rd edition**, 1981.

[33] H. L. Stormer, L. N. Pfeiffer, K. W. Baldwin, and K. W. West. Observation of a bloch-grüneisen regime in two-dimensional electron transport. *Phys. Rev. B*, **41**(2):1278–1281, 1990.

[34] Pallab Bhattacharya. Properties of lattice-matched and strained indium gallium arsenide. *Institution of Engineering and Technology*, 1993.

[35] Vanhouten H. Beenakker C. W. J. Williamson J. G. Kouwenhoven L. P. Vandermarel D. Vanwees, B. J. and C. T. Foxon. Quantized conductance of point contacts in a two-dimensional electron-gas. *Physical Review Letters*, **60**(9):848–850, 1988.

[36] Thornton T. J. Newbury R. Pepper M. Ahmed H. Frost J. E. F. Hasko D. G. Peacock D. C. Ritchie D. A. Wharam, D. A. and G. A. C. Jones. One-dimensional transport and the quantization of the ballistic resistance. *Journal of Physics C-Solid State Physics*, **21**(8):L209–L214, 1988.

[37] H. vanHouten and C. Beenakker. Quantum point contacts. *Physics Today*, **49**(7):22–27, 1996.

[38] Szewc W. Tomsovic S. Jalabert, R. A. and D. Weinmann. What is measured in the scanning gate microscopy of a quantum point contact? *Physical Review Letters*, **105**(16), 2010.

[39] Lynch H. J. Goldhaber-Gordon D. Kouwenhoven L. P. Marcus C. M. Hirose K. Wingreen N. S. Cronenwett, S. M. and V. Umansky. Low-temperature fate of the 0.7 structure in a point contact: A kondo-like correlated state in an open system. *Physical Review Letters*, **88**(22), 2002.

[40] Austing D. G. Honda T. vanderHage R. J. Tarucha, S. and L. P. Kouwenhoven. Shell filling and spin effects in a few electron quantum dot. *Physical Review Letters*, **77**(17):3613–3616, 1996.

[41] Paul L. McEuen Seigo Tarucha Robert M. Westervelt Leo P. Kouwenhoven, Charles M. Marcus and Ned S. Wingreen. electron transport in quantum dots. *Kluwer*, 1997.

[42] Thomas Ihn. Electronic quantum transport in mesoscopic semiconductor structures. *Springer Tracts in Modern Physics*, **192**, 2004.

[43] Bleszynski A. C. Westervelt R. M. Huang J. Walls J. D. Heller E. J. Hanson M. Fallahi, P. and A. C. Gossard. Imaging a single-electron quantum dot. *Nano Letters*, **5**(2):223–226, 2005.

[44] Ihn T. Sigrist M. Ensslin K. Driscoll D. C. Gildemeister, A. E. and A. C. Gossard. Lever arm of a metallic tip in scanning gate experiments. *Physica E-Low-Dimensional Systems and Nanostructures*, **40**(5):1640–1641, 2008.

[45] Y. Aharonov and D. Bohm. Significance of electromagnetic potentials in the quantum theory. *Physical Review*, **115**(3):485–491, 1959.

[46] Matsuda T. Kawasaki T. Endo J. Tonomura A. Yano S. Osakabe, N. and H. Yamada. Experimental confirmation of aharonov-bohm effect using a toroidal magnetic-field confined by a superconductor. *Physical Review A*, **34**(2):815–822, 1986.

[47] Devoret M. H. Nazarov Y. V. van Oudenaarden, A. and J. E. Mooij. Magneto-electric aharonov-bohm effect in metal rings. *Nature*, **391**(6669):768–770, 1998.

[48] Quartz crystal theory. www.jauch.de.

[49] M. L. Roukes K. L. Ekinci. Nanoelectromechanical systems. *Rev. Sci. Instrum.*, **76**:061101, 2005.

[50] Moriwaki S. Mori, T. and N. Mio. Mechanical q-factor measurement of a quartz oscillator at cryogenic temperature. *Applied Physics Express*, **1**(7), 2008.

[51] A. Elhabti and F. O. Bastien. Low-temperature limitation on the quality factor of quartz resonators. *IEEE Transactions on Ultrasonics Ferroelectrics and Frequency Control*, **41**(2):250–255, 1994.

[52] Grutter P. Horne D. Albrecht, T. R. and D. Rugar. Frequency-modulation detection using high-q cantilevers for enhanced force microscope sensitivity. *Journal of Applied Physics*, **69**(2):668–673, 1991.

[53] Technical notes from attocube systems. http://www.attocube.com.

[54] Ihn T. Barengo C. Studerus P. Gildemeister, A. E. and K. Ensslin. Construction of a dilution refrigerator cooled scanning force microscope. *Rev Sci Instrum*, **78**(1):013704, 2007.

[55] Hackens B. Pala M. G. Martins F. Baltazar S. Wallart X. Desplanque L. Bayot V. Sellier, H. and S. Huant. On the imaging of electron transport in semiconductor quantum structures by scanning-gate microscopy: successes and limitations. *Semiconductor Science and Technology*, **26**(6), 2011.

[56] Dai L. Ma R. M. Liu C. Sun T. Yang, W. Q. and G. G. Qin. Back-gate zno nanowire field-effect transistors each with a top omega shaped au contact. *Applied Physics Letters*, **93**(3), 2008.

[57] S. Nakata. Observation of coulomb-blockade oscillations by the back gate with subattofarad mutual capacitance. *Physical Review B*, **47**(3):1679–1682, 1993.

[58] Crauste O. Namatsu H. Horiguchi S. Ono Y. Fujiwara A. Takahashi Y. Nishiguchi, K. and H. Inokawa. Back-gate effect on coulomb blockade in silicon-on-insulator trench wires. *Japanese Journal of Applied Physics*, **44**(10):7717–7719, 2005.

[59] Vignaud D. Godey S. Cadio E. Plissard S. Wallart X. Liu P. Desplanque, L. and H. Sellier. Electronic properties of the high electron mobility al0.56in0.44sb/ga0.5in0.5sb heterostructure. *Journal of Applied Physics*, **108**:043704, 2010.

[60] Karavolas V. C. Peeters F. M. Singleton J. Nicholas R. J. Herlach F. Harris J. J. Van Hove M. van der Burgt, M. and G. Borghs. Magnetotransport in a pseudomorphic gaas/$ga_{0.8}in_{0.2}as$/$ga_{0.75}al_{0.25}as$ heterostructure with a si delta -doping layer. *Physical Review B*, **52**(16):12218, 1995.

[61] D.Y. Lin, M.C. Wu, H.J. Lin, and J.S. Wu. Optical studies of two-dimensional electron gas in an ingaas/algaas pseudomorphic high electron mobility transistor structure. *Physica E: Low-dimensional Systems and Nanostructures*, **40**(5):1757 – 1759, 2008.

[62] T. Suski, P. Wisniewski, L.H. Dmowski, I. Gorczyca, J. Smoliner, E. Gornik, G. Bhm, and G. Weimann. Correlations of the

remote impurity charges–a method of 2deg mobility tuning in gaas/algaas heterostructures. *Solid-State Electronics*, **37**(4-6):677 – 680, 1994.

[63] Wang D. P. Hsieh K. Y. Wang T. F. Mitchel W. C. Ahoujja M. Cheng J. P. Fathimulla A. Lo, I. K. and H. Hier. Persistent-photoconductivity effect in delta-doped al0.48in0.52as/ga0.47in0.53as heterostructures. *Physical Review B*, **52**(20):14671–14676, 1995.

[64] Saint Jean M. Guthmann C. Hudlet, S. and J. Berger. Evaluation of the capacitive force between an atomic force microscopy tip and a metallic surface. *European Physical Journal B*, **2**(1):5–10, 1998.

[65] Maja R. Krčmar and Wayne M. Saslow. Model for electrostatic screening by a semiconductor with free surface carriers. *Phys. Rev. B*, **66**:235310, 2002.

[66] Lutz C. P. Crommie, M. F. and D. M. Eigler. Confinement of electrons to quantum corrals on a metal surface. *Science*, **262**(5131):218–220, 1993.

[67] Lutz C. P. Eigler D. M. Crommie, M. F. and E. J. Heller. Waves on a metal-surface and quantum corrals. *Surface Review and Letters*, **2**(1):127–137, 1995.

[68] M. Reed. Quantum dots. *Scientific American*, **268**, 1993.

[69] Krishnamurthy M. Reaves C. M. Denbaars S. P. Leonard, D. and P. M. Petroff. Direct formation of quantum-sized dots from uniform coherent islands of ingaas on gaas-surfaces. *Applied Physics Letters*, **63**(23):3203–3205, 1993.

[70] Jensen K. F. Murray C. B. Danek, M. and M. G. Bawendi. Synthesis of luminescent thin-film cdse/znse quantum dot composites using cdse quantum dots passivated with an overlayer of znse. *Chemistry of Materials*, **8**(1):173–180, 1996.

[71] Randall J. N. Aggarwal R. J. Matyi R. J. Moore T. M. Reed, M. A. and A. E. Wetsel. Observation of discrete electronic states in a zero-dimensional semiconductor nanostructure. *Physical Review Letters*, **60**(6):535–537, 1988.

[72] Buizert C. Tielrooij K. J. Vink I. T. Nowack K. C. Meunier T. Kouwenhoven L. P. Koppens, F. H. L. and L. M. K. Vandersypen.

Driven coherent oscillations of a single electron spin in a quantum dot. *Nature*, **442**(7104):766–771, 2006.

[73] C. W. J. Beenakker. Theory of coulomb-blockade oscillations in the conductance of a quantum dot. *Physical Review B*, **44**(4):1646–1656, 1991.

[74] Wingreen N. S. Meir, Y. and P. A. Lee. Transport through a strongly interacting electron-system - theory of periodic conductance oscillations. *Physical Review Letters*, **66**(23):3048–3051, 1991.

[75] H. Ishikuro and T. Hiramoto. Quantum mechanical effects in the silicon quantum dot in a single-electron transistor. *Applied Physics Letters*, **71**(25):3691–3693, 1997.

[76] D. Braess. Uber ein paradoxon aus der verkehrsplanung. *Unternehmensforschung*, **12**:258–268, 1969.

[77] J. F. Nash. Equilibrium points in n-person games. *Proceedings of the National Academy of Sciences of the United States of America*, **36**(1):48–49, 1950.

[78] http://en.wikipedia.org/wiki/Braess's_paradox.

[79] http://www.nytimes.com/1990/12/25/health/what-if-they-closed-42d-street-and-nobody-noticed.html.

[80] Joel E. Cohen and Paul Horowitz. Paradoxical behaviour of mechanical and electrical networks. *Nature*, **352**(6337):699–701, 1991.

[81] C. Y. Liu and S. A. Chen. Charge mobility and charge traps in conjugated polymers. *Macromolecular Rapid Communications*, **28**(17):1743–1760, 2007.

[82] Shanware A. Colombo L. Liu, Y. and R. Dutton. Modeling of charge trapping induced threshold-voltage instability in high-kappa gate dielectric fets. *IEEE Electron Device Letters*, **27**(6):489–491, 2006.

[83] Callegari A. Gusev E. Zafar, S. and M. V. Fischetti. Charge trapping related threshold voltage instabilities in high permittivity gate dielectric stacks. *Journal of Applied Physics*, **93**(11):9298–9303, 2003.

[84] Burtone L. Leo K. Ray, D. and M. Riede. Detection of trap charge in small molecular organic bulk heterojunction solar cells. *Physical Review B*, **82**(12), 2010.

[85] Genevicius K. Nekrasas N. Juska, G. and G. Sliauzys. Charge carrier transport, recombination, and trapping in organic solar cells studied by double injection technique. *IEEE Journal of Selected Topics in Quantum Electronics*, **16**(6):1764–1769, 2010.

[86] L. Sanche and M. Deschenes. Mechanisms of charge trapping at a dielectric surface - resonance stabilization and dissociative attachment. *Physical Review Letters*, **61**(18):2096–2098, 1988.

[87] Lee J. J. Lyding J. W. Kim Y. K. Kim Y. W. Cheng, K. G. and K. P. Suh. Separation of hot-carrier-induced interface trap creation and oxide charge trapping in pmosfets studied by hydrogen/deuterium isotope effect. *IEEE Electron Device Letters*, **22**(4):188–190, 2001.

[88] H. M. Branz. Charge-trapping model of metastability in doped hydrogenated amorphous-silicon. *Physical Review B*, **38**(11):7474–7479, 1988.

[89] Park H. Chang M. Jung H. S. Lee J. H. Jo, M. and H. Hwang. Oxygen vacancy induced charge trapping and positive bias temperature instability in hfo2 nmosfet. *Microelectronic Engineering*, **84**(9-10):1934–1937, 2007.

[90] Tsukimoto S. Saito M. Wang, Z. C. and Y. Ikuhara. Individual charge-trapping dislocations in an ionic insulator. *Applied Physics Letters*, **95**(18), 2009.

[91] Jae-ho Kim Jea-hun Jung Chong-seung Yoon Tae-whan Kim, Young-ho Kim. Charge trap flash memory device, fabrication method thereof, and write/read operation control method thereof. *US Patent*, 2009.

[92] Cho-J. Lee C. Kim I. Park-J. Kim Y. M. Shin H. Lee J. Lee, J. S. and F. Caruso. Layer-by-layer assembled charge-trap memory devices with adjustable electronic properties. *Nature Nanotechnology*, **2**(12):790–795, 2007.

[93] Anthony-J. E. Jaquith, M. J. and J. A. Marohn. Long-lived charge traps in functionalized pentacene and anthradithiophene studied by time-resolved electric force microscopy. *Journal of Materials Chemistry*, **19**(34):6116–6123, 2009.

[94] John Lai Guann-Pyng Li Hsiang Chen, Phillip Preecha. Charge trapping at surface in gan hemts. *CS MANTECH Conference, Chicago, Illinois, US*, April 14-17, 2008.

[95] Stollenwerk A. J. Narayanamurti-V. Anikeeva P. O. Panzer M. J. Wood V. Hummon, M. R. and V. Bulovic. Measuring charge trap occupation and energy level in cdse/zns quantum dots using a scanning tunneling microscope. *Physical Review B*, **81**:115439, 2010.

[96] Kicin S. Brunner D. Ihn-T. Sigrist M. Ensslin K. Reinwald M. Pioda, A. and W. Wegscheider. Discrete charging of traps visualized by scanning gate experiments on a quantum point contact. *Physical Review B*, **75**:045433, 2007.

[97] Ihn T. Schleser R. Ensslin K. Driscoll D. C. Gildemeister, A. E. and A. C. Gossard. Imaging a coupled quantum dot-quantum point contact system. *Journal of Applied Physics*, **102**:083703, 2007.

[98] Maja Krčmar, Wayne M. Saslow, and Michael B. Weimer. Electrostatic screening near semiconductor surfaces. *Phys. Rev. B*, **61**:13821–13832, 2000.

[99] A. K. Geim and K. S. Novoselov. The rise of graphene. *Nat Mater*, **6**(3):183–191, 2007.

[100] Veligura Alina Junesch Juliane Guimaraes Marcos H. D. Vera-Marun Ivan J. Jonkman Harry T. Tombros, Nikolaos and Bart J. van Wees. Quantized conductance of a suspended graphene nanoconstriction. *Nat Phys*, **advance online publication**, 2011.

[101] M. Z. Hasan and C. L. Kane. Colloquium: Topological insulators. *Rev. Mod. Phys.*, **82**(4):3045–3067, Nov 2010.

[102] Matthias Baenninger Christoph Brüne Hartmut Buhmann Laurens Molenkamp David Goldhaber-Gordon Markus König, Andrei Garcia. Local probing of quantum spin hall edge states. *APS March Meeting*, 2011.